



UNIVERSITY OF BARI "ALDO MORO"

UNIVERSITY OF MONTPELLIER

INTERUNIVERSITY DEPARTMENT OF PHYSICS "M. MERLIN"

PHD in FISICS – Cycle XXXVI

Scientific Disciplinary Sector: FIS/01

Compact diode -based QEPAS sensors for UAVs

Doctorand:

Kniazeva Elena

Supervisors:

Prof. Vincenzo Spagnolo

Prof. Aurore Vicet

Coordinator:

Prof. Giuseppe Gonnella

2023

Acknowledgments

Throughout the years of my PhD project, I have received a lot of support and help from many people whom I would like to thank.

First and foremost, I have a lot of gratitude to my research supervisors: Aurore Vicet and Vincenzo Spagnolo, who always showed high level of professionalism in their fields. I am grateful that you gave me this opportunity and continued to support me through all the years. Thank you for your assistance, understanding and patience. I have learnt a lot from you in the past years and am proud of accomplished this goal under your supervision. I appreciate the time and work you have put into this project.

I also want to thank Alexei Baranov for encouraging me during my period at University of Montpellier and giving me an example of brilliant work. I want to thank Alexei for the enormous help throughout all challenges, professional and personal. I want to thank you for taking an interest in my work and for all of your valuable opinions and advices.

A lot of gratitude towards Eric Tournie for being such a professional and vise leader and being a person to look up to. I value a lot your contribution.

I want to thank Ariane Meguekam-Sado for the supervision in the clean room facility and for training me, it was a pure pleasure to learn from you.

A lot of thanks to the entire NANOMIR group, highly appreciate each member of the team and grateful for guidance and for making me feel at home from the very first day.

I am very grateful to Robert Weih for giving me the incredible opportunity to do the secondment in company Nanoplus. I have a lot of respect for your professionalism. Thank you for showing me the world of MBE and helping me to realize my ideas in your facilities. I am grateful for the warm welcome in the company, for your supervision and support.

I want also to thank Angelo Sampaolo, Marilena Giglio and Andrea Zifarelli from Polysense group for very warm welcome and being always ready to help. I am very glad that I got to know you and appreciate all the time we spent together through my PhD.

I want to thank Stefano Dello Russo, with whom I was working in the beginning of my project and who made the start of my research path smooth and productive. You are an amazing researcher and human being; I value a lot everything you have done for me, and I learnt a lot from you.

I want to thank my all my friends, who had to deal with my emotional roller coasters on the way and lifted me up way too many times. I am grateful that you were right by my side through this journey and love you with all my heart. Among the others I especially want to highlight Anna Michailovskaya, Anna Froom, Jordan, Ance, Yulia, Lena, Gianlorenzo, Magda and Terrezza. And all my friends back from Sain-Petersburg - Vika, Yana , Anna and Ilya, Varya, Katya. Thank

you for not forgetting me and for spending so much time on these long video calls proving that distance does not matter.

I want to thank my partner, Jonathan; I could never be happier to go through the last year of my PhD journey with you by my side. Thank you for being my rock and believing in me even when I didn't. Thank you for all the smiles and immersive amount of love I received daily.

I am very grateful to my grandfather, without whom this journey would have never happened. Thank you for guiding me through life, thank you for planting my interest in science and thank you for being always an incredible example to which I can look up to. I will never be able to repay all you have done for me, and I would never be the same person without you. You are my inspiration.

I want to thank my entire family for being supportive, loving and patient with my choices.

I am also very grateful to any person I met on the way, especially to all the members of OPTAPHI network.

It was a big journey, full of Ups and Downs, and it will stay with me forever.

Contents

Introduction 7

Chapter 1. Gas sensing techniques 11

1.1 Conventional non-optical techniques …….12

1.1.1 Chromatography spectrometry **…….12**

1.1.2 Semiconductor spectroscopy **……17**

1.1.3 Electrochemical sensors **……...20**

1.2 Direct laser absorption spectroscopy 22

1.3 Tunable Diode Laser Absorption Spectroscopy (TDLAS) …….…….23

1.4 Multi-pass and cavity-enhanced optical sensors. …….……...…...25

References Chapter 1……...……29

Chapter 2. Laser sources for gas sensing. State of the art …….…….….34

2.1. History …….…….…34

2.2. Laser's types ……..…….34

2.2.1 Laser diodes **……36**

2.2.2 Quantum cascade lasers (QCLs)……..……**37**

2.2.3 Interband cascade lasers (ICLs)……..…….**39**

2.3. Single-frequency laser sources in MidIR …….….40

2.3.1 DFB lasers with lateral grating along the ridge **……47**

2.3.2 DFB lasers with corrugation of the sidewalls……..……**48**

2.3.3 DFB lasers with buried grating design……..…….**49**

2.3.4 DFB lasers with grating on the top of the laser ridge…….**49**

References Chapter 2 ……..……**51**

Chapter 3. Novel GaSb based DFB laser diodes emitting at 2.4 μm. Simulations and Fabrication …….…….**57**

3.1 Simulations in COMSOL Multiphysics……**58**

3.1.1 Estimation of the optimum design in terms of thickness of upper cladding layer and depth of grating's etch (evaluation of losses, coupling factor and confinement factor)………**60**

3.1.2 Simulations of Mesa's etching, determination of the allowed error for technological process ……**67**

3.2 Fabrication of novel laser chips in clean room ……..**69**

3.2.1 *Fabrication techniques*……**69**

3.2.1.1 Photolithography ……**69**

3.2.1.2 E-beam lithography……...……**71**

3.2.1.3 Inductively coupled plasma (ICP) dry etching ……**72**

3.2.1.4 Deposition of metal by evaporation technique……..**72**

3.2.1.5 Deposition of metal by sputtering technique……**73**

3.2.2 Wafer's growth ……**73**

3.2.3 *Fabrication of Fabry-Perot laser diodes* ……..**75**

3.2.4 Fabrication of DFB laser diodes with grating on the top of the laser ridge (Montpellier) **……80**

3.2.4.1 Tests for grating E-beam exposure and grating etching…….**81**

3.2.5 Fabrication of DFB laser diodes with grating on the top of the laser ridge (NANOPLUS) **……....87**

3.2.6 Fabrication of DFB laser diodes with lateral metal grating along the ridge (NANOPLUS) **…….89**

References Chapter 3 ……..…91

Chapter 4. Novel GaSb based DFB laser diodes emitting at 2.4 µm. Experimental results and discussions ……93

4.1. Characterisation of laser diodes ……....93

4.1.1. L-I-V characteristics in CW mode **……..93**

4.1.2. Spectrum measurement in FTIR……...**93**

*4.1.3. Important parameters extracted from LIV curve and emission spectrum***…94**

4.2 Results on custom Fabry-Perot laser diodes with thin cupper cladding and thin top contact layers. …….97

4.3 Results on custom DFB laser diodes with thin upper cladding and thin top contact layers with grating on the top of the laser ridge (fabrication in Montpellier)……103

4.4 Results of Custom DFB Laser Diodes with thin upper cladding and thin top contact layers fabricated at Nanoplus…….110

4.4.1. Top grating samples fabricated at Nanoplus **……112**

*4.4.2. Spectrum measurement in FTIR***……114**

*4.4.3. Important parameters extracted from LIV curve and emission spectrum..***116**

References Chapter 4 ……120

Chapter 5. Quartz enhanced photoacoustic spectroscopy……..…123

5.1 PAS.Theory 123

5.2 QEPAS. Theory and state of the art 132

5.3 QEPAS twin - sensors for Methane and Nitrious oxide detection.....135

5.4 QEPAS sensor for ammonia detection.....149

Conclusions.....161

References Chapter 5 164

Introduction

Today, many aspects of our daily life depend on data collection with various sensors. Recent rapid development of gas sensing technologies has opened the way to many critical applications, including environmental monitoring, safety, security, oil and gas exploration, and biomedical analysis. These technologies must be capable of detecting multiple gases across a wide concentration range, from trace levels to high percentages, while also providing real-time, in-situ operation and precise identification and quantification of gas constituents.

The market for gas sensors is continually growing and up to date there are various solutions for species detection. All the spectroscopy methods can be mainly divided in two groups: those who employ a non-optical way and those who employ an optical technique. Three main families of non-optical detectors can be identified as: chromatography, semiconductor and electrochemical spectroscopy. On the other hand, optical sensors can be divided in two groups, based on direct absorption such as tunable diode spectroscopy or indirect absorption like photoacoustic spectroscopy (indirect). Quartz-Enhanced Photoacoustic Spectroscopy (QEPAS) is a form of indirect absorption spectroscopy that harnesses the photoacoustic effect. In this technique, a quartz tuning fork (QTF) serves as a transducer due to its piezoelectric properties, converting acoustic waves into electrical signals. Typically, a laser emitting at a specific wavelength matching an absorption line of studied gas sample is used as the light source.

The laser source plays a critical role in QEPAS as in any other absorption spectroscopy. Several properties of the laser source are essential:

- Output power: Higher laser power results in stronger signals for.

- Wavelength accuracy: The laser's wavelength needs to match the selected absorption line of the target gas for effective detection.
- Line Width and single mode operation: both are crucial, as they ensure that the laser light closely matches only the selected absorption feature of the gas. This feature is essential for selectivity.
- Tunability: The ability to tune the laser's emission wavelength is valuable for targeting absorption features belonging to different gas molecules (multi gas detection).

Diode lasers are frequently chosen as the laser source for such technique due to their compact size and the ability to alter their emission wavelength by adjusting temperature and current. Distributed Feedback Diode Lasers (DFB-LDs) are particularly well-suited for gas sensing. They feature a structured element or diffraction grating in the active region of the laser, creating a one-dimensional interference grating. This grating provides optical feedback for the laser, resulting in high wavelength filtering and stability and a narrow linewidth. For instance, the 2.3-2.4 μm range is highly attractive for gas sensing in the atmosphere since it corresponds to the absorption lines of several gases like CO, NH_3, CH_4 and HF [1]. These absorption lines are within a transparency window for H_2O and CO_2, which are the primary interferents in ambient air.

This research work is a result of joint doctorate program within training network OPTAPHI (https://www.optaphi.eu/) and was conducted between two institutions (University of Bari and University of Montpellier) and one industrial company (Nanoplus). There are two main objectives of current research thesis. The first goal is to design and fabricate custom DFB laser diodes based on GaSb material family for future application in QEPAS systems, which was realised at University of Montpellier and at Nanoplus. Developing custom DFB laser diodes feature the DFB grating directly on the laser ridge, eliminating the need for wall corrugations along the ridge or

epitaxial regrowth on the active zone. The idea is to fabricate devices having thinner layers structure for a better coupling between the DFB grating and lasing mode. The second aim of the work is to develop and realise compact and highly sensitive QEPAS sensors for toxic gases detection, exploiting custom QTFs (this objective was realised at University of Bari). Developed sensors could be used in future for the environmental sensing with unarmed air vehicles (UAVs), due to achieved dimensions and weight of the final device.

The whole thesis consists of 5 chapters.

Chapter 1. The first chapter provides an in-depth analysis of the present-day sensing technology market, with a specific focus on its applications in toxic gas detection. We will assess the strengths and limitations of these technologies, especially in the context of safeguarding the environment from hazardous gases. Our exploration encompasses a comprehensive overview of both traditional techniques like chromatography and semiconductor spectroscopy, followed by an introduction to contemporary absorption methods, including multi-pass and cavity-enhanced optical sensors. By examining these diverse approaches, we aim to provide a holistic perspective on the current landscape of gas sensing technologies and their relevance in environmental protection and industrial applications.

Chapter 2. In this section, one will discover an overview of the historical evolution of lasers and fundamental principles, along with an in-depth examination of the current state-of-the-art semiconductor laser sources. Detailed information on laser diodes, Quantum Cascade Lasers (QCLs) and Interband Cascade lasers (ICLs) will be presented. These lasers are readily accessible in the market and are primarily utilized for gas sensing applications. Towards the conclusion of this chapter, special attention will be given to single-frequency laser sources with emission within the Mid-IR spectral range.

Chapter 3. The third chapter is entirely dedicated to the design and realization of custom GaSb-based DFB laser diodes operating at a wavelength of 2.4 μm. The initial step involves conducting simulations of the desired structure using COMSOL Multiphysics, where various parameters of the future devices are systematically adjusted, such as the thickness of the upper cladding and the depth of etching. Subsequently, the chapter transitions into the fabrication phase of the laser chips. This section starts with a comprehensive explanation of the essential techniques required for the fabrication of laser diodes in a general context. To validate the results obtained from the simulations and prove the feasibility of the proposed modifications to the laser structure, the development of Fabry-Perot laser diodes with custom laser thicknesses will be elaborated. The chapter finishes with a detailed explanation of the fabrication process for DFB laser diodes, implementing different designs. Mentioned fabrication activities take place within an academic clean room in Montpellier, France, as well as an industrial clean room at Nanoplus in Germany.

Chapter 4. Here we will present and deliberate upon all the outcomes derived from the characterization of the laser sources whose design and manufacturing processes were introduced in Chapter 3. In-depth study on 2 generations of Fabry-Perot laser diodes with modified laser structures is conducted. This will be followed by the wide discussion on results from different achieved designs for DFB laser diodes (devices with grating on the top of the ridge and devices with grating along the ridge, both featuring different thicknesses of upper cladding). Furthermore, we will evaluate the prospective applications for these devices, assessing their potential utility in the market among other laser sources tailored for spectroscopy applications.

Chapter 5 is focused on Quartz Enchased Photoacoustic Spectroscopy (QEPAS). The chapter will start with the explanation of general principles for photoacoustic spectroscopy, turning to the theory and history of development for QEPAS. Later results on the development of compact, light-

weighted twin sensors for N_2O and CH_4 detection with minimum detection limits in ppb range will be presented. As the last part of the section, the performance of sensor for NH_3 detection and theoretical study on its calibration methods will be described.

Chapter 1. Gas sensing techniques

The ability to detect with high precision concentrations of toxic gases in ambient air and in human breath hold significant importance in various scientific and industrial domains. This capability is instrumental in enhancing our comprehension and surveillance across a diverse spectrum of applications, including but not limited to environmental monitoring, industrial process control analysis, combustion processes, the detection of hazardous gases, as well as breath analysis for medical studies. For instance, within the realm of atmospheric science, there is a critical need for trace gas sensors characterized by heightened sensitivity and selectivity. These sensors are indispensable for monitoring an array of trace gas species, encompassing greenhouse gases and ozone. Similarly, in the field of breath diagnostics, sensors must detect and quantify gases like nitric oxide, ethane, ammonia, and numerous other biomarkers. Quantitative and qualitative gas sensors can be broadly categorized into distinct groups, each contingent on the underlying physical mechanisms employed for detection. These categories encompass analytical sensors, prominently represented by gas chromatography and mass spectrometry; electrochemical sensors; semiconductor sensors; and laser optical absorption sensors.

This sensor classification is primarily predicated upon the fundamental principles and mechanisms utilized in the detection process. In the current chapter, we will conduct an in-depth examination

of mentioned gas sensors technique, shedding light on the respective advantages and limitations associated with each detection method. Ideally, the sensor should match the requirements on such parameters as high sensitivity (it refers to a sensor's ability to detect the smallest concentrations of the target gas), selectivity (it refers to a sensor's ability to distinguish between different gases or chemical compounds and respond specifically to the target gas of interest while ignoring or having minimal interference from other gases or environmental factors) and stability (it refers to its ability to maintain consistent and reliable performance over time under normal operating conditions), low response time and recovery time, low fabrication cost, and should be able to operate in situ with real-time measurements.

1.1 Conventional non-optical techniques

The traditional analytical methods for gas sensing will be discussed in this part, including semiconductor sensors, gas chromatography-mass spectrometry, and electrochemical sensors.

1.1.1 Chromatography spectrometry

The first technique under the discussion will be gas chromatography, which started developing with the pioneering work of Ramsey [2] and Tswett [3] back in 1903. The roots of modern gas chromatography (GC) trace back to 1952 when it was first conceptually articulated by Martin and James [4]. Over the subsequent decades, GC has firmly established itself as the quintessential standard in the realm of analytical chemistry, primarily due to its exceptional sensitivity and unwavering reliability. The International Union of Pure and Applied Chemistry (IUPAC) formally defines chromatography as "a physical method of separation in which the components to be separated are distributed between two phases, one of which remains stationary (stationary phase), while the other traverses in a predetermined direction (mobile phase)" [5]. In essence, this

technique hinges on the fundamental principle of differential migration, where the individual components within a complex mixture exhibit varying affinities for the stationary and mobile phases, thereby facilitating their separation.

Gas chromatography, specifically, serves as an invaluable tool for the separation of volatile compounds. These volatile substances, characterized by their propensity to readily transition from a liquid to a gas state, find themselves amenable to the GC process. Through the strategic use of a stationary phase within the chromatographic column and a mobile phase, which is typically an inert carrier gas, GC achieves the meticulous partitioning and isolation of individual compounds within a sample.

The utility of gas chromatography extends beyond mere separation; it encompasses the capacity to identify these isolated compounds. This feat is achieved through the utilization of various types of detectors, each attuned to specific chemical properties or interactions. By coupling GC with these detectors, it becomes possible to achieve a precise and comprehensive understanding of the composition of a given sample [6]. A typical gas chromatograph apparatus shown on Fig. 1.1.

The carrier gas, typically an inert gas like hydrogen or helium, maintains a continuous flow originating from a gas cylinder. This flow traverses through a sequence comprising the inlet, the column, and ultimately reaches the detector. The sample earmarked for analysis undergoes

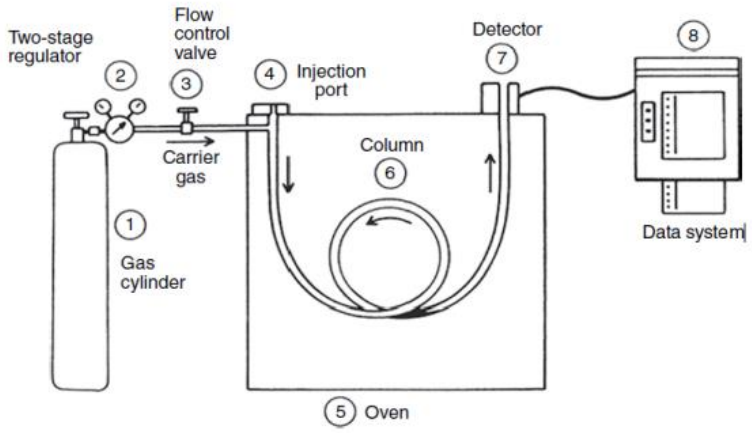


Figure 1.1. Schematic representation of typical gas chromatograph set up [5]

injection into the heated inlet and is subsequently carried into the column. Within the column, the crucial separation of the various components within the mixture takes place.

The column, typically a capillary column measuring between 15 cm to 30 cm in length, possesses an interior coating consisting of a slender film (measuring between 0.2 to 1 μm) composed of a high-boiling liquid, known as the stationary phase. It is at this juncture that the sample undergoes a meticulous separation, with each constituent diverging between the mobile and stationary phases. This separation hinges on the relative solubility and vapor pressures exhibited by the analytes.

Upon exiting the column, both the carrier gas and the sample proceed to traverse through a detector, which may encompass a range of options such as flame ionization detectors (FID), nitrogen phosphorus detectors, electron capture detectors, photoionization detectors (PID), thermal conductivity detectors, and mass spectrometric detectors (MS). Notably, in the domain of gas

chromatography, mass spectrometry (MS) and flame ionization detection (FID) stand out as the most prevalent choices for laboratory analysis of intricate gas matrices.

Mass spectrometry (MS) scrutinizes the mass-to-charge ratio (m/z) of the chemical species present within the sample. From this precise measurement, it becomes feasible to derive the molecular weight of each component. This capability not only facilitates the identification of unknown compounds but also empowers the quantification of their abundance within the sample. Thus, the combined attributes of gas chromatography and mass spectrometry play a pivotal role in unravelling the intricate composition of complex gas mixtures encountered in analytical endeavours. The flame ionization detector (FID) stands as the instrument of choice when it comes to detecting hydrocarbons. This preference arises from the fact that any hydrocarbon gas, when burned within a hydrogen flame, gives rise to the production of ions. These generated ions undergo detection via a pair of electrodes, establishing a potential difference. Consequently, the ions are propelled toward the negatively charged electrode, thereby inducing an electric current. This current is directly proportional to the rate of ionization and, consequently, to the concentration of hydrocarbon gas present in the sample.

GC-MS, on the other hand, signifies the pinnacle of analytical techniques aimed at identifying organic substances. This sophisticated approach finds widespread application in critical domains such as environmental science, healthcare, explosive detection, biological research, food safety, and numerous others [7]. In the GC-MS methodology, the gas chromatograph effectively segregates the components within a mixture, while the mass spectrometer diligently undertakes the structural elucidation of each individual component, providing both qualitative and quantitative insights.

Main advantaged of the explained techniques are:

- it demands only minute sample quantities, often measured in the microliter (μL) range.
- it boasts exceptional resolution (exceeding 60 000 with five orders of magnitude dynamic range)[8] and identification capabilities.
- it offers rapid response times (150 ptsec) [9]

The application of GC-MS has yielded significant advancements in environmental analysis [10], enriched biological investigations [11], and enhanced the quality control and safety measures within the food industry [12]. Consequently, GC-MS stands as a cornerstone technology that has revolutionized our capacity to dissect and comprehend the intricacies of the natural and man-made world.

Gas Chromatography with Flame Ionization Detection (GC-FID) stands as the preeminent detection technique extensively applied in the oil and gas industry for the purpose of hydrocarbon detection. In this specialized sector, gas samples acquired as a byproduct of drilling operations undergo meticulous analysis to unravel the distinct characteristics of the designated reservoir. Upon collection, these samples undergo requisite treatment before being subjected to examination through GC-FID. This analytical tandem performs a dual role: the gas chromatograph (GC) facilitates the precise separation of analytes, while the flame ionization detector (FID) is entrusted with the crucial task of quantification.

The salient virtues of employing GC-FID in this context are manifold and underscore its prominence:

- simplicity
- unwavering reliability
- exceptional versatility

- straightforward operational procedures
- propensity to generate minimal or negligible signals in response to commonplace carrier gases (such as helium, argon, or nitrogen) or the typical contaminants that may be present within these gases (e.g., oxygen and water vapor) [13].

1.1.2 Semiconductor spectroscopy

Next conventional technique to be discussed is semiconductor spectroscopy. Semiconductor sensors operate based on a fundamental physical principle: when the sensor's surface comes into contact with the surrounding environment, gases interact with the sensing material, resulting in alterations of key physical characteristics such as conductivity, permittivity, and work function [14]. To translate these variations in physical parameters into electrical changes, a transducer is employed. This transducer converts the modifications in physical parameters into corresponding electrical alterations, affecting attributes like resistance, capacitance, and inductance. Consequently, this process generates a voltage or current signal whose magnitude, frequency, and phase can be precisely measured and correlated with the concentration of the gas being absorbed.

While the underlying principle remains consistent, diverse types of semiconductor gas sensors have emerged over recent years, each distinguished by the specific sensing materials used. These materials include metal oxides, carbon nanotubes, conducting polymers, and two-dimensional materials [15]. Notably, metal oxides have garnered widespread use and application in commercial devices, whereas the others represent novel materials still in the research phase, primarily harnessed to overcome the limitations associated with metal oxide gas sensors.

Metal oxide semiconductors, categorized into n-type semiconducting oxides such as tin oxide (SnO_2), zinc oxide (ZnO), and tungsten oxide (WO_3), and fewer instances of p-type variants, have

undergone extensive investigation. These sensors are primarily employed to detect gases through redox reactions occurring at the interface between the target gases and the oxide surface. This redox process unfolds in two steps: initially, redox reactions prompt the distribution of oxygen species on the material's surface to engage with the molecules of the target gases, leading to electronic changes on the oxide surface. Subsequently, this alteration is translated into an electrical resistance shift within the sensor.

The sensitivity of these sensors is intricately linked to the redox reaction, which, in turn, is influenced by various factors encompassing the characteristics and morphology of the sensing layer. Notably, high operating temperatures are often required for these sensors [16]. To attain such temperatures, a heated filament or micro-hotplate is employed to preheat the sensitive layer, heightening the likelihood of gas molecule adsorption onto the layer's surface. For example, the operational temperature range for SnO2-based sensors typically spans from 25°C to 500°C, with the specific temperature chosen depending on the type of gas to be detected. This leads to possible loose in sensitivity with temperature fluctuations.

Metal oxide semiconductor sensors offer several advantages, such as:

- cost-effectiveness
- lightweight nature
- ease of manufacturing
- user-friendly operation
- capability to detect a wide range of gases, including flammable and toxic ones

However, these sensors also come with their share of disadvantages and limitations, they are as follow:

- poor selectivity
- susceptibility to cross-sensitivity
- extended recovery periods required after gas exposure (which hampers their utility in applications necessitating continuous gas concentration monitoring)
- elevated power consumption
- baseline resistance drift

To ameliorate the precision and selectivity concerns, one approach involves employing various sensing materials and implementing multisensory arrays. Among metal oxide options, SnO_2 stands as one of the most frequently used in practical commercial gas sensor devices. A notable producer of metal oxide gas sensors is Figaro Engineering Inc., renowned for its production of sensors designed to monitor hazardous levels of explosive gases within homes [17]. The pursuit of small-sized sensors, driven by commercial demand, has led to the development of advanced production technologies, culminating in state-of-the-art Micro Electro-Mechanical Systems (MEMS).

In contrast, conducting polymers offer alternative gas sensing materials with advantages such as room-temperature operation, robust mechanical properties, and facile synthesis. Nonetheless, they suffer from drawbacks that hinder their broad practical application, including long-term instability, irreversibility, and low selectivity. Over time, these sensors experience a decline in response that is irreversible, adversely affecting their sensitivity over their operational lifespan. Moreover, their stability is substantially influenced by ambient conditions, including variations in humidity and temperature, which can impact the chemical and physical characteristics of the gas-sensing conducting polymer layer. Additionally, interactions between the analyte and conducting polymer can induce a swelling effect within the conducting polymer layers, thereby affecting electrical resistance and overall sensing performance.

Carbon nanotubes (CNTs), owing to their exceptional chemical and mechanical stability coupled with excellent electronic properties, hold promise for gas sensing applications [18]. They possess the potential to significantly influence the gas sensing market [19]. Regrettably, their commercialization is impeded by technological challenges. The synthesis of CNTs is both costly and intricate, as achieving continuous defect-free nanotubes remains a formidable task [20]. If talk about conducting polymers, the sensor response to gases one wants to target can be influenced by the presence of water vapor.

1.1.3 Electrochemical sensors

In conjunction with semiconductor gas sensors, electrochemical sensors have garnered widespread adoption as effective means for detecting toxic gases. Presently, a diverse array of electrochemical sensors finds extensive utilization across a spectrum of stationary and portable applications, particularly in the realm of personal safety [21]. The fundamental architecture of an electrochemical sensor represents an electrochemical cell containing following components: a sensing electrode, a reference electrode, and a counter electrode. These components are demarcated by a slender layer of electrolyte, as visually depicted in Figure 1.2 [22].

Initially, the gas traverses a narrow capillary-type aperture, subsequently diffusing through a hydrophobic barrier. It then proceeds to undergo reactions at the surface of the sensing electrode. When the cell comes into contact with the target gas, a cascade of chemical reactions ensues, culminating in the generation of an electric current that flows between the anode and the cathode. This current exhibit a direct and proportional correlation with the concentration of the gas. The sensitivity of this process hinges predominantly upon the number of reactive sites on the electrode and the dimensions of the gas inlet.

These sensors boast several key advantages, such as:

- a remarkable degree of specificity toward the target gas
- a straightforward linear correlation between current output and gas concentration
- the potential for miniaturization due to the simplicity of the apparatus
- an innate immunity to alterations in sensitivity, accuracy, and linearity brought about by changes in size
- an innate immunity to alterations in sensitivity, accuracy, and linearity brought about by changes in size

Conversely, electrochemical sensors grapple with certain limitations linked to the underlying chemical reactions. For instance, the speed of these reactions decreases as temperatures drop. They

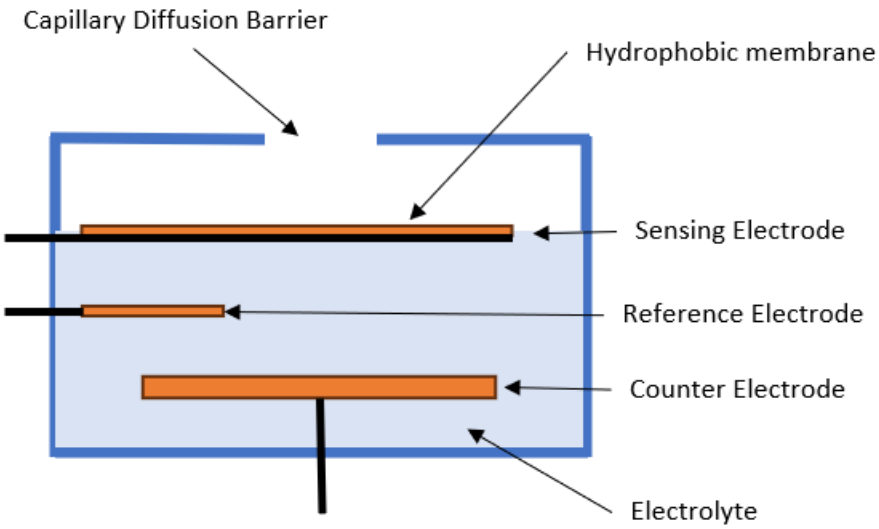


Figure 1.2. Schematic representation of an electrochemical sensor

are also susceptible to disturbances from alkaline metals, which can induce sensor drift, as well as silicon vapours that may deposit on the sensor surface. Furthermore, operation within low-oxygen

environments can impact overall sensor performance, particularly when the oxidation of the target gas occurs at the sensing electrode.

1.2 Direct laser absorption spectroscopy

Direct Laser Absorption Spectroscopy (DLAS) is a technique used in analytical chemistry and physics to study the interaction between light and matter. This methodology typically employs a laser as the primary source of radiation to quantitatively assess the degree of absorption exhibited by a specimen at discrete wavelengths of radiation. This technique uses precise measurements of the interaction between electromagnetic radiation from a laser and gas molecules to determine the presence and number of gases in the environment. In DLAS laser beam passes through the sample, and the amount of light absorbed by the substance is detected by a photodetector. The principle of molecular absorption is based on the transitions that an electromagnetic wave causes in a chemical species. If a molecule is irradiated by infrared light, it is excited to a rotational-vibrational energy level manifold. Absorption lines are specific for each chemical species. By measuring the decrease in light intensity (absorbance), the concentration of the target substance can be determined using the Beer-Lambert Law.

$$I(\lambda) = I_o e^{-\alpha(\lambda) l} \quad (1.1)$$

"I" represents the intensity of light that passes through the cell housing the desired gas, while "I_0" signifies the intensity of the incident light that initially strikes the gas cell. The parameter "α" denotes the absorption coefficient specifically at the wavelength denoted as λ, and "l" corresponds to the optical path length of the cell. This absorption coefficient "α" is intricately linked to the gas concentration, denoted as "n," and the absorption cross-section, represented as σ(λ), by way of the equation:

$$\alpha(\lambda) = \sigma(\lambda) * n \quad (1.2)$$

Therefore, the most basic configuration of a Laser Absorption Spectroscopy (LAS) sensor comprises three essential components: a laser source, a gas cell, and an optical detector.

1.3 Tunable Diode absorption spectroscopy

Leveraging the capacity to tune the wavelength of a diode laser, one of the frequently employed techniques is known as tunable diode laser absorption spectroscopy (TDLAS). This method allows for the exploration of the emission wavelength of a laser diode with a narrow linewidth across a gas absorption line, achieving remarkable spectral resolution. The high resolution brings forth several advantages:

- Elevated Signal-to-Noise Ratios (SNRs): This arises from the complete resolution of absorption lines and a limited effective baseline, contributing to heightened precision.
- Enhanced Selectivity: As the single absorption feature narrows, the potential for overlap with other lines from potential interferents diminishes, bolstering selectivity.
- Expedited Operation: Many laser sources can modulate their wavelength at frequencies up to the MHz range, primarily restrained by the capabilities of the electronics used for signal retrieval, resulting in swift operation [23].

The TDLAS technique is typically implemented in two configurations: direct absorption spectroscopy and wavelength modulation spectroscopy (WMS). In the direct absorption spectroscopy approach, the laser diode's injection current is adjusted to scan one or more

absorption lines, while a photodetector records the transmitted power. The resulting transmission profile exhibits a rising background due to the laser source's output intensity increasing with drive current. This background is punctuated by a dip corresponding to the gas line absorption, as depicted in Figure 1.3(a). To isolate the gas absorption line, it can be extracted by subtracting the zero-reference (indicated by the dotted line in Figure 1.3(a)) or by normalizing the detected signal to the input light intensity.

Conversely, in the WMS approach, a sinusoidal modulation is superimposed onto the laser source's scanning injection current. This imparts a sinusoidal modulation to the emission wavelength, effectively acting as a dither over the absorption features. When coupled with second harmonic (2f) detection, the peak value of the reconstructed absorption feature, which closely resembles the second derivative of the Lorentzian function with minor distortions due to RAM contribution,

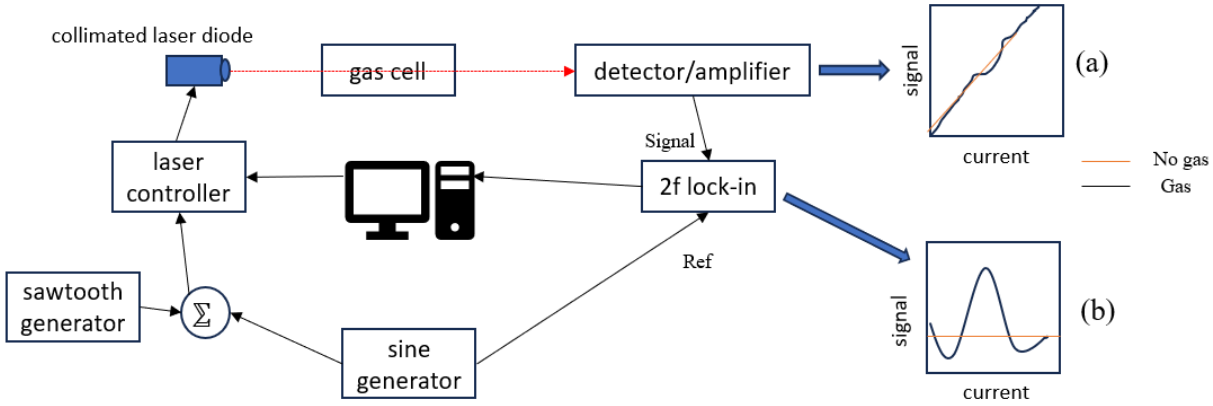


Figure 1.3. The typical setup for TDLS using a laser diode is illustrated, with detected signals plotted against the laser's drive current. In this representation, (a) demonstrates the direct scanning of the gas line, while (b) showcases 2nd harmonic wavelength modulation spectroscopy (2f-WMS). Notably, in plot (a), the influence of RAM is evident through the increasing background signal, and in the case of plot (b), the asymmetry is observable in the negative lobes of the retrieved 2f-lineshape.

becomes directly proportional to the gas concentration. Importantly, this method eliminates background interference, as showcased in Figure 1.3(b).

TDLAS has harnessed the advancements in the swift evolution of high-power, high-resolution laser sources [24,25], which constitute the central components of a TDLAS sensor in conjunction with photodetectors. The capability to efficiently detect multiple analytes using TDLAS sensors is attainable by employing appropriate laser sources and photodetectors. These components are adept at pinpointing and reconstructing various absorption features with commendable sensitivity and selectivity.

1.4 Multi-pass and cavity-enhanced optical sensors

As per Equation 1.1, the optical path length within a gas sample plays big role in laser spectroscopy, as it serves to amplify the absorption signal, thereby enhancing sensor sensitivity. In situations where absorption signals are inherently small due to factors such as a low concentration of gas molecules or weak absorption line strengths, compensatory measures are required. This is where the utilization of multipass cells (MPCs) or cavity-enhanced techniques becomes particularly valuable. Among the direct absorption-based methods, tunable diode laser absorption spectroscopy employing multipass cells stands out as the most representative approach.

In this technique, the laser beam undergoes multiple reflections at various locations within a gas cell, facilitated by two large diameter focusing mirrors that constitute the multipass cell. Consequently, the optical path length can be substantially extended, reaching lengths of up to 100 meters, even when the actual gas cell is only a few tens of centimetres long. Various configurations of MPCs have emerged, with some of the most well-known designs attributed to White [26], Herriott et al. [27], and Chernin and Barskaya [28]. Additionally, for more compact setups, alternative arrangements involving pairs of cylindrical or astigmatic mirrors have been proposed

[29]. However, it's worth noting that MPCs come with certain drawbacks, including the need for meticulous optical alignment, as well as the introduction of additional fringes resulting from interference between successive passes across the cell, which can, in some instances, degrade performance [30]. Furthermore, while the optical cell is pivotal in enhancing the technique's sensitivity, it also poses limitations when it comes to realizing compact and portable optical gas sensors, primarily due to its size, weight, and sensitivity to misalignments. Nevertheless, over recent years, many robust portable sensors utilizing multipass cells have been successfully demonstrated and developed [31], [32].

An alternative approach to enhancing the sensitivity of laser absorption spectroscopy lies in cavity-enhanced methods, specifically Cavity Ring Down Spectroscopy (CRDS) and Cavity Enhanced Absorption Spectroscopy (CEAS). In CEAS, the gas cell is structured as a high-finesse optical cavity, and exceptionally long pathlength cells can be created by using mirrors with high reflectivity ($R > 99.99\%$), attainable through dielectric coatings. Resonant cavities are constructed akin to high-finesse Fabry-Perot etalons. However, it's important to note that cavity-enhanced techniques are susceptible to misalignment issues since the linewidth and spectral purity of longitudinal cavity modes can deteriorate due to suboptimal matching between the laser beam path outside the cavity and the light propagation within the cavity itself. Consequently, these techniques demand laser beams characterized by high spatial quality and narrow linewidth. The trade-off for achieving an extremely high sensitivity, down to the level of parts per quadrillion [33 - 35], is a significant increase in optical path lengths, overall sensor size, and complexity. The incorporation of a phase-sensitive scheme in CEAS [36] has proven highly effective in enhancing detection sensitivity by mitigating sources of noise arising from laser power fluctuations and shot-to-shot variations in power injection during each resonance.

OA-ICOS, a variation of CEAS, employs radiation injected at a minute angle in relation to the cavity axes. This setup results in the creation of a closely spaced array of weak optical axial modes, rendering the entire system more resilient against instability in both the cavity and laser spectrum [37]. While this approach significantly reduces alignment challenges, it still grapples with limitations such as low transmissivity and intensity fluctuations arising from partial excitation of high-order transverse modes. These high-order modes are essential in the on-axis configuration (CEAS) but serve as a noise source in the case of OA-ICOS. Furthermore, even for OA-ICOS, the tunability range remains quite narrow. Both multi-pass cells and optical cavities must be combined with optical detectors. The utilization of widely tunable laser sources or arrays of lasers for analysing gas mixtures, which may contain numerous broadband absorbers, is typically unfeasible, especially in the context of CEAS-based sensors.

CRDS, on the other hand, operates on the principle of measuring the rate of light intensity decay within a stable optical resonator known as the ring-down cavity (RDC) [38]. In a typical CRDS setup, a laser source is initially tuned to resonate with one of the cavity modes, and the laser emission is introduced into the RDC before being switched off. Subsequently, the transmitted radiation from the cavity exhibits exponential decay over time, with a decay rate directly proportional to the cumulative optical losses within the RDC. Highly sensitive detectors with kHz bandwidths are employed to measure the decay time. Sources of losses within the cavity encompass mirrors with reflectivity less than 100%, scattering losses, and alignment imperfections. If the cavity contains the target gas, additional losses due to spectral absorption manifest. The exponential decay of the measured signal can be mathematically expressed as:

$$I(t) = I_o \exp\left(-\frac{t}{\tau} - \alpha n t\right) \quad (1.3)$$

By analysing the attenuation pattern of radiation within the cavity, it becomes possible to determine the concentration of the gas. The primary advantage of CRDS is its capability to achieve an effective optical path of several kilometres, enabling sensitivities in the part-per-trillion (ppt) range with integration times spanning several seconds [39]. However, there are significant limitations, including the stringent demands for precise alignment and the restricted tunability range due to challenges associated with matching the laser emission wavelength to the cavity parameters. Additionally, system drifts between successive ringdown events [40] and noise may arise as a result of the excitation of multiple cavity modes by pulsed sources with broad linewidths [41]

	Sensitivity	**Selectivity**	**Compactness and portability**	**Stability**	**Cost**
Chromatography spectrometry	ppb	perfectly determine one species among the rest	bad	poor	poor
Semiconductor spectroscopy	ppb	selective for some species	excellent	good	excellent
Electrochemical sensors	ppm	determine one species among others; cross-selectivity might occur	good	bad	good
TDLAS	ppt	determine one species among others; cross-selectivity might occur	bad	good (influence of external noise)	poor
Multi-pass and cavity-enhanced optical sensors	ppt	determine one species among others; cross-selectivity might occur	bad	poor	poor
Photoacoustic spectroscopy	ppt	perfectly determine one species among the rest	poor	excellent	poor

Table 1.1 Comparison of different gas sensing techniques

To sum up all the above, Table 1.1 presents the comparison between all the main techniques for the gas sensing existent on the market, including the photoacoustic spectroscopy which will be in

details described in Chapter 5. As can be seen from the table, photoacoustic spectroscopy is the most promising way for the environmental detection of toxic gases and has best agreement between sensitivity and selectivity comparing to other gas sensing techniques, but still suffers on side of cost, compactness and portability. In these theses (precisely in chapter 5) the work towards the development of more compact and portable module for the quartz enhanced photoacoustic spectroscopy will be presented to push forward even more the photoacoustic spectroscopy competitiveness on the market.

References

[1] Gordon, L. Rothman, C. Hill, R. Kochanov, Y. Tan, P. Bernath, M. Birk, V. Boudon, A. Campargue, K. Chance, "The HITRAN2016 molecular spectroscopic database", J. Quant. Spectrosc. Radiat. Transf. 203, 3–69 (2017)

[2]W. Ramsay, A Determination of the Amounts of Neon and Helium in Atmospheric Air, Proc. R. Soc. Lond. A76111–114. (1905).

[3] H.H. Strain, J. Sherma, Adsorption Analysis and Chromatographic Methods, J. Chem. Educ. 24 (1967) 238–242.

[4] A.T. James, J.P. Martin, Gas-liquid partition chromatography: the separation and micro-estimation of volatile fatty acids from formic acid to dodecanoic acid., Biochem. J. 50 (1952) 679.

[5] L.S. Ettre, Nomeclature for chromatography, Pure Appl. Chem. 65 (1993).

[6] H.M. McNair, J.M. Miller, N.H. Snow, Basic gas chromatography - Third Edition, John Wiley & Sons, Ltd, 2019.

[7] D.O. Sparkman, Z.E. Penton, F.G. Kitson, Gas chromatography and mass spectrometry : a practical guide - 2nd Edition, Elsevier, 2011.

[8] Špánik, I, Machyňáková, A. Recent applications of gas chromatography with high-resolution mass spectrometry. *J Sep Sci*. 2018; 163–179. https://doi.org/10.1002/jssc.201701016

[9] B. C. Kaanta, H. Chen, G. Lambertus, W. H. Steinecker, O. Zhdaneev and X. Zhang, "High Sensitivity Micro-Thermal Conductivity Detector for Gas Chromatography," *2009 IEEE 22nd International Conference on Micro Electro Mechanical Systems*, Sorrento, Italy, 2009, pp. 264-267, doi: 10.1109/MEMSYS.2009.4805369.

[10] F.J. Santos, M.T. Galceran, The application of gas chromatography to environmental analysis, TrAC - Trends Anal. Chem. 21 (2002) 672–685.

[11] R. Porter, ed., Gas chromatography in biology and medicine, J. & A. Churchill, 2009.

[12] M. Lorenzo, Y. Pico, Gas Chromatography and Mass Spectroscopy Techniques for the Detection of Chemical Contaminants and Residues in Foods, in: Chem. Contam. Residues Food Second Ed., Woodhead Publishing, 2017: pp. 15–50.

[13] D.S. Hage, Chromatography, in: Princ. Appl. Clin. Mass Spectrom. Small Mol. Pept. Pathog., Elsevier, 2018: pp. 1–32.

[14] S. R. Morrison, “Semiconductor Gas Sensors,” 1982.

[15] M. V. Nikolic, V. Milovanovic, Z. Z. Vasiljevic, and Z. Stamenkovic, “Semiconductor gas sensors: Materials, technology, design, and application,” Sensors (Switzerland), vol. 20, no. 22. MDPI AG, pp. 1–31, Nov. 02, 2020. doi: 10.3390/s20226694.

[16] X. Liu, S. Cheng, H. Liu, S. Hu, D. Zhang, and H. Ning, “A survey on gas sensing technology,” Sensors (Switzerland), vol. 12, no. 7. pp. 9635–9665, Jul. 2012. doi: 10.3390/s120709635.

[17] “Figaro Engineering Inc.” https://www.figaro.co.jp/en/

[18] S. Mao, G. Lu, and J. Chen, “Nanocarbon-based gas sensors: Progress and challenges,” Journal of Materials Chemistry A, vol. 2, no. 16, pp. 5573–5579, Apr. 2014, doi: 10.1039/c3ta13823b.

[19] S. Mao, G. Lu, and J. Chen, “Nanocarbon-based gas sensors: Progress and challenges,” Journal of Materials Chemistry A, vol. 2, no. 16, pp. 5573–5579, Apr. 2014, doi: 10.1039/c3ta13823b.

[20] J. T. W. Yeow and Y. Wang, “A review of carbon nanotubes-based gas sensors,” Journal of Sensors, vol. 2009. 2009. doi: 10.1155/2009/493904. 172

[21] R. - Emerson, “Electrochemical vs. Semiconductor Gas Detection-a Critical Choice.”

[22] “Electrochemical Sensors,” 1988. Accessed: May 27, 2021. [Online]. Available: http://www.intlsensor.com -> electrochemical.pdf

[23] J. Hodgkinson, R.P. Tatam, Optical gas sensing: A review, Meas. Sci. Technol. 24 (2013) 012004.

[24] J. Li, B. Yu, W. Zhao, W. Chen, A Review of Signal Enhancement and Noise Reduction Techniques for Tunable Diode Laser Absorption Spectroscopy, Appl. Spectrosc. Rev. . 49 (2014) 666–691.

[25] P. Werle, F. Slemr, K. Maurer, R. Kormann, R. Mücke, B. Jänker, Near- and mid-infrared laser-optical sensors for gas analysis, Opt. Lasers Eng. 37 (2002) 101–114

[26] J. U. White, “Long Optical Paths of Large Aperture.”

[27] D. Herriott, H. Kogelnik, and R. Kompfner, “Off-Axis Paths in Spherical Mirror Interferometers.”

[28] S. M. Chernin and E. G. Barskaya, “Optical multipass matrix systems,” 1991.

[29] B. Tuzson, M. Mangold, H. Looser, A. Manninen, and L. Emmenegger, “Compact multipass optical cell for laser spectroscopy,” 2013. [Online]. Available: www.nanotera.ch 173

[30] P. Werle and F. Slemr, “Signal-to-noise ratio analysis in laser absorption spectrometers using optical multipass cells,” 1991.

[31] L. Dong et al., “Compact TDLAS based sensor design using interband cascade lasers for mid-IR trace gas sensing,” Optics Express, vol. 24, no. 6, p. A528, Mar. 2016, doi: 10.1364/oe.24.00a528.

[32] T. I. Yacovitch et al., “Just Accepted Manuscript • Publication Date (Web),” 2014. [Online]. Available: http://pubs.acs.org

[33] I. Galli et al., “Molecular gas sensing below parts per trillion: Radiocarbon-dioxide optical detection,” Physical Review Letters, vol. 107, no. 27, Dec. 2011, doi: 10.1103/PhysRevLett.107.270802.

[34] L. Xiong et al., “Photoacoustic trace detection of gases at the parts-per-quadrillion level with a moving optical grating,” Proceedings of the National Academy of Sciences of the United States of America, vol. 114, no. 28, pp. 7246–7249, Jul. 2017, doi: 10.1073/pnas.1706040114.

[35] T. Tomberg, M. Vainio, T. Hieta, and L. Halonen, “Sub-parts-per-trillion level sensitivity in trace gas detection by cantilever-enhanced photo-acoustic spectroscopy,” Scientific Reports, vol. 8, no. 1, Dec. 2018, doi: 10.1038/s41598-018- 20087-9.

[36] M.-C. Chan and S.-H. Yeung, “High-resolution cavity enhanced absorption spectroscopy using phase-sensitive detection,” Chemical Physics Letters, vol. 373, no. 1–2, May 2003, doi: 10.1016/S0009-2614(03)00540-2.

[37] J. B. Paul, L. Lapson, and J. G. Anderson, “Ultrasensitive absorption spectroscopy with a high-finesse optical cavity and off-axis alignment,” 2001.

[38] A. O’Keefe and D. A. G. Deacon, “Cavity ring-down optical spectrometer for 174 absorption measurements using pulsed laser sources,” Review of Scientific Instruments, vol. 59, no. 12, pp. 2544–2551, 1988, doi: 10.1063/1.1139895.

[39] Z. Li, R. Hu, P. Xie, H. Wang, K. Lu, and D. Wang, “Intercomparison of in situ CRDS and CEAS for measurements of atmospheric N2O5 in Beijing, China,” Science of the Total Environment, vol. 613–614, pp. 131–139, Feb. 2018, doi: 10.1016/j.scitotenv.2017.08.302.

[40] A. Foltynowicz, F. M. Schmidt, W. Ma, and O. Axner, “Noise-immune cavityenhanced optical heterodyne molecular spectroscopy: Current status and future potential,” in Applied Physics B: Lasers and Optics, Sep. 2008, vol. 92, no. 3 SPECIAL ISSUE, pp. 313–326. doi: 10.1007/s00340-008-3126-z.

[41] T. G. Spence, C. C. Harb, B. A. Paldus, R. N. Zare, B. Willke, and R. L. Byer, “A laser-locked cavity ring-down spectrometer employing an analog detection scheme,” Review of Scientific Instruments, vol. 71, no. 2 I, pp. 347–353, 2000, doi: 10.1063/1.1150206.

Chapter 2. Laser sources for gas sensing. State of the art

2.1. History

The spectral range situated in the medium infrared (MIR) region, spanning approximately 2-20 μm, holds considerable appeal for diverse industrial applications. Leveraging lasers within this specific wavelength range introduces the potential to effectively detect numerous toxic gases due to the presence of pronounced absorption lines for such gases in this region. In the field of interest for industrial companies, there are strong absorption lines of toxic gases in the near-IR range such as nitrous oxide (N_2O) at 3484 cm^{-1} (2.87 μm), nitrogen dioxide (NO_2) at 2919 cm^{-1} (3.4 μm), methane (CH_4) at 3030 cm^{-1} (3.3 μm) and 4421 cm^{-1} (2.20 μm). And even higher demand is for detection of extremely hazardous gases, which can lead to big health issues or even death, such as hydrofluoric acid (HF) (exposure limit is 3 part per million (ppm) for 15 minute exposure time) with the strong absorption lines around 2.34 - 2.82 μm, hydrogen chloride (HCL) (exposure limit 5 ppm) around 3.5 μm or carbon monoxide (CO) (exposure limit 50 ppm) around 2.34 μm. Hence, the imperative lies in the development of highly effective spectroscopic sources operating within the near and mid infrared (mid-IR) range. Within the context of this thesis, the primary focus is directed towards the advancement of a bespoken Type-1 Distributed Feedback (DFB) laser sources with a wavelength emission at 2.4 μm, engineered from GaSb materials.

2.2. Laser's types

Typically, there are three primary semiconductor laser technologies that utilize quantum wells within their active regions and find widespread application in the generation of medium infrared (mid-IR) laser sources. These technologies encompass interband lasers, interband cascade lasers (ICLs), and quantum cascade lasers (QCLs). It is important to note that when classifying these

laser sources, we consider three distinct types of band alignment within the quantum wells, as illustrated in Figure 2.1.

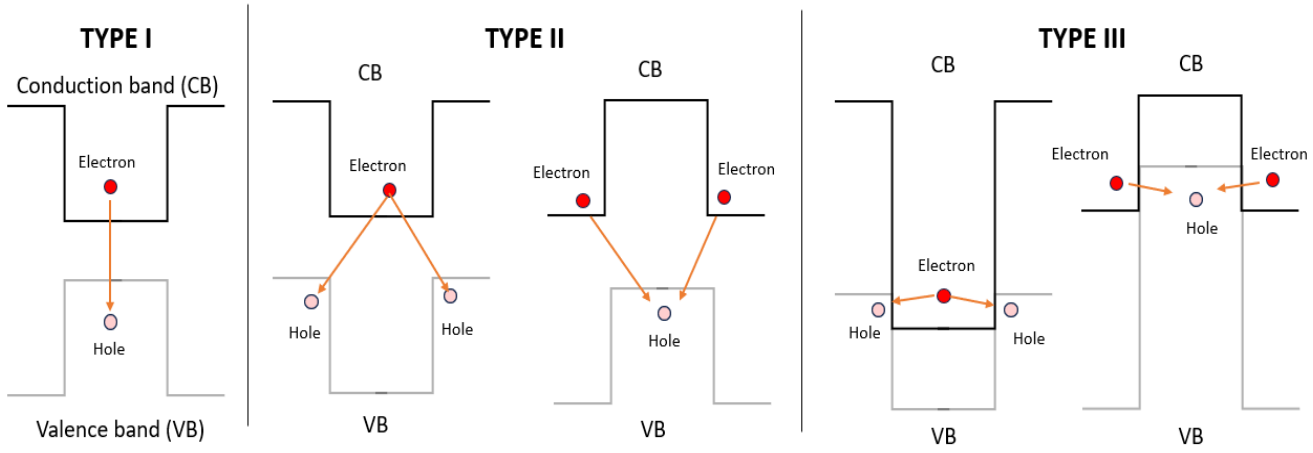


Figure 2.1. Types of band alignment in lasers

Lasers of Type-I feature a quasi-two-dimensional density profile, with all carriers confined within the same layer. A noteworthy characteristic of Type-I lasers is the nearly complete overlap of wavefunctions, approaching 100% overlap. In contrast, for other laser types, the conduction band of one material may either intersect with the band gap (Type-II) or reside below the valence band of the adjacent layer (Type-III). In the case of Type-II and Type-III lasers, both electrons and holes are confined within the adjacent layers, leading to significantly reduced wavefunction overlap compared to Type-I lasers, meaning reduced overlap between the electron and hole wavefunctions within the semiconductor layers, which affects the efficiency of the laser's light-emitting capabilities. However, it's worth noting that these lasers often possess energy gaps that are lower than the energy gap of each individual material, impacting their spectral properties.

2.2.1 Laser diodes

Lasers which will be described in this thesis are Type-I laser diodes with active zone based on QWs. Emission wavelength of such sources depend not only on the material (setting the band gap energy) and resonant cavity (selecting resonant modes) but also on the properties of QWs (adjusting the different energy levels and increasing the gaps between them, meaning changing the quantification within the QW). Targeting infrared spectral range, it is common to use materials of III-V zinc-blend alloys as low bandgap allows these materials to operate at lower energy levels, resulting in efficient light emission. Specifically, NANOMIR group in Montpellier is focused on antimonide materials, such as gallium antimonide (GaSb), indium antimonide (InSb), aluminium antimonide (AlSb), indium arsenide (InAs), and their ternary or quaternary alloys. The first reported lasers based on antimonide materials were introduced in 1980 by Kobayashi [1] and it was done by means of liquid phase epitaxy and lasers were emitting around 1.8 μm. Later on, starting from 1991, began to appear devices using GaSb as a substrate [2]. Nowadays GaSB-based lasers are made with the help of MBE (Molecular Beam Epitaxy). MBE is a technique which deposits thin crystal layers on the given substrate. The deposition is realized in a chamber under vacuum (10^{-10} Torrs) and at high temperature (approximately 480°C). The structural configuration of these lasers can be described in terms of their band structure, resembling a P-N junction situated between two wide-gap materials, often referred to as "claddings layers." These claddings layers, both upper and lower, are typically of the same width, measuring approximately 1.3-1.5 μm. They are characterized by a high concentration of aluminium (ranging from 65% to 90%), which serves to widen the band gap facilitate the confinement of charge carriers within the active region and act as waveguides for the emitted light.

The active zone within these lasers comprises an intermediate gap medium with the primary function of confining the carriers. It also has a high optical index, enabling it to confine the electromagnetic field effectively. This active zone features embedded quantum wells, constructed from materials with smaller band gaps. These quantum wells are responsible for capturing and retaining electrons and holes at quantized energy levels, facilitating their radiative recombination.

In standard structures, like ones we studied in current thesis, active zone has two GaInAsSb QWs of 10 -15 nm width, an AlGaAsSb barrier 250 nm thick between them and on both sides of active

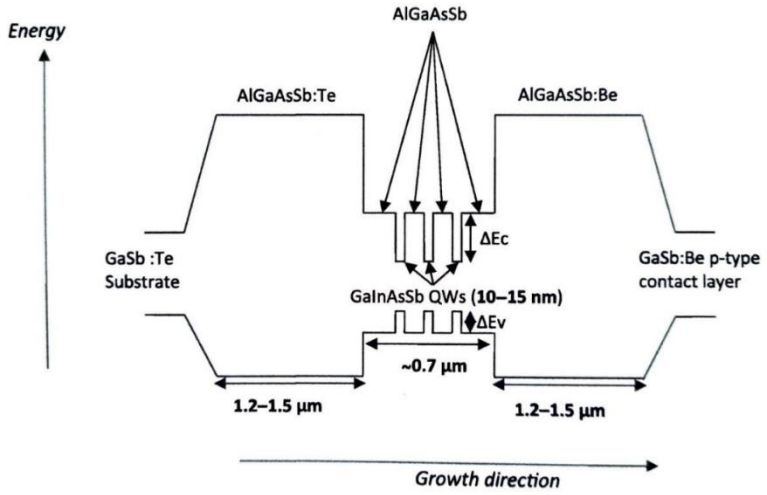


Figure 2.2. Band structure of Type-I QW laser diodes emitting in MIDIR [3]

zone there are two waveguide layers (about 380 nm) with the same composition as barrier layer. On the top of the structure there is a "top contact ", an highly p-doped GaSb layer, which acts as p-contact and typical thickness is about 350 nm. You can observe the standard band profile of such laser heterostructure on Fig. 2.2.

2.2.2 Quantum Cascade Lasers (QCLs)

Next laser sources which are very common in use for gas sensing, due to high emitting power, are Quantum Cascade Lasers (QCLs), which are devices where electronic transitions between the sub bands are confined in the heterostructure conduction band. The history of such sources

started back in 1971, when two scientists from Soviet Union stated the existence of gain phenomenon in a semiconductor superlattice [4]. The laser source itself was developed in USA by the group lead by Federico Capasso. [5]. The multilayer configuration found in Quantum Cascade Lasers (QCLs) comprises a semiconductor superlattice, which consists of a series of quantum wells interspersed with potential barriers. The injector in Quantum Cascade Lasers plays a central role in facilitating the injection of electrons into the active region of the laser, helping create the necessary conditions for laser emission. Its design and operation are critical for achieving the desired laser performance, including wavelength tuning and efficiency. What sets QCLs apart is that the emitted wavelength is not governed by the band gap within the active region, as is the case in quantum wells lasers. Instead, it is determined by the geometric characteristics of the superlattice, the thickness of the potential barriers and the dimensions of the quantum wells.

Another notable distinction between QCLs and conventional lasers lies in their utilization of either electrons or only holes during the emission process. To go further into their operation, let's now explore the fundamental operating principle of QCLs. Quantum Cascade Lasers (QCLs) are constructed through the precise layering of semiconductor materials with distinct energy band structures. These layered structures incorporate multiple quantum wells (QWs). Within each quantum well, there exists a nanoscale confinement region where the energy levels available to electrons become discrete and quantized. This quantization is a direct consequence of the confined electron motion within the narrow boundaries of the quantum well. The specific energy spacing between these discrete levels is intricately controlled, determined by factors such as the layer's thickness and material characteristics. Each device can be divided into 2 main parts:

active region and injection/relaxation part. Very efficient QCLs can be found emitting at 8 μm [6].

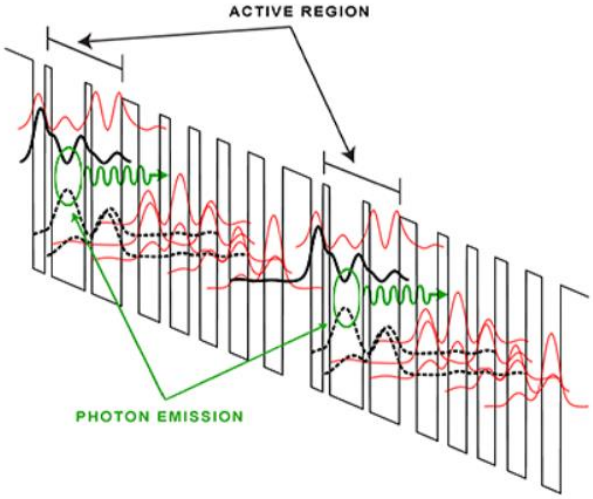


Figure 2.3. Schematic representation of QCL structure [7]

2.2.3 ICLs

Another efficient technology for laser operation is the interband cascade lasers (ICLs). This technology combines main advantages from laser diodes (long upper-level recombination lifetime – is time, during which in the absence of stimulated emission conditions, electrons and holes may coexist in proximity to one another, before recombining) and from QCLs (voltage efficient scheme reproducing cascade) (Figure 2.4). These sources were invented in 1994 [8] but received poor support from the scientific community Following extensive research efforts and the integration of a hole injector into the concept [9], the first operational Interband Cascade Laser (ICL) was unveiled in 1997 [10]. It's worth noting that this early ICL design had limitations, as it could only achieve lasing action at cryogenic temperatures. This was primarily

attributed to the design choices made during that era, including the excessive thickness of the electron injector, which led to elevated threshold current densities and low external differential quantum efficiencies per stage [11]. Later, between 1998 and 2000, ICLs with improved solutions and better performances at different temperatures were shown leading to future developments [12-14].

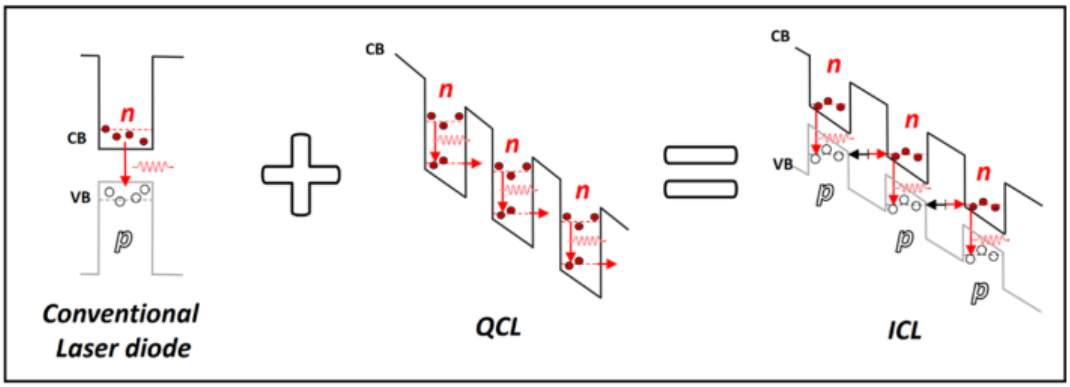


Figure 2.4. Operating principal of ICLs [15]

2.3. Single-frequency laser sources in MIR

As already stated above, one of the main applications for laser sources is gas sensing, there are several requirements for laser sources in this industry: precise selection of target wavelength, narrow laser line width (10-12 - 10-11 meters) to have good spectral resolution and avoid cross-interference, fast wavelength tuning (current tuning can achieve speeds in the range of tens to hundreds of megahertz) to have a real-time gas monitoring and detection of dynamic gas mixtures and output power of more than 5 mW as in some techniques the signal is in linear

proportion to laser output power. Single mode operation is fundamental property for all gas sensors based on absorption spectroscopy.

The term "single-mode operation" in the context of lasers can be interpreted in two distinct ways:

- Single-Longitudinal-Mode Operation: In this interpretation, "single-mode operation" refers to the laser emitting radiation with an extremely narrow linewidth, often only a few kilohertz wide. This results in a long coherence length. This type of single-mode operation is defined by the laser's free spectral range, as previously explained. It means that the laser predominantly operates in a single longitudinal mode, with the emitted photons having nearly identical optical frequencies.
- Single-Transverse-Mode Operation: In this context, "single-mode operation" means that the laser operates in a single transverse or spatial mode, which is typically a Gaussian-shaped mode. However, it's important to note that laser oscillation may still occur simultaneously in multiple longitudinal (or axial) modes. These longitudinal modes have essentially the same transverse spatial shape but differ in their optical frequencies, and they are separated by the free spectral range.

In summary, the term "single-mode operation" can have two distinct meanings in laser physics: one relates to the narrow linewidth and coherence length due to single-longitudinal-mode operation, and the other pertains to the dominance of a single transverse mode while potentially allowing multiple longitudinal modes to coexist within the laser cavity. These interpretations are based on the specific aspects of laser behaviour that are emphasized.

Regrettably, while Fabry-Perot lasers may exhibit single-mode operation under specific conditions, such as precise injection, temperature control, and specific spectral requirements,

their performance remains inconsistent and unreliable for dependable sensor applications. To address this challenge, efforts were made to create devices leading to single frequency emission. The first Distributed Feedback laser diodes (DFB) were pioneered in 1971 by Kogelnik [16]. Later, a single mode component named a vertical-cavity surface emitting laser (VCSEL) was introduced by Prof. Emeritus K. Iga of Tokyo Institute of Technology in 1977 [17]. Such single mode devices as VECSELs were introduced in 1997 by Kuznetsov [18]. Upon a comprehensive analysis of the afore mentioned technologies, we have arrived at the determination that DFB laser sources are the best choice for applications in compact gas sensors. This choice is rooted in the fact that VCSELs emit extremely low powers, typically not exceeding 1 mW, within the targeted spectral range. Additionally, VECSELs are deemed unsuitable due to the constraints posed by optical pumping, which would hinder our goal of achieving a compact system.

In contrast, DFB lasers have demonstrated favourable characteristics in various spectral ranges, boasting a robust theoretical foundation and a relatively straightforward fabrication process. These attributes make DFB lasers the most suitable choice for our specific needs.

Very first DFB source was presented in 1971 by H. Kogelnik [16], emitting at 630 nm, but first semiconductor DFB laser which had low-temperature operation was developed around same time by Nakamura in 1973 [19]. It is only by the end of the 1970s that were presented first semiconductor DFB lasers operating at room temperature on

GaAs substrate [20-22].

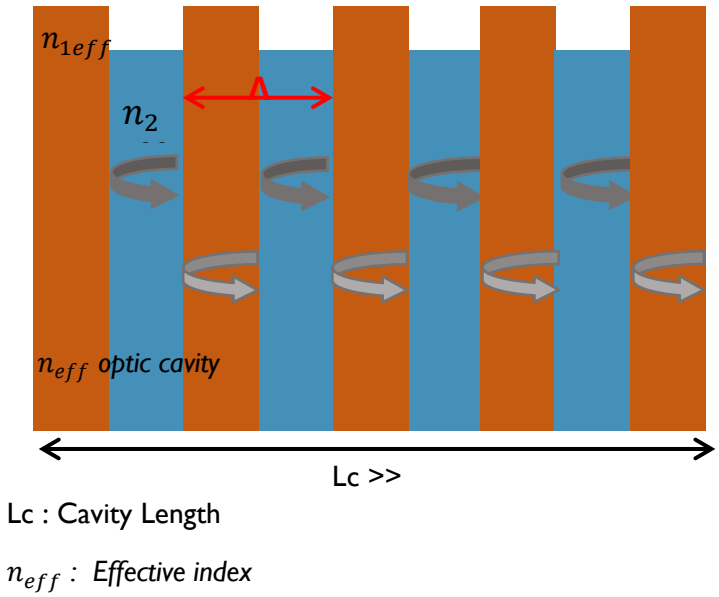


Figure 2.5. Schematic representation Bragg grating's

The Bragg grating functions as a filter for Fabry-Perot modes. It is constituted by structure composed of two materials with alternating refractive indices, as illustrated in Figure 2.5. Electromagnetic waves that fulfil the Bragg condition, as they propagate through such a structure, experience partial reflections at each interface between the two materials. The strength of these reflections is influenced by the magnitude of the refractive index difference between the two materials. These reflections give rise to both destructive and constructive interference patterns. Importantly, these reflections at each interface of the index grating serve to prolong the lifetime of photons within the specific longitudinal mode confined in the cavity. This extended photon lifetime results in an abundance of photons within this particular mode. Consequently, this mode surpasses the efficiency of radiative recombination when compared to other modes present in the Fabry-Perot cavity.

Below one can find the Bragg condition itself:

$$\Lambda = m\frac{\lambda_B}{2\, n_{eff}} \quad (2.1)$$

Where Λ is a grating period, m is a grating order, λ_B is the wavelength which is needed to be filtered by grating and n_{eff} is the waveguide refractive index.

Two standing waves are allowed perpendicular to the Bragg grating. The energy difference between these two modes is called the forbidden band gap. This band corresponds to the frequencies for which the reflections in the DFBs are not constructive but are destructive. The bandgap width is defined in terms of frequency according to the relationship:

$$\Delta\omega = \frac{2\kappa c}{n_{eff}} \quad (2.2)$$

$\Delta\omega$ is the difference in pulsation of the two modes, κ is the coupling factor, c is the speed of light in a vacuum and n_{eff} is the average effective index of the two lattice modes.

Considering previous equations, the coupling factor can be defined as:

$$\kappa = \frac{\Delta w}{2 * c} * n_{eff} \quad (2.3)$$

Mode with higher gain is selected in the end.

One of the very important parameters for the DFB's evaluations is coupling coefficient, which is multiplication of coupling factor on laser's length (κL) and play on the distribution of the field along the cavity length. The distribution of the relative intensity of the coupling coefficient κL is presented on the figure (Figure 2.6). As I already mentioned before – bigger the difference between the refractive indexes between two media – more efficient reflections are. And when reflections are weak, the coupling is weak as well and then coupling coefficient is less than 1. For this regium the intensity of the mode is bigger in the edges of the cavity, than in the middle

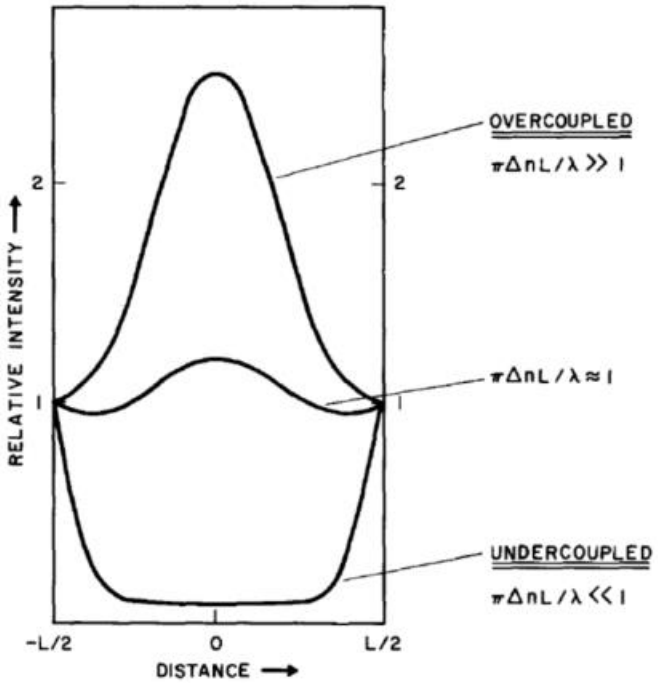


Figure 2.6. Spatial distribution of the relative intensity of the optical field in a laser cavity [23]

and it is called "under coupled" regime. In this regium the leaking of extra modes except the chosen one is possible and single mode operation cannot be ensured. When value $\kappa L >> 1$, it leads to "over-coupled" regime, when contrast of refractive indexes is too big and reflections appear to be too strong. This situation leads to too big confinement of mode in the cavity and emitted optical power can be really low. For perfect lasing conditions the distribution of field

strength should be same in the center of the cavity and on the edges and it would respond to the coupling coefficient of 1.

DFB structures can be implemented gratings of different orders (more common 1st, 2nd, 3d orders). Higher order gratings are much easier in fabrication, as require lower resolution for grating determination due to bigger grating periods, but at the same time they have more diffractive losses [24]. First order gratings have good coupling only if duty cycle of the grating is around 0.5, and in higher order gratings the situation is different. For grating of second order the optimal coupling can be achieved at 0.25 and 0.75 (Fig 2.7), and for the third order – at 0.2, 0.5 and 0.8 [25]. These values were achieved but device with buried grating emitting at 2.3 μm, with refractive index of claddings 3.182 and of waveguides 3.62 [26]. Coupling will also differ a lot according to different depths of etching for different grating's orders. All the above should be taken into consideration before designing the wanted structure.

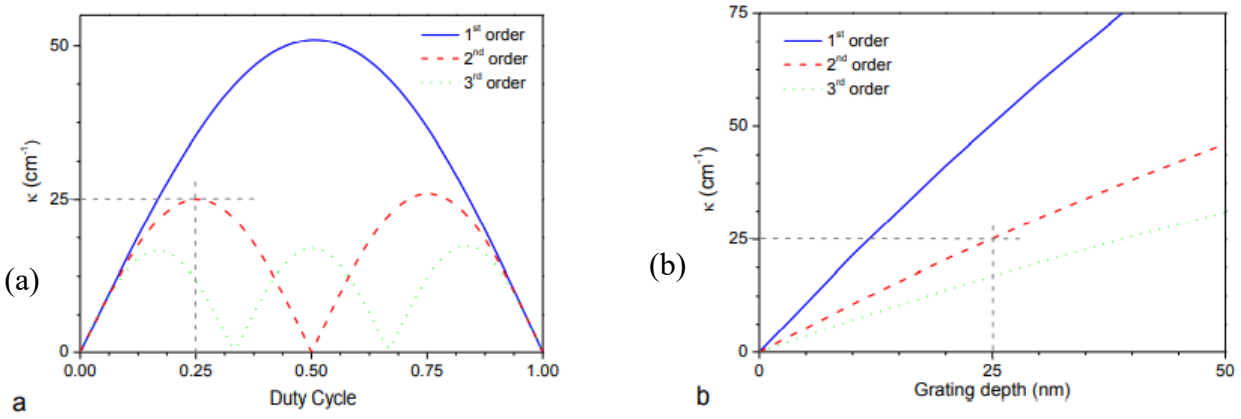


Figure 2.7.(a) - Coupling factor dependance on duty cycle of the grating; (b) – Coupling factor dependance on depth of etching [25]

2.3.1. DFB lasers with lateral grating along the ridge

Discussion on different DFB's designs will start with the technique which is well spread on the market among GaSB-based lasers – chromium grating along the ridge (Figure 2.8). Using lateral coupling of the guided mode to a first order grating made from Cr lead to a periodic modulation of the losses in the cavity and the coupling of the evanescent part of the mode happens [26]. This way of grating's implementation doesn't depend on used material and can be implied in all laser's structures (GaAs, InP, GaSb). This technique was able to perform side-mode suppression ratio (SMSRs) bigger than 30 dB at different wavelengths, with later focusing on spectroscopic needs in MidIR with examples of lasers emitting at 2.3 μm [27], 2.6 μm [28,29] as well as lasers with wavelength above 3 μm showed good performance [30,31]. Important to mention that lateral metal grating introduce additional losses that lower device performance. This technique is widely used commercially and at the moment the main technique implemented on DFB laser diodes in industrial German company Nanoplus GmbH.

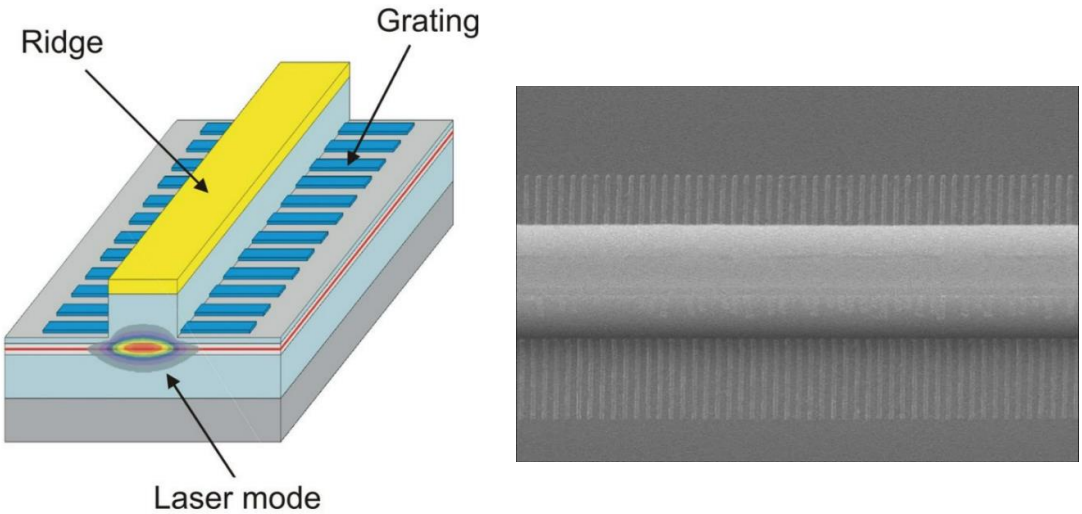


Figure 2.8. Schematical representation and photo of the DFB laser with the grating along the ridge [32]

2.3.2. DFB lasers with corrugation of the side walls.

Next technique of DFB production is lateral sidewall corrugation (Figure 2.9). Trying to overcome disadvantages of the previous technique (introduction of additional losses due to presence of metal grating) another way was to modulate dielectric function while maintaining low guided mode losses. It is done by varying the real part of the index with a corrugation of the sidewalls of the laser ridge. So periodic pattern of a few hundred nanometres wide and a few microns long is etched into the mesa sidewalls on both sides. This way of grating's implementation was inspired by work carried out on ICLs with higher order gratings [33]. The first results on DFBs with grating on the ridge sidewalls ever was presented with laser having a 3d order grating and made from GaInSb/Gasb materials and the emitting wavelength was 1.9 μm [34]. Later, successful lasers emitting at longer wavelengths going up to 3.3 μm were developed. [35-39]. Groups were also implementing gratings of higher orders (from 2nd to 6th) in their devices by means of nanoimprint, contact, holography or i-line lithography. Talking about fabrication, it is important to mention that for single-mode emission to be possible, one should

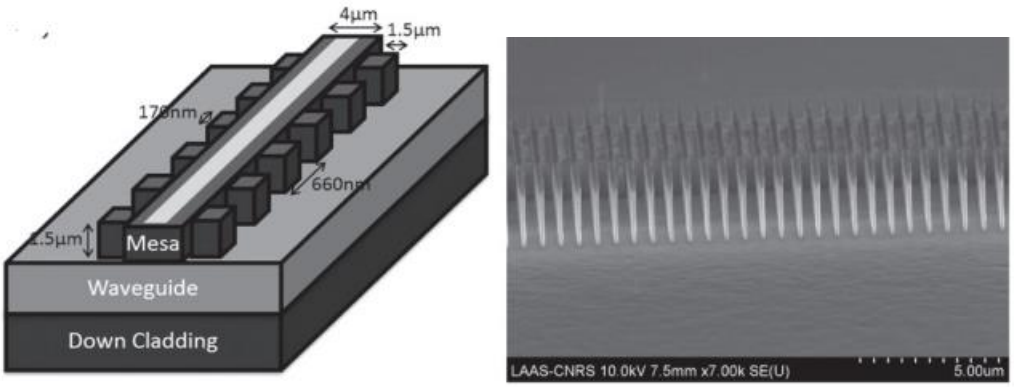


Figure 2.9. Schematical representation and photo of the DFB laser with the corrugated side walls [38]

assure to have straight etching sides without any angles [40]. Performance in terms of power (24 mW) and SMSRs (30 dB) [25] is very similar to the lateral metal-gratings.

2.3.3. DFB lasers with buried grating design

Buried grating is another efficient design for implementing periodic structure into device. This method was widely used for manufacturing InP-based telecom lasers [41]. The technology requires stopping the growth process and etching of the grating in the active zone and only after the successful implementation of grating in the structure the regrowth of the remaining layers can be completed. The buried gratings started developing by the devices made on the InP base by [41] and on the GaAs by [42] structures with buried grating on GaSb were carried out first time only in 2014 [43] with second order grating emitting at 2.2 μm and with first order grating emitting at 3 μm. SMSRs was 30 dB and having power of tens mW.

2.3.4. DFB lasers with grating on the top of the laser ridge

The last technique to mention is the implementation of grating on the top of the laser ridge, which technique will be explored experimentally later on in current manuscript. The schematic representation of such device and photo of fabricated grating are shown on Fig.2.10. The first periodic grating etched into the top of the laser ridge was developed and demonstrated for a laser emitting in the near infrared in 2000 by R. Kohler [44]. Brilliant results on QCLs with top grating were realized in our group in Montpellier by Z. Loghmari in 2018 [45]. There reason why this design is not so well spread among modern DFB laser diodes is that there are a lot of complications with the design and realization of such structures. The first one is the complex fabrication process, as grating needs to be assured to stay only strictly on the top of the laser ridge. Metal must be deposited on the etched grating, situated on top of the mesa, to allow

injection of electric power, leading to close distance between the optical mode and the metallic layer. Another big issue about this technique is that grating is too far from the active zone and poor coupling of the mode with the Bragg grating can degrade the laser performance.

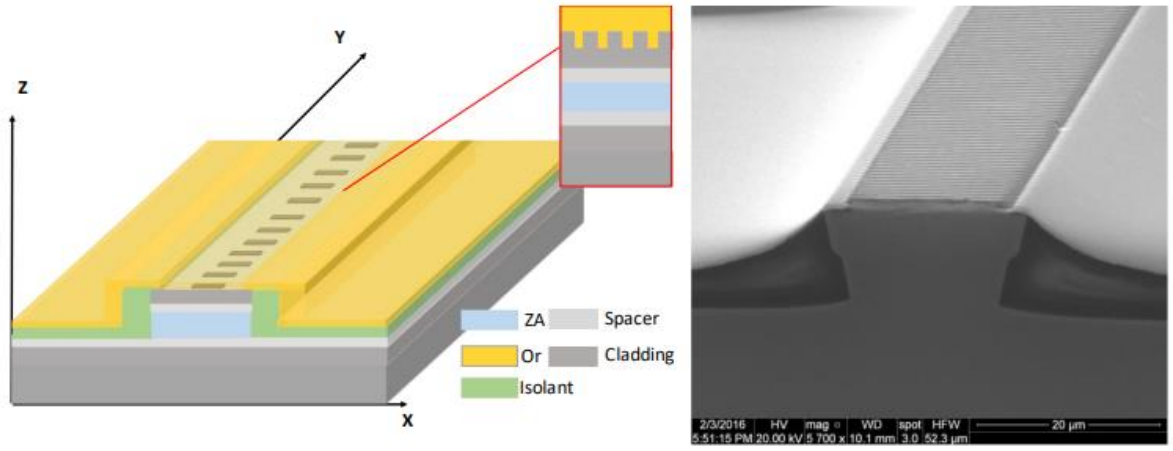


Figure 2.10. Schematical representation and photo of the DFB laser with the grating on the top of the ridge [45]

Coming to conclusion, should be mentioned that DFB laser diodes based on GaSb already have shown good performances in recent years: low threshold currents about 27 mA for 830 μm long device [38] , high output power of 60 mW [25] and solid single mode operation with SMRS of 50 dB [39]. These exceptional performance parameters undoubtedly position GaSb-based DFB laser diodes as highly suitable candidates for a broad spectrum of gas sensing applications. Their combination of low thresholds, high power output, and reliable single-mode operation positions them as valuable tools in this field, offering the precision and sensitivity required for various analytical and environmental monitoring applications. This encompassing capability extends to advanced techniques such as Quartz-Enhanced Photoacoustic Spectroscopy (QEPAS).

References

[1] N. Kobayashi, Horikoshi and Uemura Room temperature operation of the InGaAsSb/AlGaAsSb DH laser at 1.8 μm wavelength Journal of Applied Physics, vol. 19, pp. 30-32, 1980

[2] W.Y. Choi, J.C. Chen and C.G. Fonstad Evaluation of coupling coefficients for laterally-coupled distributed feedback lasers Japanese Journal of Applied Physics Part 1-Regular Papers Short Notes & Review Papers 35 (9A), p.4654, 1996

[3] L. Cerutti, A. Vicet, E. Tournie; Interband mid-infrared lasers; Mid-infrared Optoelectronics, p. 93, 2020

[4] R. Kazarinov. R. Suris, Possible amplification of electromagnetic waves in a semiconductor with superlattice, Sov. Phys. Semivond. 5 (1971) 707 – 709

[5] J. Faist, F. Capasso, D.L. Sivco, C. Sirtori, A.L. Hutchinson, A.Y. Cho, Quantum Cascade Laser, Science 264 (5158) (1994) 553-556

[6] Cherotchenko, E. D. et al. High-Power Quantum Cascade Lasers Emitting at 8 μm: Technology and Analysis. Nanomaterials, 12(22), 3971 (2022)

[7] www.teamwavelength.com/quantum-cascade-laser-basics/

[8] Yang RQ 1995 Infrared laser based on intersubband transitions in quantum wells Superlatt. Microstruct. 17 77- 83

[9] Meyer JR, Vurgaftman I, Yang RQ, and Ram-Mohan LR 1996 Type-II and type-I interband cascade lasers. Electron. Lett. 32 45-46

[10] Lin CH, Yang RQ, Zhang D, Murry SJ, Pei SS, Allerman AA, and Kurtz SR 1997 Type-II interband quantum cascade laser at 3.8 μm Electron. Lett. 33 598-599

[11] Jeremy A Massengale et al 2023 Semicond. Sci. Technol. **38** 025009

[12] Olafsen LJ, Aifer EH, Vurgaftman I, Bewley WW, Felix CL, Meyer JR, Zhang D, Lin CH, and Pei SS 1998 Near-room-temperature mid-infrared interband cascade laser Appl. Phys. Lett. 72 2370-2372

[13] Bruno JD, Bradshaw JL, Yang RQ, Pham JT, and Wortman DE 2000 Low-threshold interband cascade lasers with power efficiency exceeding 9% Appl. Phys. Lett. 76 3167-3169

[14] Yang RQ, Bradshaw JL, Bruno JD, Pham JT, and Wortman DE 2001 Power, efficiency, and thermal characteristics of type-II interband cascade lasers IEEE J. Quantum Electron. 37 282-289

[15] D.A. Diaz Thomas; Design, fabrication and investigation if Interbrand Cascade structures for mid-IR VCSELs; 2020

[16] H. Kogelnik and C. V. Shank Stimulated emission in a periodic structure Appl. Phys. Lett. 18, p.497-499, 1971

[17] K. Iga, "Surface emitting laser", Trans. IEICE C-I, vol. JBl-C-1, no. 9, pp. 483-493, Sep. 1998.

[18] M. Kuznetsov, F. Hakimi, R. Sprague and A. Mooradian, "High-power (>0.5-W CW) diode-pumped vertical-external-cavity surface-emitting semiconductor lasers with circular TEM/sub 00/ beams," in *IEEE Photonics Technology Letters,* vol. 9, no. 8, pp. 1063-1065, Aug. 1997, doi: 10.1109/68.60550

[19] M. Nakamura, H.W. Yen, A. Yariv, E. Garmire, S. Somekh and H.L. Garvin Laser oscillation in epitaxial GaAs waveguides with corrugation feedback Appl. Phys. Lett. 23, p.224-225, 1973

[20] H. C. Casey Jr., S. Somekh and M. Ilegems Room-temperature operation of low – threshold separate – confinement heterostructure injection laser with distributed feedback Appl. Phys. Lett. 27, pp.142-144, 1975

[21] Y. Uematsu, H. Okuda and J. Kinoshita Room temperature cw operation of 1.3μm distributed-feedback GaInAsP/InP lasers Electronics Letters vol.18,pp.857-858, 1982

[22] K. Utaka, S. Akiba, K. Sakai and Y. Matsushima Room temperature cw operation of distributed-feedback buried heterostructure InGaAsP-InP lasers emitting at 1.57μm Electronics Letters vol. 17,pp.961-963, 1981

[23] H. Kogelnik and C. Shank (1972). "Coupled-wave theory of distributed feedback lasers." Journal of applied physics 43(5): 2327-2335

[24] Y. Yamamoto, T. Kamiya, H. Yanai, Improved coupled mode analysis of corrugated waveguides and alsers, IEEE J. Quantum Electronics 14 (4) (1978) 245

[25] Quentin Gaimard, Diodes lasers DFB à couplage par l'indice émettant entre 2 μm et 3,3 μm sur substrat GaSb, 2014, p. 37

[26] J. Seufert, M. Fischer, M. Legge, DFB laser diodes in the wavelength range from 760 nm to 2.5 um, Spectrochim. Acta A Mol. Biomol. Spectrosc. 60 (14) (2004) 3243.

[27] A. Salhi, D. Barat, D. Romanini, Single frequency Sb-based DFBs emitting at 2.3 um above room temperature for application in tunable diode laser absorption spectroscopy, Appl. Opt, 45 (20) (2006) 4957

[28] K. Rosner, M. Hummer, A. Benkert, Long-Wavelengh GaInAsSb/AlGaAsSb DFB lasers emitting near 2.6 um, Phys. E. 30 (2005), 159-163

[29] D.Barat,, J. Angellier, A. Vicet, Anitmonide DFB lasers emitting above 2.6 um, Electron. Letters 43 (23) (2007) 1281-1282

[30] S. Belanhesene, L. Naehle, M. Fischer, Laser diodes for gas sensing emitting at 3.06 at room temperature, IEEE Photo. Tchnol. Letters 22(15) (2010) 1084

[31] L. Naehle, S. Belahsene, M. von Edinger, Continuous-wave operation of type-I quantum well DFB laser diodes emitting in 3.4 um wavelength range around room temperature, Electronic Letters 47(1) (2011) 46

[32] Seufert, Jochen & Fischer, Merlind & Legge, Marg & Roessner, K. & Werner, R. & Hildenbrand, Jürgen & Herbst, J. & Lambrecht, Armin & Koeth, Johannes. (2008). DFB laser diodes and quantum cascade lasers for sensors in safeguard applications. 10.1117/12.799723.

[33] C. Kim, M. Kim, W. Bewley, J. Lindle, C. Canedy, J. Abell, I. Vurgaftman and J. Meyer (2009). "Corrugated-sidewall interband cascade lasers with single-mode midwave-infrared emission at room temperature." Applied Physics Letters 95(23): 231103.

[34] K. Haring, J. Viheriala. M.R. Vijanen, Laterally coupled DFB InGaSb/GaSb diode lasers fabricated by nanoimprint lithography , Electron letters, 46 (16) (2010) 1146-U76

[35] S.Forouhar, R.M Briggs, C. Frez, High-power laterally coupled DFB GabSb-based lasers at 2 um wavelength. , Appl. Phys. Letters 100 (2012) 0311107

[36] J.A Gupta, A. Bezinger, B.J. Barrios, High-resolution methane spectroscopy using InGaAsSb/AlInGaAsSb laterally-coupled index-grating DFB laser diode at 3.23 um, Electron Letters 48 (7) (2012) 396

[37] R. Liang, T. Hosoda, L. Shterengas, DFB 3.27 um laser diodes with continuous wave output power above 15 mW at room temoerature, Electron Letters 50 (19) (2014) 1378

[38] Q. Gaimard. A. Larrue, M. Triki, 2.2 um to 7.7 um side wall corrugated index coupled DFB GaSB based laser diodes, Semicond. Sci. technol. 30 (2015), 065015

[39] J. Viheriala, K. Haring, S. Suomalainen, High spectral purity high power GaSb based DFB laser fabricated by nanoimpring lithography, IEEE Photon. Technol. Letters 28(11) (2016) 1233

[40] Q. Gaimard (2014b), "Diodes lasers DFB à couplage par l'indice émettant entre 2 μm et 3,3 μm sur substrat GaSb", Universtié de Montpellier.

[41] M. Krakowski, D. Rondi, A. Talneau, Y. Combemale, G. Chevalier, F. Deborgies, P. Maillot, P. Richinn, R. Blondeau and L. D'Auria (1989). "Ultra-low-threshold, high-bandwidth, very-low noise operation of 1.52 um GaInAsP/InP DFB buried ridge structure laser diodes entirely grown by MOCVD." IEEE Journal of Quantum Electronics 25(6): 1346-1352.

[42] H. Casey Jr, S. Somekh and M. Ilegems (1975). "Room-temperature operation of low-threshold separate-confinement heterostructure injection laser with distributed feedback." Applied Physics Letters 27(3): 142-144.

[43] Q. Gaimard, L. Cerutti, R. Teissier and A. Vicet (2014a). "Distributed feedback GaSb based laser diodes with buried grating." Applied Physics Letters 104(16): 161111.

[44] Rüdeger Köhler, Claire Gmachl, Alessandro Tredicucci, Federico Capasso, Deborah L. Sivco, S. N. George Chu, Alfred Y. Cho; Single-mode tunable, pulsed, and continuous wave quantum-cascade distributed feedback lasers at λ≅4.6–4.7 μmλ≅4.6–4.7 μm. Appl. Phys. Lett. 28 February 2000; 76 (9): 1092–1094. https://doi.org/10.1063/1.125987

[45] Z. Loghmari, M. Bahriz, D. D. Thomas, A. Meguekam, H. N. Van, R. Teissier and A. Baranov (2018a). "Room temperature continuous wave operation of InAs/AlSb-based quantum cascade laser at λ∼ 11 μm." Electronics Letters 54(17): 1045-1047.

Chapter 3. Novel GaSb based DFB laser diodes emitting at 2.4 μm. Simulations and Fabrication

For successful fabrication of DFB laser diodes with grating on the top of the laser ridge, several studies have been made. Main goal was to bring grating as close as possible to the active zone by thinning the upper cladding layer, which would lead to increased coupling between grating and laser mode. This change could also introduce additional losses, so the aim was to find the thickness of upper cladding, which would allow to have an agreement between the losses and coupling factor. We started with simulations of the proposed structure in COMSOL Multiphysics, varying the thickness of upper cladding with fixed depth of grating etch, achieving results on losses and coupling factor for each value. When optimal value according to results was estimated – study on depth of grating etch for this thickness of upper cladding was performed. When in theory the agreement for the future design was reached – the fabricated of Fabry Perot laser diodes with different thicknesses of the upper cladding was made to confirm the viability of such thin layers experimentally and prove the achieved trend by simulations. Fabrication of Fabry-Perot laser diodes prior to DFB fabrication on same wafer allow us to make precise estimation of grating period for future DFB lasers based on emitting wavelength of Fabry-Perot samples. Simulations results and performance of Fabry-Perot samples lead to decision of thickness of laser layers and future grating design (grating period, duty cycle and depth of etching). These results were followed by successful fabrication of DFB laser diodes with grating on the top of the laser ridge. In industrial company Nanoplus the process was repeated and DFB with grating along the ridge were fabricated on same wafers for comparison.

3.1. Simulations in COMSOL Multiphysics

The modelling of DFB laser diodes enables us to forecast and examine the optical mode's behaviour when incorporating a Bragg grating into the structure, a critical step for achieving single-mode operation. Through presented simulations in this section, on can gain insight into how various structural parameters, such as layer thicknesses and refractive indexes, as well as different grating configurations, including etching depth, grating period, and duty cycle, influence the laser's modes propagation.

The simulations are tailored to GaSb- based laser diodes emitting at 2.3 μm, featuring a surface grating positioned on the top of the laser ridge. Here will be presented the study on potential impact of altering parameters like the upper cladding thickness and etching depth on losses, coupling factor, confinement factor, and figure of merit. Furthermore, it will be discussed the influence of precision in the Mesa etching process on single-mode operation and confinement factor. Additionally, in this section will be undertaken an analysis of gratings with different orders and duty cycles. These assessments hold significant relevance for the future production of DFB laser diodes with enhanced performance and reliability.

Numerical simulations of the DFB laser diode's structure were performed using COMSOL Multiphysics software. For simulation we used the Electromagnetic waves module (frequency domain)in mentioned software to study the propagation of the electromagnetic field inside the proposed structure.

Modern numerical models provide us with the capability to design novel devices and predict their characteristics without the need for extensive fabrication of numerous test samples. The

simulation is based on the resolution of the Helmholtz equation by the finite element method, as this equation describes the propagation of electromagnetic waves [1].

$$\Delta E + K_o^2 \left(n^2 - n_{eff}\right)E = 0 \qquad (3.1)$$

Where Δ is the Laplacian operator, K_0 is the wave vector of the guided mode, n and n_{eff} are, respectively, the complex index and the effective index of the materials and E is the electric field of guided mode

In Figure 3.1, we observe a longitudinal cross-section of the DFB laser diode's structure, revealing its distinct layers. We made simulation for a GaSb-based DFB laser diode, with AlGaAsSb cladding layers and waveguides and GaInAsSb Quantum Wells separated by AlGaAsSb barrier layers. Structure has p-doped GaSb top contact layer.

	Thickness of layer	Real part of refractive index	Imaginary part of refractive index
Bottom cladding	1.2 µm	3.17	0
Active zone	0.8 µm	3.6	0
Upper cladding	0.1 µm → 0.9 µm, step of 0.1 µm	3.17	0.005
Metal	0.1 µm	1.06	14.4

Table 3.1. Parameters of the structure's layers for the simulation

The grating, depicted as rectangular patterns, is etched into the upper cladding layer. At the uppermost part of the structure, a gold layer for the top contact is placed.

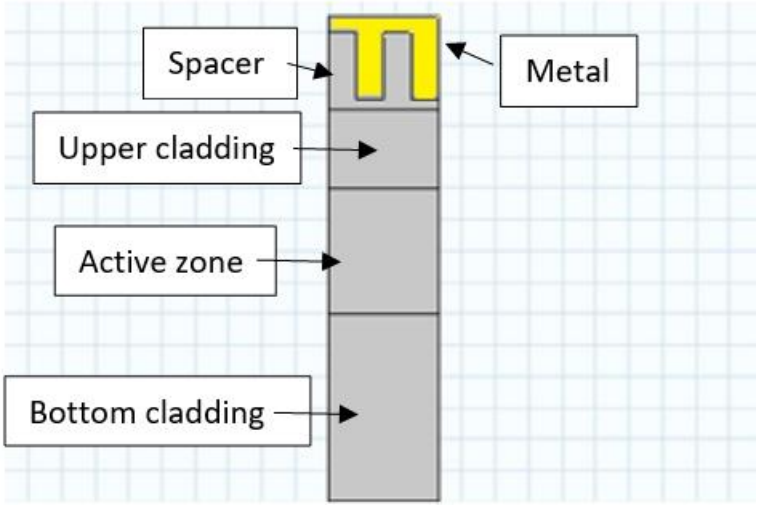


Figure 3.1. Schematic representation of the designed DFB structure

Table 3.1 provides a comprehensive overview of the various constituent layers and their thicknesses that form the device, along with their associated refractive indices, including both the real and imaginary components. The index of the cladding layers is lower than that of the active zone, to allow the light to be confined in the active zone with the highest index. The index of the metallic layer was taken from the Palik book published in 1983 [2]. For the properties of semiconductor layers, we used the data based in NSM archive [3].

3.1.1. Estimation of the optimum design in terms of thickness of upper cladding layer and depth of grating's etch (evaluation of losses, coupling factor and confinement factor)

Several simulations were performed to determine the optimal agreement between coupling factor and losses, trying to vary thickness of upper cladding (from 0.1 μm to 0.9 μm) and different depths of etching for grating (from 0.001 μm to 0.5 μm). Reducing the thickness of the upper cladding layer was expected to enhance the coupling between the grating and the mode. This

adjustment was made because the grating, situated on top of the ridge, is considerably distant from the active zone. The estimated period of first order grating for the wavelength of 2.3 um is 330 nm and it is deduced from the Brag grating condition equation. The simulations were carried out with periodic boundary conditions which make it possible to model an infinite length of the laser cavity. These simulations were performed based on a 2D structure, encompassing both the growth axis and the wave propagation axis.

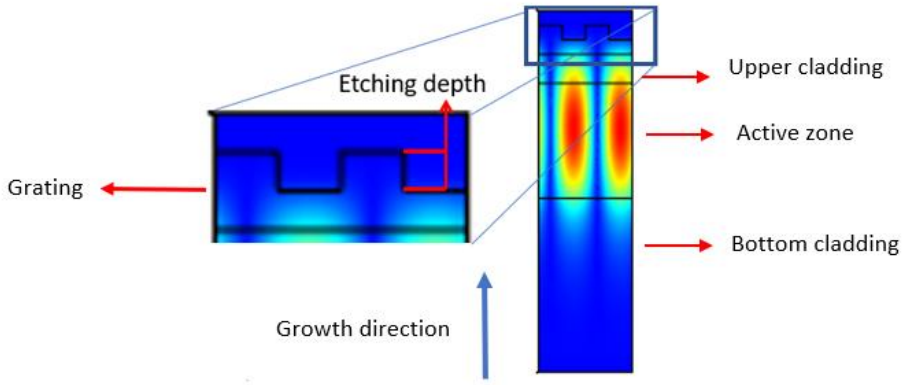


Figure 3.2. Representation of the electromagnetic field distribution in the simulates structure.

Figure 3.2 illustrates the propagation of the electromagnetic field in the 2D simulation of the desired device configuration. These simulations yield intricate oscillations representing the eigenmodes' complex pulsations. These outcomes directly correspond to the eigensolutions derived from the Helmholtz equation. Subsequently, both the real and imaginary components of these two eigenmodes are used to make a deduction of the real refractive index (referred to as "n_{eff}") and the imaginary refractive index (referred to as "k_{eff}").

This comprehensive analysis allows us to gain insights into the behaviour and performance of the device, providing a foundation for optimizing its design and functionality.

COMSOL Multiphysics provides us results of eigenmodes in the following format:

$$v = v_{real} + i * v_{im} \quad (3.2)$$

And Index of each mode can be expressed as (first order):

$$n = \frac{\lambda}{2\Lambda} \quad (3.3)$$

Where λ can relate to eigenfrequency as

$$\lambda = \frac{c}{n_{real} + i^* n_{im}} \quad (3.4)$$

So substituting the wavelength into the equation of refractive index we will achieve the equation, from which it is possible to extract n_{eff} and k_{eef} values.

$$\mathrm{n} = \frac{1}{2\Lambda}\frac{\mathrm{c}\nu_{\mathrm{real}}}{\nu_{\mathrm{real}}^2+\nu_{\mathrm{im}}^2} - \mathrm{i}\frac{1}{2\Lambda}\frac{\mathrm{c}\nu_{\mathrm{im}}}{\nu_{\mathrm{real}}^2+\nu_{\mathrm{im}}^2} = \mathrm{n}_{\mathrm{eff}} - \mathrm{ik}_{\mathrm{eff}} \quad (3.5)$$

The coupling factor κ is deduced from the real part of the complex pulsations of the eigenmodes using optical gap (stopband $\Delta\omega$) concept from coupled mode theory [5].

$$k = \frac{\Delta w}{2c} * n_{eff} \quad (3.6)$$

Using the relation between pulsation and frequency, we can estimate κ in following way:

$$k = \frac{\Delta v}{c} * n_{eff} \quad (3.7)$$

where Δv is Frequency difference between the 2 eigenmodes.

The optical losses are deduced from the imaginary part of the refractive index according to the relationship:

$$\alpha = 4\pi \frac{k_{eff}}{\lambda} \quad (3.8)$$

Confinement factor shows how good laser mode is confined in the active zone and defined as the ratio of electric field in the active region at the wavelength of interest total the total electric field in the total waveguide:

$$\Gamma = \left(\frac{\int_{active\ zone} |E_z|^2 dz}{\int_{total} |E_z|^2 dz}\right) \quad (3.9)$$

The results on losses and confinement factor estimation makes it possible to calculate a figure of merit (χ) defined as :

$$\chi = \frac{\Gamma}{\alpha} \quad (3.10)$$

And we are interested in the biggest value of figure of merit.

The first simulations results show the influence on different depth of grating's etching and different thicknesses of upper cladding on the optical modes of a DFB laser. We had to find right parameters for our device to ensure confinement factor of more than 0.7 [7] and the compromise between losses and coupling factor must be achieved. It is Important to consider that the coupling factor κL (L-length of laser) is wanted to stay above 1 to provide sufficient coupling and efficient DFB effect [8].

We started with the estimation of thickness of upper cladding. On Figure 3.3 we present results of the simulation for losses and coupling factor. These simulations maintain a consistent etching

depth of 0.43 µm while systematically adjusting the thickness of the upper cladding layer, ranging from 0.1 µm to 0.9 µm in 0.1 µm increments. The fixed depth of etching value first was chosen in order to have low form factor, assuring grating to have define straight walls and rectangular profile.

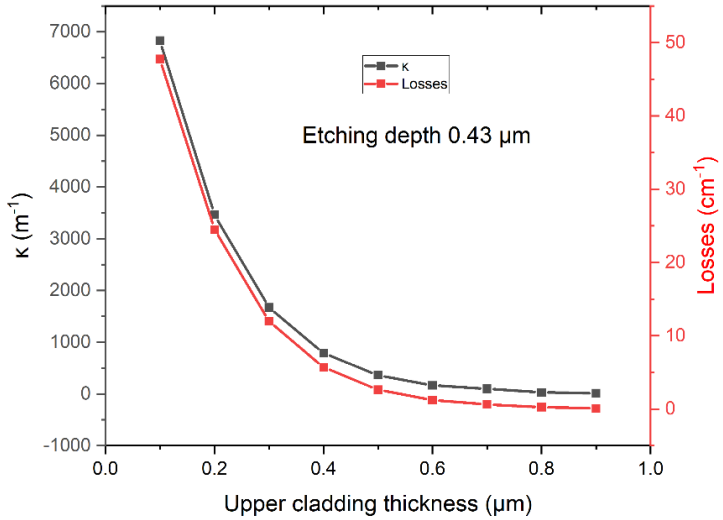


Figure 3.3. Coupling factor and losses versus upper cladding thicknesses with fixed depth of etching of 0.43 µm

It's evident from the data that both losses and the coupling factor exhibit a declining trend as the thickness of the upper cladding layer increases. This observation aligns with logical expectations, as bringing the grating closer to the active zone significantly enhances the coupling efficiency between the mode and the grating. Conversely, thinner upper cladding layers contribute to higher losses. This is primarily due to the increased likelihood of mode leakage out of the cladding and the proximity of the top contact metal, which results in additional absorption and further elevates losses. These results clearly indicate that the optimal choice for the upper cladding thickness falls within the range of 0.4 µm to 0.5 µm, with a preference for the latter. This selection strikes a delicate balance, ensuring that the laser diode achieves efficient coupling while minimizing

losses. It represents a practical and efficient configuration that enhances the overall performance and effectiveness of the device.

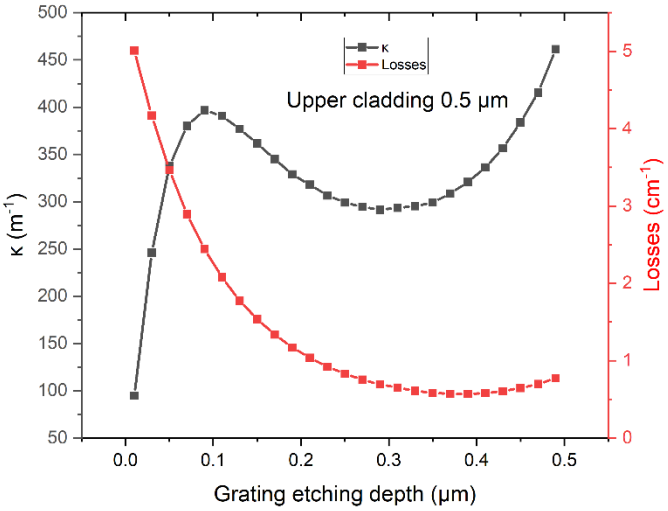


Figure 3.4. Coupling factor and losses versus etching depth for a grating with fixed upper cladding thickness of 0.5 µm

When the best value for the thickness of upper cladding got set, evaluation of the best grating etching depth for this value was performed, considering losses and coupling factor. Figure 3.4 shows plot of losses and κ against the depth of etching with fixed thickness of upper cladding (0.5 µm). It is clear that the best depth of etching should be between 0.4 µm and 0.5 µm (where lowest losses and highest κ are presented at the same range), which values are similar to initial guess assessment of value due to form factor.

In order to corroborate the choice of etching depth, an assessment of the figure of merit was conducted across varying depths of etching, and the outcomes are depicted in Figure 3.5. It is evident from the results that the most substantial figure of merit values are achieved with deeper etching depths, particularly in the range of approximately 0.4 to 0.43 µm.

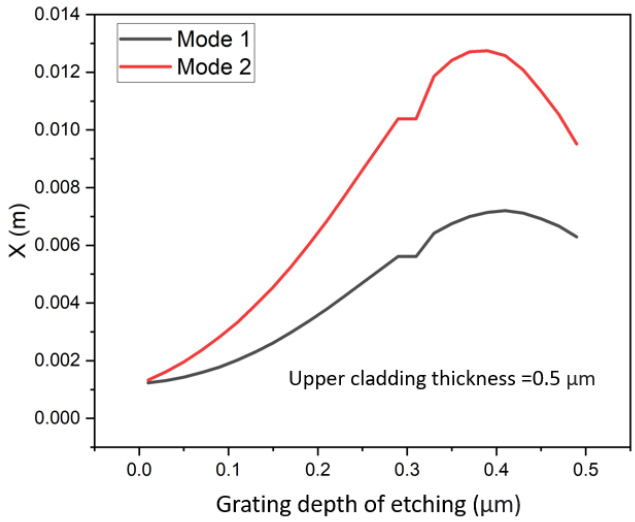


Figure 3.5. Plot of figure of merit against depth of etching

The figure of merit serves as a critical parameter in evaluating the overall performance and efficiency of the laser diode. It takes into account such factors as losses and coupling. The higher figure of merit values observed in the context of deeper etching depths underscores the efficacy and desirability of this specific configuration.This finding reinforces the selection of an etching depth around 0.4-0.43 µm as the optimal choice, as it not only facilitates superior figure of merit values but also aligns with the overall goal of optimizing the laser diode's performance and functionality.

Confinement factor was also estimated for different thickness of the upper cladding (with fixed depth of etching 0.43 (as mentioned before)) and for different grating etching depths (fixing thickness of upper cladding on optimal value 0.5 µm) , results are presented on the Figure 3.6 and Figure 3.7 respectively.. For all thicknesses of upper cladding confinement factor was above the expected value and it didn't change dramatically within studied range, as well as for optimal depth of etching the confinement factor stood above 0.7.

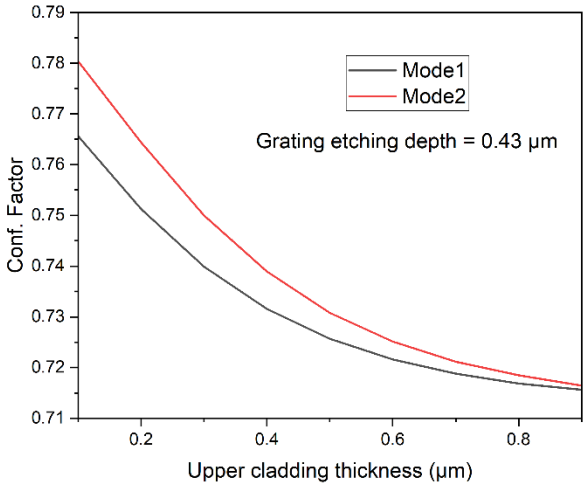


Figure 3.6. Simulation results on confinement factor against different thickness of upper cladding with the fixed depth of etching of 0.43 μm

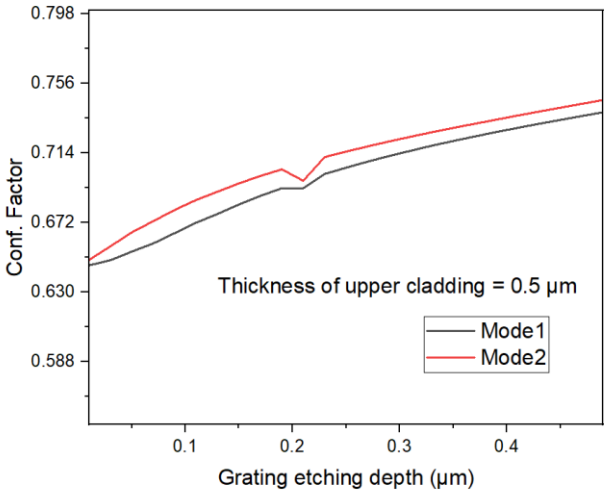


Figure 3.7. Simulation results on confinement factor against different depth of etching for upper cladding of 0.5 μm thick

3.1.2. Simulation of precision in Mesa's etching, establishing the permissible margin of error within the technological process.

The objective was to investigate how the precision of the technological process would impact both the single-mode operation of the device and the confinement factor.

Initially, a 2D model of the structure was developed, and one can observe an image of it in Figure 3.8. A crucial variable parameter was identified as the remaining part of the upper cladding after the Mesa's etching process, which is precisely depicted in Figure 3.8 in accordance with the laser's structure. Simulation experiments were conducted to assess the laser's ability to operate in a single mode operation, going with remaining part of the upper cladding down to 0.05 μm instead of wanted 0.2 μm (which is experimentally established value in Nanomir group to achieve single mode operation and needed beam shape) and these results are particularly revealing. It appears that the acceptable margin of error in the fabrication process can be as large as 0.1 μm. This means that even if the initial target for the remaining part of the upper cladding was set at 0.2 μm and it was ultimately achieved at 0.1 μm, the device can still maintain single-mode operation with confidence. Across all tested thicknesses for the remaining part of the upper cladding, the confinement factor consistently exceeded expectations (was over 0.7). This trend held true even when considering the previously determined optimal thickness of the upper cladding at 0.5 μm.

These findings underscore the robustness of the laser diode's design and fabrication process. They offer valuable insights into the tolerance for variations in the technological process, providing reassurance that even with some level of error, the laser can reliably achieve single-mode operation and maintain desired performance metrics.

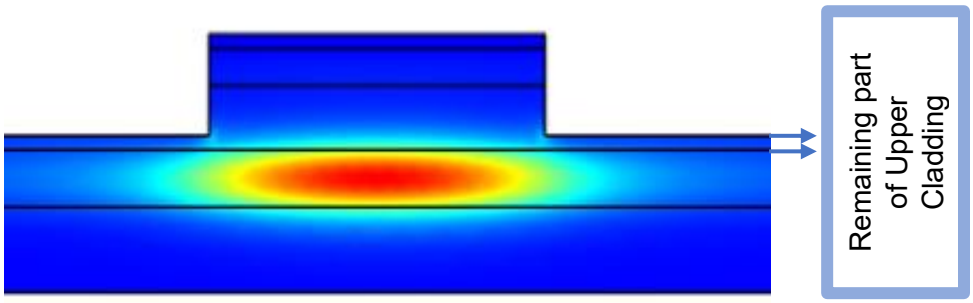


Figure 3.8. Distribution of the electrical field in 2D structure of laser diode with etched mesa

Conclusion.

The final design for the GaSb-based DFB laser diodes with grating on the top of the laser ridge was estimated to have thickness of upper cladding 0.5 µm, depth of grating etch in the range 0.4 – 0.43 µm. It was also confirmed thar error of mesa etching within 0.1 µm wouldn't affect single mode operation or confinement factor.

3.2.Fabrication of novel laser chips in clean room

3.2.1. Fabrication techniques

3.2.1.1.Photolithography

Photolithography is a patterning process in which a photosensitive polymer is selectively exposed to light through a designed chromium mask (having wanted pattern on it) [13], leaving hidden pattern in the polymer that can then be created on the substrate after being put in suitable chemical developer. Name of the used photosensitive material is photoresist, which is based on an organic solution with a photosensitive component. The whole process normally represents in four main steps: first, the deposition of a thin layer of photoresist on the wafer by spin-coating; baking on the hot plate; third, the photomask is brought close to the coated sample and exposed

to UV light; finally, the sample is dipped into a solution to develop the pattern. Resist can have different polarity, which is very important to take in consideration during the design of mask and the process itself. There are two types of photoresists: positive and negative. The main difference is that exposed to UV light resist getting dissolved during development or opposite way around. A positive resist is initially insoluble in developer, but during the light exposure the photosensitive component changes its chemical properties and becomes soluble. Therefore, when using a positive photoresist, the unexposed areas remain on the sample as shown on Fig 2. On

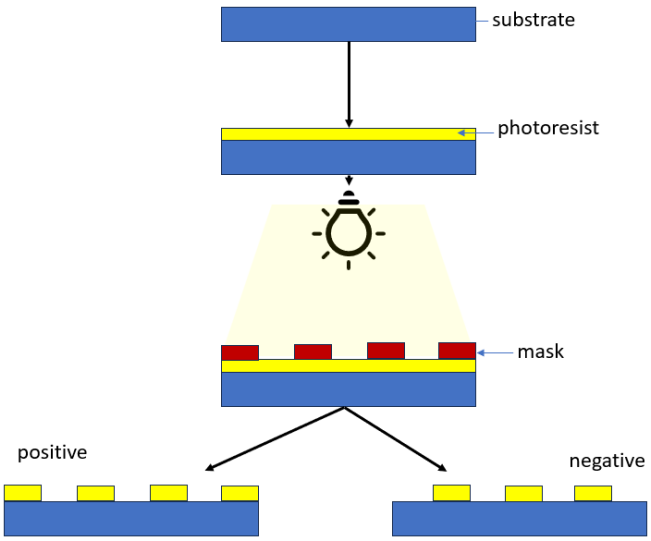


Figure 3.9. Representation of the profiles for photolithography negative and positive polarities of resists

other hand, negative resist become insoluble when exposed to UV light. Hence, when using a negative photoresist, the exposed areas remain on the sample (Fig 3.9). There are some additional steps during the lithography process which might take place. Soft bake, hard bake, or additional light exposure, depending on the requirements of the photoresist and the process itself. Soft bake is normally done before exposure to evaporate part of the solvent of the photoresist. Hard bake is performed after the exposure for a negative resist in order to complete the crosslinking reaction. The resist thickness can be varied by the spin-coating parameters and the

gap by using different contact modes (soft contact (SC), hard contact (HC) or vacuum contact (VC)). Each contact mode pushes the photomask against the resist with different pressure, from low to high pressure, respectively and from lower resolution (large gap) to higher resolution (small gap).

3.2.1.2.E-beam lithography

Electron beam lithography is a direct writing technique that uses an accelerated beam of electrons to create patterns with resolution of sub-10 nm (number depends on apparatus) [14], on substrates that have been coated with an electron beam sensitive resist. Exposure to the electron beam changes the solving ability of the resist, enabling selective removal of either the exposed or non-exposed regions of the resist by immersing it in a developer. Depends on polarity of the used resist (negative or positive), the parts of pattern which have been under exposure or become more soluble (as the electrons induce local chain scission) or more resistant to developer. The resolution of e-beam lithography is determined by the scattering of primary and secondary electrons in the resist layer and the substrate. When electrons hit resist with high energy, they scatter forward. Despite the very small beam spot size (less than 0.5 nm) focused on top of the resist surface, the exposed area in resist becomes much larger as scattering broadens the beam inside the resist. Some electrons are bounced off from the substrate and backscatter (large angle scattering) with micrometre range. And then if the neighbouring features are tightly spaced, the exposure dose should account for the backscattered electrons (that is named proximity effect). Exposure dose, precise focus on the substrate (including creation of quantum dots for the focusing purposes), angle correction for sample position and right-field alignment – all of it needs to be optimised with high precision before starting the process. For this technique physical

mask is not needed (mask is programmed in specific software), what allows more flexibility for the fabrication itself.

3.2.1.3.Inductively coupled plasma (ICP)

Dry etching is very popular technique for nanofabrication, as it shows very high precision, provides anisotropic profiles and allows good repeatability and has good control over the etch depth. Another advantage is that it prevents user from interacting with dangerous acids (as in wet etching). ICP is based on plasma etching, where the accelerated molecules bombing the sample surface resulting in physical etching. Chemical etching also takes place to some extent during the process because the accelerated molecules are chemical species that also reacts with the sample material. By adjusting the etching parameters, it is possible to control which etching mechanism will dominate. The etching parameters which can be adjusted are gas composition and flow, chamber pressure, temperature, RF and ICP powers. It is very important to know the precise etching rate for the structure of the chosen gas recipe in order to adjust the etching time. The sample is fixed to the holder with thermal oil for a good thermal contact. For GaSb-based samples is good to process with chlorine etching [15].

3.2.1.4.Deposition of metal by evaporation technique

Deposition by evaporation method is widely used for the deposition of thin layers of materials. The main idea of the method is that the heated source material is evaporated in a vacuum, which allows vapor particles to travel directly to the substrate, where they condense back to a solid state. In high vacuum (with a long mean free path), evaporated particles can travel directly to the deposition target without colliding with the background gas. Evaporated materials deposit nonuniformly if the substrate has a rough surface, because the evaporated material arrives to the

substrate mostly from a single direction, protruding features block the evaporated material from some areas (what is good for metal lift-off).

3.2.1.5.Deposition of metal by sputtering technique

Sputtering is also a thin film deposition method, based on physical deposition. A solid target with the atoms of the material to be deposited is bombarded by an ionized inert gas (usually argon). The atoms are sputtered from the target, and they deposit after on the substrate. An important advantage of sputter deposition is that even materials with very high melting points are easily sputtered while evaporation of these materials in a resistance evaporator is problematic or impossible. Sputtered films typically also stick better on the substrate than evaporated films. But this technique makes the lift-off process impossible due to the , characteristic of sputtering, which makes a full shadow impossible. It is not possible in this technique to fully restrict where the atoms go, which can also lead to contamination problems.

3.2.2 Wafer's growth

Wafers for all samples were grown using molecular beam epitaxy (MBE), which is very well known for the growth of III-V semiconductor materials. As have been mentioned before, this technique implies the growth of the material on a heated crystalline substrate by the deposition of molecules and atoms of the required species. Two generations of wafers were grown by solid-source MBE on a Te-doped, n-type, (001) ± 0.1° oriented GaSb substrate in a VARIAN GENII reactor equipped with an Sb- valved cracker cell providing Sb species. Growth rates were inferred from flux measurements carefully calibrated by reflection high-energy electron diffraction (RHEED). Growth temperature was measured with an optical pyrometer calibrated using (1x3) to

(2x5) surface reconstruction transitions observed on the GaSb surface. Tellurium (Te) and Beryllium (Be) were used as the n-type and p-type dopants respectively. All layer thicknesses are illustrated on Fig. 5. A 1.3 µm-thick layer of $Al_{0.9}GaAsSb_{0.92}$ serves as the bottom cladding (n-cladding) followed by two $Al_{0.25}GaAsSb_{0.98}$ waveguides on the sides (each 380 nm thick). In between the waveguides, there are 2 $GaIn_{0.33}AsSb$ quantum wells (QW) (each 10 nm thick) separated by the 25 nm thick $Al_{0.25}GaAsSb_{0.98}$ barrier layer. The upper cladding (p-cladding) consists of $Al_{0.9}GaAsSb_{0.92}$ and has a thickness of 0.5 µm. This is followed by a grading layer of 0.1 µm and, finally, 0.2 µm of p doped GaSb were epitaxied as a top contact layer.

One can see the schematic representation of all layers for both generations on the Fig 3.10. List of total number of wafers used for the laser processing is presented in Table 3.2.

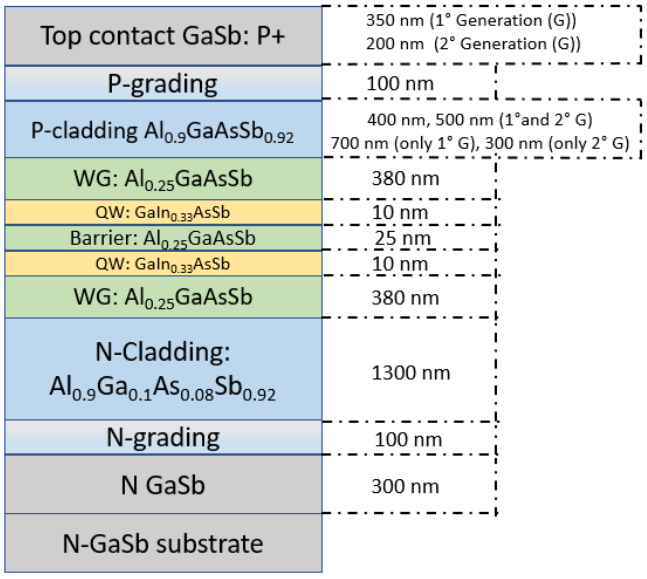


Figure 3.10. Schematic representation of laser's structure for both generations

Name of wafer	Thickness of upper cladding, µm	Thickness of top contact layer, µm	Generation
V3265	0.4	0.35	1
V3267	0.5	0.35	1
V3268	0.7	0.35	1
V3343	0.3	0.2	2
V3344	0.4	0.2	2
V3346	0.5	0.2	2

Table 3.2. List of wafers grown for laser processing

3.2.3. Fabrication of Fabry-Perot laser diodes

Fabrication of Fabry-Perot laser diodes prior to DFB fabrication is essential for the confirming the viability of estimated through simulations small upper cladding thickness and to be able to know the emitted wavelength by the presented wafers (for adjustment of grating period).

During the fabrication of the Fabry-Perot devices following main steps are necessary: determine the mesa and create an insulation layer, make deoxidation of the structure and assure bottom and top contact metallisation, lift-off for the top contact (to electrically separate the lasers), cleaving and mounting. Thinning of the substrate down to 150 nm is also mandatory for better heat dissipation. We processed one samples from each wafer from both grown generations.

The process is started with the cleaning of the samples from any organic dust or other species using acetone/ethanol/isopropanol baths. Sample should be dehydrated by annealing at 110°C for 1 min. After been assured that the surface is ready for fabrication – mesa determination should be started.

To determine the Mesa (Fig. 3.11 (a)) the photolithography technique with physical Cr masks was used. We used a mask having mesas with widths of 8 µm, 10 µm, 12 µm, 2 µm and 100 µm.

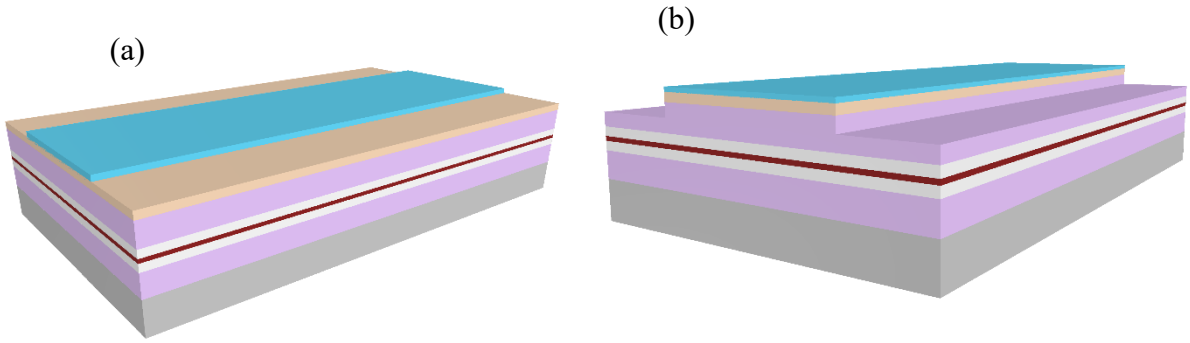


Figure 3.11. Representation of defined mesa by the resist (a) and of mesa after etching (b); blue colour represents resist, beige – top contact layer, violet – bottom and upper claddings, white -waveguides, red -quantum wells, grey -substrate;

This technique is based on the exposition of a photo-sensible polymer (a photoresist) deposited on the sample. Positive photoresist Az1518 was used according to the polarity of the mask. Parameters of the spin coating were as follows to bobtain necessary thickness of the the resist: RPM = 4000, Ramp = 2 and Time = 30 s. When spin coating was done, it was needed to

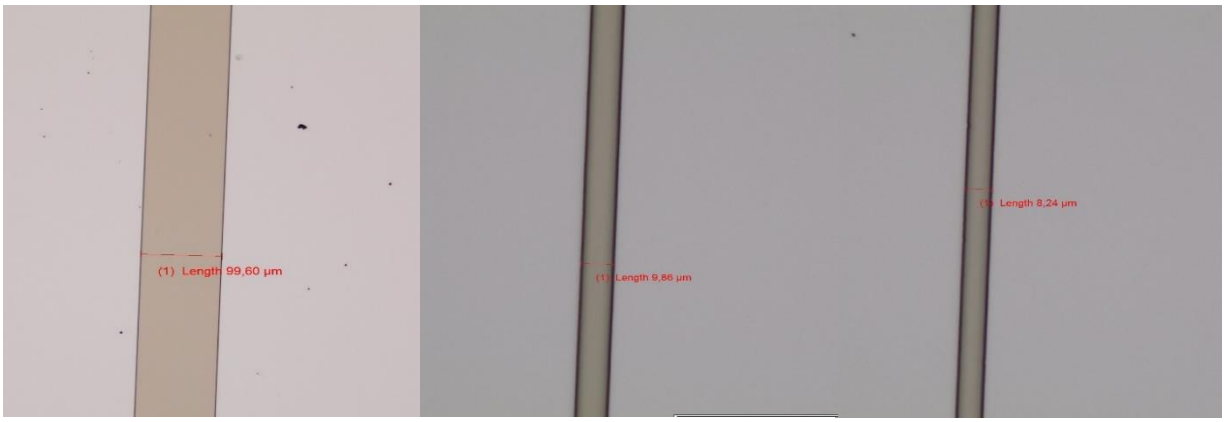


Figure 3.12. Photo from optical microscope of mesas with widths of 100 µm, 10 µm, 8 µm

perform soft bake at 110°C for 1 minute to evaporate the solvent from the resist. Exposure was made by MJB4 machine, and the time of exposure was 23s during 1 cycle. Mask was aligned according to cleaved edges. After exposure, we proceeded with development of the sample in bath of MIF319 developer for 30 s. For some samples development time was affected by the change

of humidity in the room, as viscosity and solubility of the resist can be influenced by it, increasing the moisture content of the resist, altering its physical characteristics. This affects how quickly the resist dissolves or reacts during development. Check of the developed mesa width was essential and was done by the optical microscope. Photos from optical microscope of some of the mesas are presented on Fig. 3.12.

After determination of the mesa, dry etching is used to be able to actually create the pattern, where the resist played role of the etching mask. (Fig 3.11 (b)) ICP Oxford with recipe of $BCl_3/Cl_2/Ar$



Figure 3.13. Photo from optical microscope of the mesas with insulation layer

plasma was chosen for etching given structure. Etching rate of resist (140 nm/min) and of structure (350 nm/min) were determined beforehand leading to different time of etching for each sample (as each sample had different thickness of upper cladding and some of them different thickness of top contact layers). After that the removal of resist is achieved by keeping the sample in acetone bath for 45 min. When resist was still there after the bath – oxygen plasma was applied for 2-3 minutes.

To avoid oxidation of the layers, it's very important to proceed with the fabrication of the insulation layer in the same day when etching was done. We used again positive resist Az1518 as insulation layers in all fabricated Fabry-Perot devices. The pattern was achieved by using

different mask designed for photolithography. All parameters for photolithography remained the same as in mesa determination. After development insulation layer was undergoing baking to harden resist. Photo example of mesa with insulation layer is presented on Fig. 3.13.

Next important step is determination of metal contacts. Firstly, top contact layer is created, but it is very important to achieve electrical separation of each laser on the laser bar, that's why

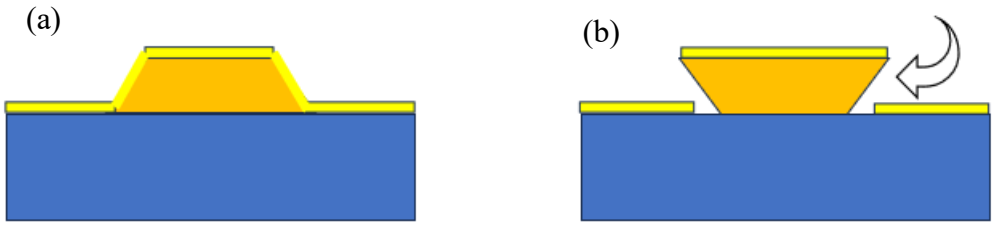


Figure 3.14. Representation of positive (a) and negative (b) profiles of resist for lift off purpose.

certain width of metal strip should be lifted in between the mesas. In order to determine the lifting pattern with negative resist Az2070 – photolithography needs to be performed. The negative resist allows to get a necessary pattern for the lift off, as negative resist after development would assure a negative slope of the pattern and it would give the better access for acetone to remove unwanted parts, while the positive resist would have a positive slope (Fig.3.14).

Spin coating parameters and baking parameters were the same as for the positive resist Az1518, but the exposure time was 6 s for 1 cycle and after the exposure the baking for 1 min at 110^{o}C was performed (what is not needed for photolithography with positive resists). Developer AZ726MIF was used for 1 min 30 sec to create the pattern.

After the photolithography, the deoxidation is performed, we used solution of H_2O/HCL in proportions of 4/1, soaking samples in the bath with such solution for 30 s. To remove the remaining acid– all the samples were carefully rinsed in deionized water.

After deoxidation samples were ready for deposition of top contact layer, we deposited layers of Au/Ti, having thickness of 400/20 nm, using evaporation technique. Evaporation technique was chosen as metal would be deposited vertically giving better access for lift off solution to resist. The lift off was done in acetone bath and additional pressure on the surface was introduced through the syringe, putting the flow of acetone all over the sample what would allow the resist to dissolve, and resist would lift with himself the unwanted parts of metal.

To achieve better conductivity of the device, thinning of the substrate is mandatory. Originally thickness of substrate is about 600 μm – it needs to be thinned down to 120-150 μm. We used mechanically polishing with abrasive paper P240 reaching speed of rotation about 120 rpm. The sample is sticked to metal holder by crystal bond, top contact facing the holder. It is crucial to assure the homogenous thinning through all the sample.

When satisfactory thickness of the substrate is achieved, bottom contact is deposited. We used sputtering technique for deposition of Pd/AuGeNi (5/200 nm) layers. For better integration of metals into the substrate – annealing was performed putting sample on the hot plate heated up to 185^{o}C.

After fabrication of bottom contact layer – sample is ready for cleaving. Cleaving is a very important process and requires a lot of precision, as at this step the facet quality will be established what can after dramatically affect the laser performance (defining the reflectivity of the cavity). Thanks to the lift off, it is possible to separate lasers electronically and we could

directly cleave laser bars with several lasers on it. From each sample we cleaved laser bars of 1 mm length.

Mounting of the laser bars was done on the copper base using indium as a bonding material. All lasers were mounted epi-side up. The final picture of the device can be seen on the Fig. 3.15.



Figure 3.15. Photo of the mounted laser bar

3.2.4 Fabrication of DFB laser diodes with the grating on the top of the laser ridge (Montpellier)

Described below DFB laser diodes were based on the wafer from Generation 2 (Fig. 3.14) with thickness of upper cladding of 0.5 µm (V3346). Processing of DFB laser diodes starts in the same way as previous fabrication - with the clearance of the sample surface using

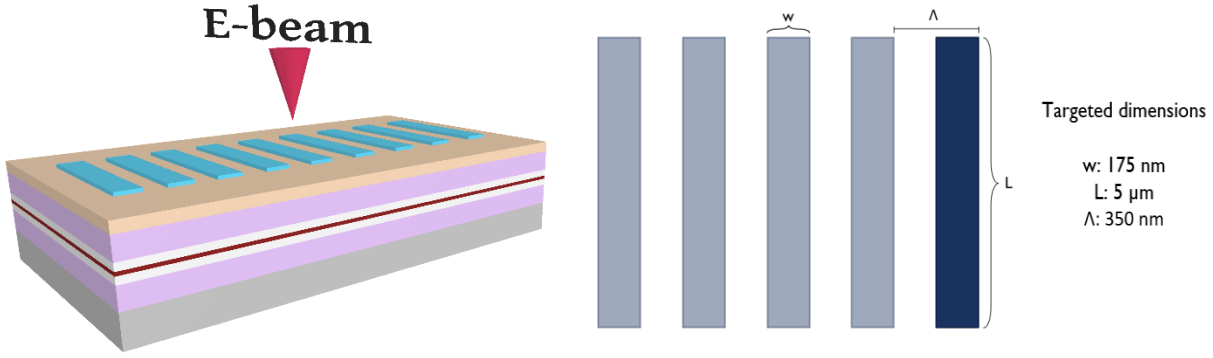


Figure 3.16. Representation of the grating pattern on the sample

acetone/ethanol/isopropanol baths. But unlikely in Fabry-Perot fabrication – the current processing starts with the determination of the grating.

The determination of the grating structure was accomplished through the utilization of e-beam lithography, employing equipment provided by company RAITH. Our objective was to create a grating with a period (Λ) of 350 nm and a Duty Cycle of 50%, as illustrated in Figure 3.16. All the symbols for grating dimensions to consider are showed on Figure 3.16.

3.2.4.1 Tests for grating E-beam exposure and grating etching

Numerous experiments were conducted to optimize exposure dose and development time for the current resist material. All mentioned tests bellow were done on the testing standard GaSb wafer for laser diodes, to be able to evaluate the bets parameters for exposure on real samples for future DFBs. Exposure doses were varied within the range of 50% to 190% of the nominal dose, with increments of 10%. For each exposure dose setting, the development time was also adjusted, ranging from 15 seconds to 36 seconds, with increments of 2 seconds. The test specifications

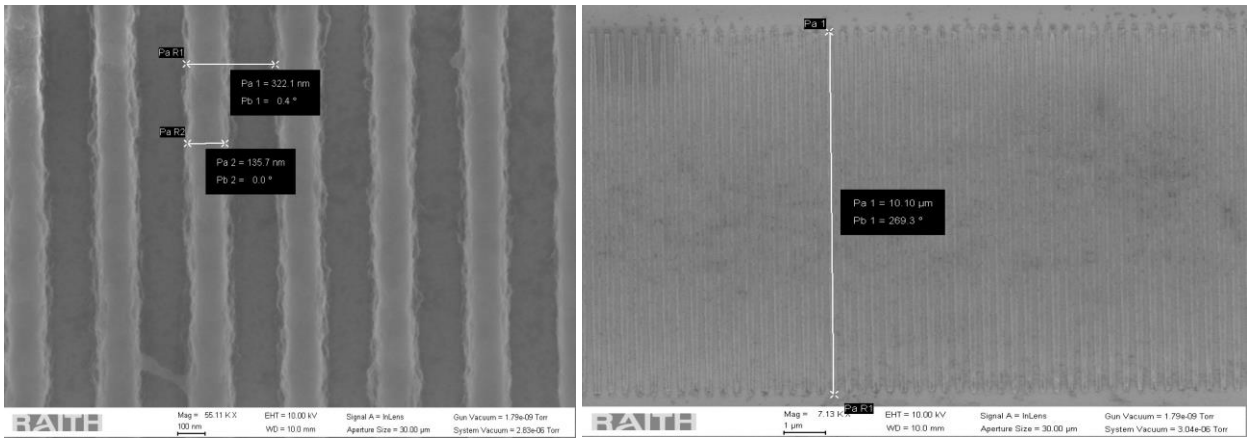


Figure 3.17. Photo from E-beam of the exposed grating (Dose of 120% out of nominal)

included a target line width (L) of 10 µm, a grating period of 320 nm, and a ridge width (w) of 160 nm. These rigorous tests and adjustments were undertaken to ensure the precise fabrication of the desired grating structure. On Fig. 3.17, e-beam pictures of exposed grating under the

optimal chosen dose (120%) is shown after development. The progression of the grating length (L) with development time for each dose is represented on the graph on Fig. 3.18.

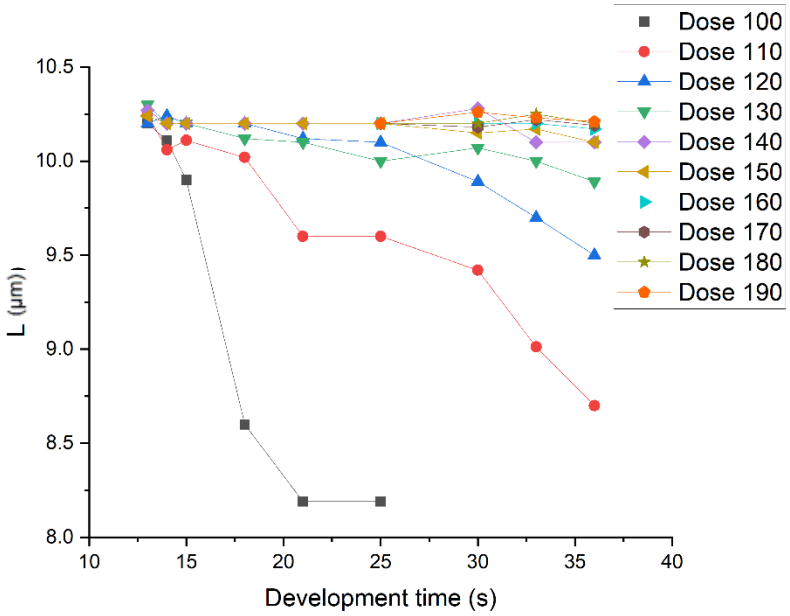


Figure 3.18. Graph represents the development of the grating length for different doses of exposure

In order to achieve less spiky edges of the grating stripes and duty cycle of 50 % - it was decided to work on 120% of nominal dose (nominal dose is 13 µC/cm²). The precise focus on the sample must be performed at the first place following with angle correction and right-field alignment. After the exposure sample should be baked for 1 minute on the hot plate under 110°C. The very careful development of the sample should be performed, taking into the consideration fluctuations of the humidity of the room at the moment. Photoresists are often sensitive to moisture, and excessive humidity can impact the chemical solubility of the exposed and unexposed regions of the resist. This can either accelerate or decelerate the dissolution of the unexposed regions during development. Change in humidity can also affect the temperature of the room leading to variations

in viscosity of solution which affect the rate at which the developer dissolves the photoresist. Moreover, the precision of the time is very important as experimentally it was confirmed that even 2 s error can lead to dramatical changes in the pattern. The total development time of the sample after all the tests was 36 s.

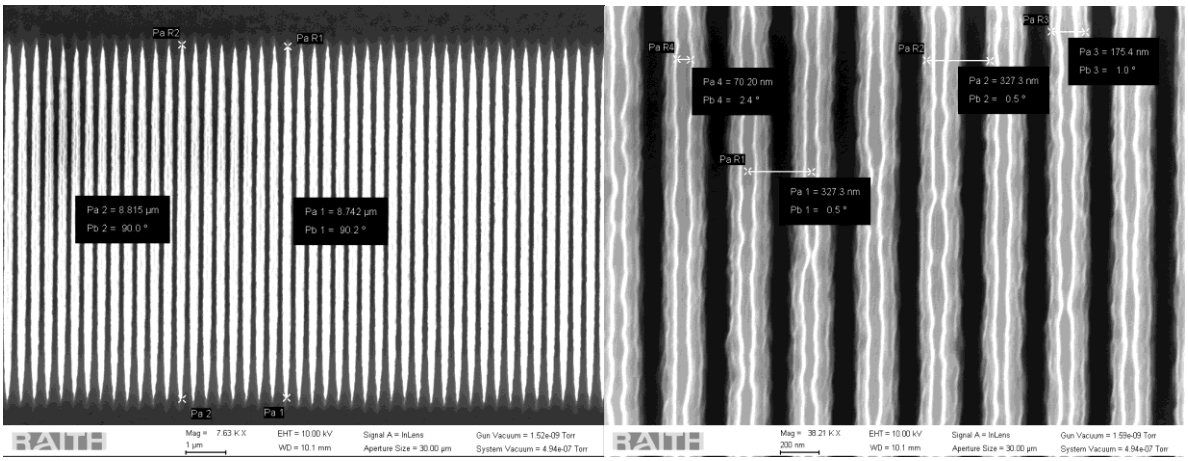


Figure 3.19. E-beam photo of the test etched grating

Next step is the etching of the grating which was performed in ICP Oxford using $BCl_3/Cl_2/Ar$ plasma (same as for Fabry-Perot lasers fabrication). The etching rate have been calculated independently for the grating etch, because of the very small grating period it was hard for plasma to reach gaps between the resist and etch the structure in wanted spaces, so several tested samples has been processed. Another difficulty was that we needed to have deep etch on our structure (500 nm, while top contact +grading +upper cladding layers all together are 800 nm). It meant that we had to assure the sufficient thickness of the resist after the development of the grating pattern. Photo of the test etched grating (with period of 320 nm, grating length of 10 µm) is shown on Fig. 3.19.

First step was the determination of the grating by E-beam lithography. Important to keep in mind that future mesa width would be 5 µm and grating should not exceed the boundaries of the mesa.

The process commenced with the spin-off of the negative resist Az2020, carried out under specific conditions: a spin rate of 6000 rpm with a ramp duration of 3 and a spin time of 30 seconds. Subsequently, baking was conducted at a temperature of 110°C for a duration of 1 minute and 30 seconds. Tests, presented before, estimated the exposure dosage of 120% of nominal dose (nominal dose is 13 $\mu C/cm^2$). The developing time was 36 s. Determination of mesa was followed by dry etching in ICP Oxford using BCl_3/Cl_2/Ar plasma. Depth of etching was 0.45 μm.

After successful etching, when the grating was fully determined, it was crucial to assure that resist would be gone from all parts of the sample (otherwise if even small amounts remained – burn of the resist hence burn of the entire device was observed during the characterisation). This part was extremely challenging as we didn't find acetone baths or remover PG to be very effective. The only solution was to use oxygen plasma, which we proved to be effective during the Fabry-Perot fabrication, facing the problem of oxidation of the grating walls (grating was etched into the upper cladding layer with hight content of Aluminium of 90 %). It was decided to introduce additional deoxidations using H_2O/HCL 4/1 solution between the main fabrication steps instead of performing it only before the metallisation (top and bottom). Additional deoxidation was done after removal of all the resist by oxygen plasma. Storing samples in a vacuum environment when they were not actively being processed, and consistently striving to reach a point where the walls would be uniformly coated with resist by the end of the day, played a vital role in the fabrication process.

Mesa was determined by the photolithography using negative resist Az2020 but with different spin off configurations (4000 rpm/ ramp 2 / 30 sec). Baking was under same conditions as for e-beam lithography. Alignment of the mask during this process is crucial for the device fabrication as grating is already etched and it should not exceed the mesa boarders in order to stay strictly on the top of the ridge by the end of the process. Using the same photolithography machine as for Fabry-Perot process before, the exposure time was 9 sec during 1 cycle. Development of the sample took 45 s. Etching of the Mesa was done by the same technique as mesa etch for Fabry-Perot laser diodes, using $BCl_3/Cl_2/Ar$ plasma and the additional mesa etch was 100 nm. Width of mesa was 5 µm. To remove remaining resist after mesa etch was used the technique described above. Deoxidation step was performed when the resist was out of the surface.

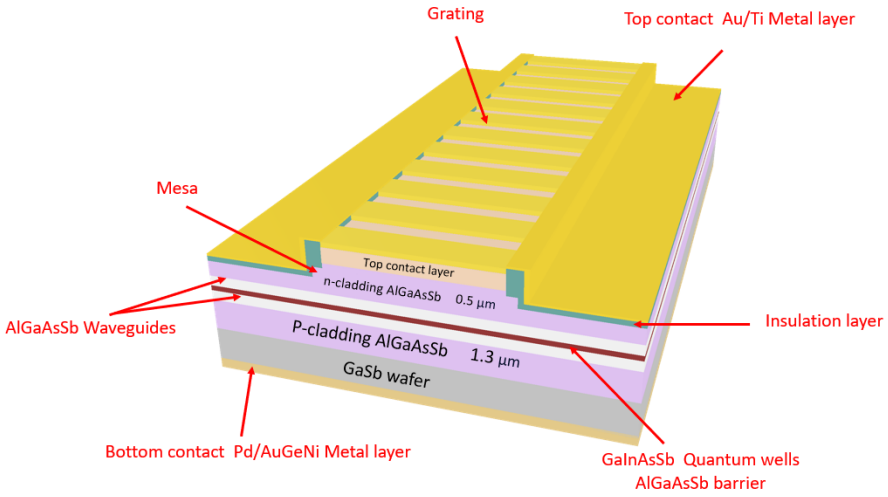


Figure 3.20. 3D image of the final device

As insulation layer we used resist AZ 2020, spin off and photolithography was done with the same parameters as for the mesa determination. The opening window was 4 µm. The insulation layer had to go through baking in the oven for 2h under 180°C, to harden the resist.

All the next steps including photolithography for metal lift off, deoxidation, top and bottom metallization, substrate thinning, cleaving and mounting of the samples were done in the exact same way as it was processed for Fabry-Perot samples. Final representation of the device can be seen on Fig. 3.20. Overall flow of the fabrication process with all steps in right order is presented on Fig 3.21.

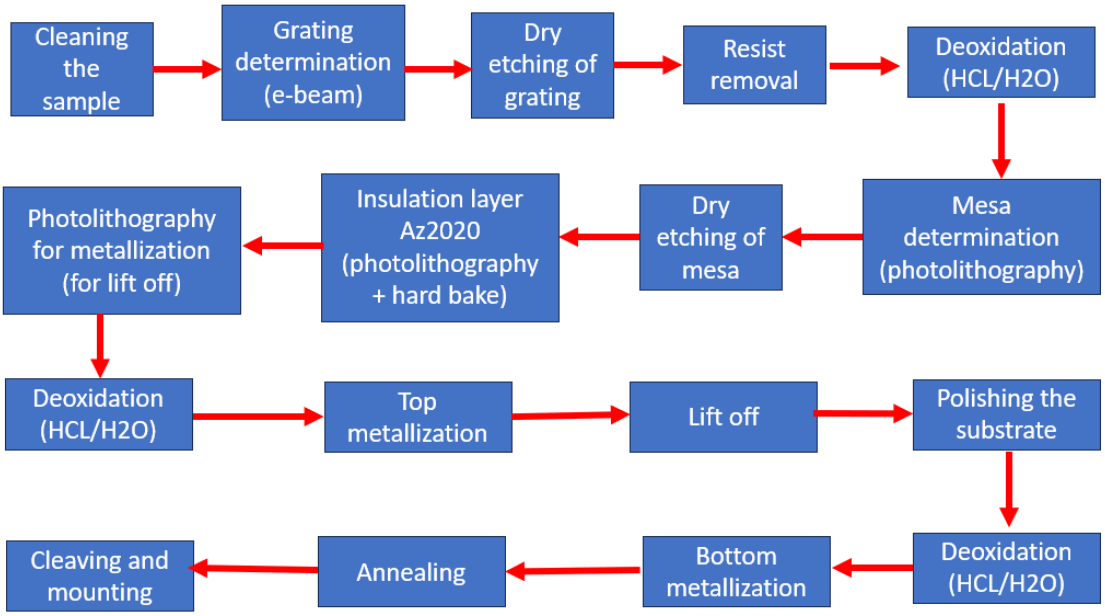


Figure 3.21. Representation of fabrication process for DFB laser diode in Montpellier

3.2.5. Fabrication of DFB laser diodes with grating on the top of the laser ridge (NANOPLUS)

Fabrication process of samples in Nanoplus was slightly different from the one conducted in Montpellier facilities. As Nanoplus is an industrial company – the information on the process itself will be limited. Processing was done on the wafers form Generation 2 mentioned above (growth was done in Montpellier) (Fig. 3.10). Samples with thickness of upper cladding 0.4 μm and 0.5 μm and thickness of top contact layer 0.2 μm were fabricated (wafers V3344, V3346).

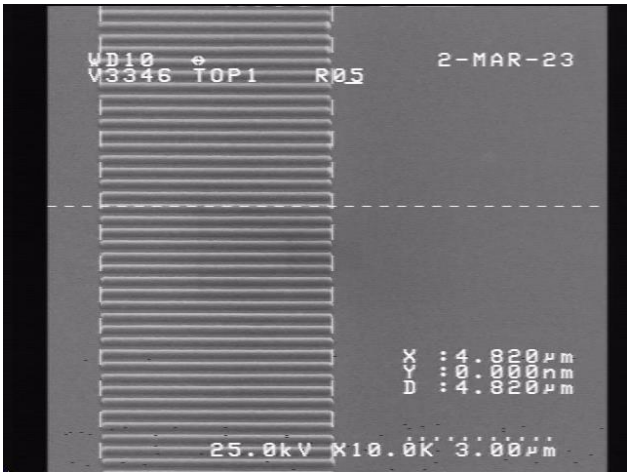


Figure 3.22. Photo of grating pattern after E-beam exposure

The wafer processing typically commenced with the initial step of cleaning the samples using a solution of acetone and isopropanol. Subsequently, the process involved determining the grating

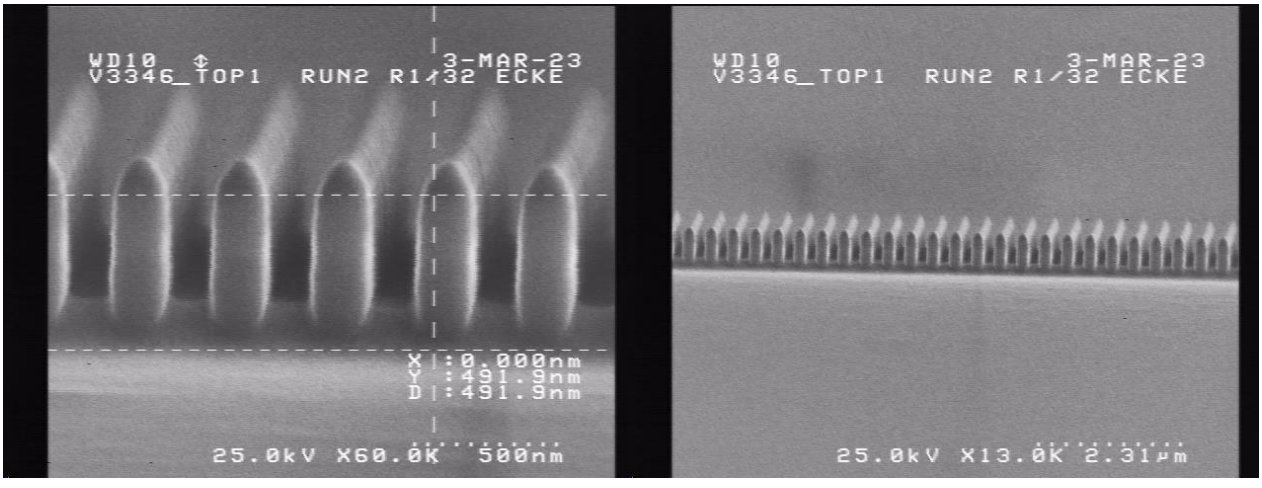


Figure 3.23. Photo of the etched grating.



Figure 3.24. Photo of the etched mesa

structure, which was achieved using PMMA (Polymethyl Methacrylate) resist and E-beam lithography. PMMA was evenly applied to both samples, followed by E-beam exposure at a dosage of 1800 μC/cm². Pattern of gratings with duty cycle of 50% and variations of period of 246 nm, 250 nm, 254 nm and 258 nm were inscribed on samples. Development of PMMA was done in MIBK/Isopropanol solution following proportions of 1/3 during 1 min and 30 s. After the development of the grating – hard mask was evaporated and then it was lifted off, leaving the grating pattern (Fig. 3.22). The grating was etched using dry etching by ICP, depth of etching for grating for a sample with upper cladding of 400 nm was 400 nm and for the sample with thickness of upper cladding of 500 nm – 500 nm. An example of the etched grating is presented on Fig. 3.23.

Mesa determination was done in a similar way by using PMMA as a resist and E-beam lithography for the exposure. The same developing conditions were applied. Width of mesa was 5 μm. After the dry etch the height of Mesa for both samples was 100 nm (Fig. 3.24).

Etching mask was dissolved in water bath. Deoxidation in HCL/H_2O solution was performed. For these samples SiN was used as the first round of passivation and SiO_2 as a second round. The

opened contact window was 4 um width. As p-contact Ti/Pt/Au layer was used and for n- contact AuGe/Ne/Au layer.

3.2.6 Fabrication of DFB laser diodes with lateral metal grating along the ridge (NANOPLUS)

Finally, to confirm the compatibility of the top grating samples, we decided to compare them with already well established technique on the market for such structures – devices with lateral metal grating along the ridge. So the fabrication was done on the same wafers (Fig. 3.14) as for the top grating samples at Nanoplus (Generation 2, thickness of upper cladding 0.4 μm and 0.5 μm).

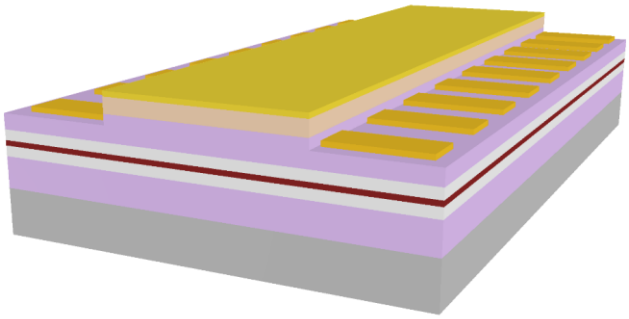


Figure 3.25. Representation of the device's design with the metal grating along the ridge

Fabrication process was similar to the process already established in the company. Picture of the design can be seen on Fig. 3.25).

The process has a lot of similarities with the top grating samples fabricated at Nanoplus. PMMA resist and E-beam lithography were also used both for mesa and grating determination (using same parameters). Main alteration was the order of the steps (mesa etch was before the grating), position of grating and that grating was evaporated but not etched in the structure. Order of steps were as follows:

- Cleaning in acetone/isopropanol baths
- Spreading of PMMA resist
- E-beam exposure for Mesa (3.8 um width)
- Evaporation of hard Mask
- Lift off of Mask (Fig. 3.26)
- Ridge etching (ICP dry etching)
- Passivation SiN
- Spreading of PMMA

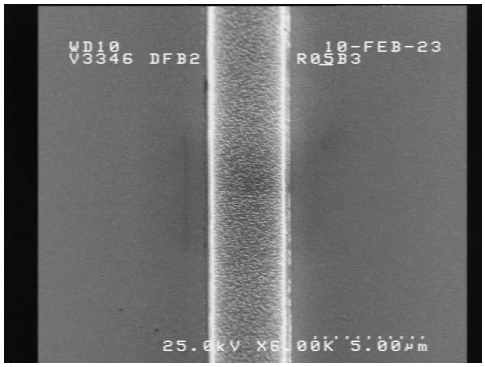


Figure 3.26. Photo of the determined mesa width

- Grating exposure E-beam (periods of grating: 350 nm, 354 nm, 358 nm, 362 nm)
- Evaporation of grating
- Lift off of grating (Fig. 3.27)
- Passivation SiO_2
- Open contact window
- Removing etching mask
- P-contact Ti/Pt/Au
- N -contact AuGe/Ne/Au

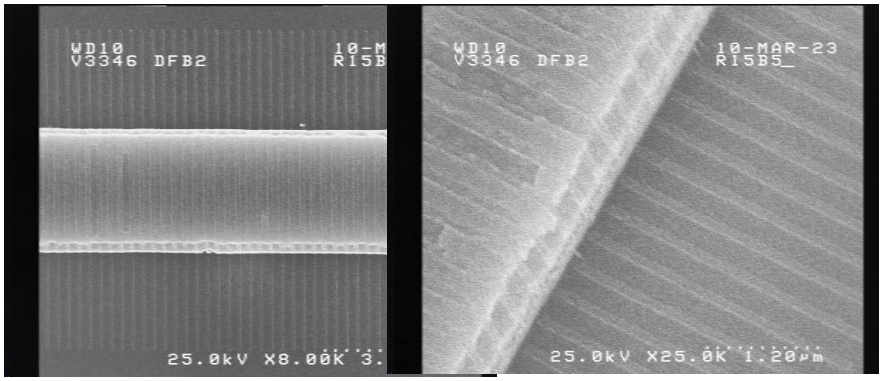


Figure 3.27. Photos of grating along the mesa

Conclusion.

In addition to the successful development of the fabrication process, this chapter represents a significant milestone in the broader context of semiconductor laser technology. The integration of top grating designs into GaSb-based DFB laser diodes opens up new avenues for advanced laser applications, particularly in the mid-infrared spectral range.

The studies conducted here, combining theoretical simulations and practical experimentation, have not only resulted in the creation of a fabrication process but have also deepened our understanding of the intricacies involved in designing and manufacturing cutting-edge laser

devices. Moreover, by demonstrating the compatibility of this new fabrication process with existing techniques for lateral grating samples, we have paved the way for seamless integration into established manufacturing workflows. This achievement promises increased flexibility and scalability in the production of such DFB laser diodes, which can have wide-ranging applications across various industries, including environmental monitoring and spectroscopy.

References

[1] Guekos George. Photonic devices for telecommunications: how to model and measure;. ISBN 3-540-64318-4 (he.: alk. paper) TK5103.G84 1998 621.382-dc21 98-44450

[2] E. D. Palik, "Handbook of Optical Constants and Solids," Academic, Orlando, 1985 Handbook Series on Semiconductor Parameters: Ternary and quaternary III-V compounds

[3] A. Levinshtein, M.,A Rumyantsev, S.L.,A Shur, M., A Scientific, W., Handbook Series on Semiconductor Parameters: Ternary and quaternary III-V compounds,1999,World Scientific Publishing Company

[4] David Seider; Solving an Eigenvalue Problem in Laser Simulation; Dissertation zur Erlangung des naturwissenschaftlichen Doktorgrades der Bayerischen Julius-Maximilians-Universit¨at Wurzburg;2004

[5] H. Kogelnik Coupled wave theory for thick hologram gratings Bell System Technical Journal 48 (9), p. 2909, 1969

[6] H. Kogelnik and C. V. Shank Stimulated emission in a periodic structure Appl. Phys. Lett. 18, p.497-499, 1971

[7] R. Mostallino, “Development of high-power laser diodes emitting at 975 nm with enhanced wall-plug efficiency and wavelength stabilization for optical pumping of doped fibers and realization of fiber lasers”, Ph.D. dissertation, University of Bordeaux (2018)

[8] S. Forouhar, R. M. Briggs, C. Frez, K. J. Franz, A. Ksendzov, "High-power laterally coupled distributed-feedback GaSb-based diode lasers at 2 μm wavelength", Appl. Phys. Lett. 100, 031107, 1.3678187 (2012)

[9] Niu S, Wei Z, Fang X, Wang D, Wang X, Gao X, Chen R. Brief Review of Epitaxy and Emission Properties of GaSb and Related Semiconductors. *Crystals*. 2017; 7(11):337. https://doi.org/10.3390/cryst7110337

[10] Razeghi, M. (2009). Technology of Quantum Devices. Germany: Springer US., p.28ff.

[11] John Orton, Tom Foxon; Molecular Beam Epitaxy: A Short History ; Oxford University Press, 2015, p.36.

[12] K. Alavi, Molecular Beam Epitaxy, Encyclopedia of Materials: Science and Technology, Elsevier, 2001, P. 5765-5780, https://doi.org/10.1016/B0-08-043152-6/01002-0.

[13] del Barrio, J., Sánchez-Somolinos, C., Light to Shape the Future: From Photolithography to 4D Printing. Advanced Optical Materials 2019, 7, https://doi.org/10.1002/adom.201900598

[14] Reema McMullen, Aditya Mishra, Jason D. Slinker, Straightforward fabrication of sub-10 nm nanogap electrode pairs by electron beam lithography, Precision Engineering, Volume 77, 2022, Pages 275-280, https://doi.org/10.1016/j.precisioneng.2022.06.004

[15] T Maeda, J.W Lee, R.J Shul, J Han, J Hong, E.S Lambers, S.J Pearton, C.R Abernathy, W.S Hobson, Inductively coupled plasma etching of III–V semiconductors in BCl3-based

chemistries: I. GaAs, GaN, GaP, GaSb and AlGaAs, Applied Surface Science, Volume 143, Issues 1–4, 1999, Pages 174-182, https://doi.org/10.1016/S0169-4332(98)00594-7.

Chapter 4. Novel GaSb based DFB laser diodes emitting at 2.4 µm. Experimental results and discussions

4.1. Characterisation of laser diodes

4.1.1. L-I-V characteristics in CW mode

Light-current-Voltage characteristic evaluate electrical and optical operational characteristics of tested devices. Electrical current is applied to laser diode (usually at range of mA) and intensity of the laser beam is measured by photo detector placed on the output of the device and gives the idea of output power of the laser diode per facet. Voltage drops between two contacts of laser diode is measured at the same time. On Figure 4.1 one can see a typical LIV curve, where the threshold current (I_{th}) and turn on voltage (V_o) are indicated.

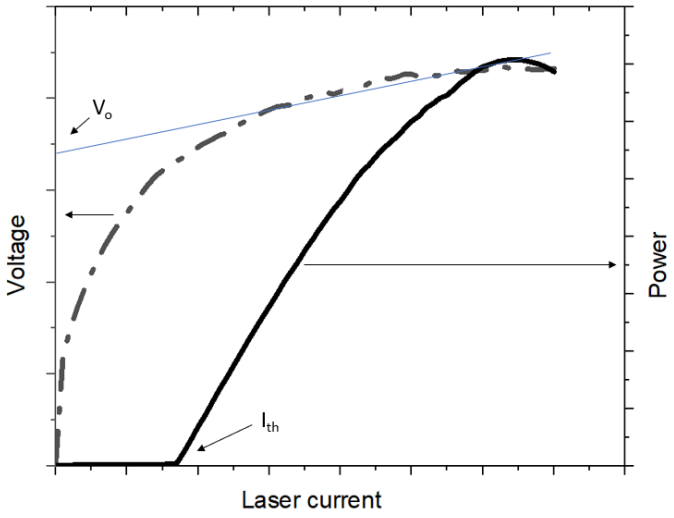


Figure 4.1. Representation of typical LIV curve

4.1.2. Spectrum measurements

Spectrum measurements serve the purpose of determining the emitted wavelength of a laser source and provide insights into whether the source operates in a single or mono mode. During the characterization of samples conducted at the University of Montpellier, the spectrum analysis was carried out using FTIR, or Fourier Transform Infrared Spectroscopy, a widely employed technique. FTIR works by taking advantage of the fact that a laser beam can be split into different paths using an interferometer. The interferometer creates an interference pattern, and this pattern is then analysed using Fourier transformation to obtain the frequency spectrum, which shows the intensity of different frequency components present in the laser emission.

4.1.3. Important parameters extracted from LIV curve and emission spectrum.

From LIV curve such parameters as built in potential (V_o), current threshold, current density, external differential quantum efficiency and series resistance can be obtained. Having LIV curves of the same sample but under different temperatures makes it also possible to determine characteristic temperature T0 of the device.

V_o parameter is the interception of the slope of Voltage curve with the Y axes and it represents the necessary voltage drop for the diode to be conductive (Fig. 4.1). Light emitting device should have the diode voltage equal to the bandgap energy divided by the elementary charge [1]. But in practice this value is normally bigger because of the voltage drop happening in different parts of the structure (can be due to p-n junction voltage drop, trapping of carries, etc..).

Current threshold is the minimum current value needed for the device to switch from the spontaneous emission to the stimulated radiation and it represents where the gain in the device exceeds the losses. This value can depend a lot on the design of the device and the used

materials. To be able to compare lasers with different sizes – the threshold current density parameter is presented (J_{th}). J_{th} can be calculated by dividing the experimentally measured I_{th} by the area of the laser where current is injected (length of laser multiplied by mesa width).

Series resistance (R_s) determines the quality of the ohmic contacts on the device and can be determined by estimating the slope of the I-V curve. Low values of R_s can indicate the lower power consumption and less self-heating of the laser.

Another important parameter is external differential quantum efficiency, what appears to be the ratio of the emitted photon population by the injected carrier population. This parameter shows how the device is efficient in terms of converting the ejected electron hole pairs to output light. Differential quantum efficiency can be determined by the slope of the experimentally measured I-V curve.

Please use and describe simply using this new equation.

$$\eta_d = 2\frac{q}{h\nu}\frac{\Delta P}{\Delta I} \quad (4.1)$$

The characteristic temperature of a laser, also known as the T_o temperature, is a measure of the threshold current temperature dependence of the device. It represents the change in threshold current of a laser diode with temperature. It can be calculated using the Arrhenius equation, which relates the temperature dependence of the threshold current (I_{th}) to the characteristic temperature (T_o) [2]:

$$Ith(\Delta T) = Ith^{RT}\exp\left(\frac{\Delta T}{To}\right) \quad (4.2)$$

Where Ith^{RT} represents the threshold current at reference temperature and ΔT represents the deviation of the junction temperature from reference temperature. To be able to estimate characteristic temperature – device should be tested under various temperatures and for each temperature the I_{th} should be extracted. Higher values of T_o imply that the threshold current density of the device increase less rapidly with increasing temperatures. This translates into the laser being more thermally stable.

From the spectrum of the laser emission such parameters as side mode suppression ratio (SMSR), tuning rates and free spectral range (FSR) can be extracted. Obtained spectrums also show user if the device is mono mode or single mode and if there are any mode hopes during tuning. SMSR represents the relation of power between centre peak longitudinal mode with the nearest higher order mode. This ratio is important for single mode devices, and it represents how efficiently the grating is able to supress other modes. It can be estimated by following relation:

$$SMSR = 10\, log\, (P1/P2) \quad (4.3)$$

where P1 is the intensity of the main peak and P2 is the intensity of the pick of most intense mode.

The tuning rate of a laser device quantifies its ability to alter its emission wavelength in response to variations in operating conditions, such as changes in applied current (current tuning) or shifts in temperature (temperature tuning).

The free spectral range (FSR) in laser diodes refers to the spacing between adjacent longitudinal modes of the laser emission. It represents the frequency or wavelength separation between two consecutive peaks in the laser's optical spectrum. To estimate the free spectral range in a laser diode it is needed the information about the diode's cavity length and refractive index. The FSR can be calculated using the following formula:

$$FSR = \frac{c}{(2 * n * L)} \quad (4.4)$$

Where FSR is the free spectral range, c is the speed of light in a vacuum, n is the effective refractive index of the laser medium and L is the cavity length of the laser diode.

4.2 Results on custom Fabry-Perot laser diodes with thin upper cladding and thin top contact layers.

In this chapter novel Fabry-Perot laser diodes with different thicknesses of upper cladding and top contact layers based on AlGaAsSb quantum wells are presented. To achieve better laser performances, several studies on the modification of the laser structure organization were conducted before [3,4]. But unfortunately, most of the attention was dedicated to the design of active zone (to control the emitting wavelength) and the waveguides (to achieve better optical confinement). The importance of upper p-cladding thickness mostly being neglected and been designed in a way to be sure that thickness is enough to keep the mode confined. While the modification and precisely thinning of the upper cladding can lead to several advantages, such as decrease of the growth time and material consumption and increase of the performance for a certain DFB configuration. The design of DFB laser-diodes, which would be the most effected

by the p-cladding layer thickness, is the one where the grating is placed on the top of the laser ridge [5], instead of using a wall corrugation along the ridge [6] or an epitaxial regrowth on the active zone [7]. Standard layer thicknesses prevent a device from having a good coupling with the grating as grating is too far away from the active zone. The typical thickness of the upper cladding for antimonide DFB laser diodes is 1,3-1,4 µm and thickness of top contact is 0.4-0.5 µm.

Study started with the realization of Generation 1 of Fabry-Perot laser diodes, which represent devices with thicknesses of upper cladding layers of 0.4 – 0.7 µm and top contact layer thickness of 0.35 µm. All devices were characterised in continuous wave regime, obtaining LIV curves under different temperatures (15° – 30°). As an example, LIV curve for the sample with upper cladding of 0.5 µm is presented on the Fig. 4.2 (a), as it is considered the most promising one in terms of output power and I_{th}. The power of the sample was going up to 15 mW and I_{th} was 75 mA. On Fig. 4.2 (b) also presented I-V curves under different temperatures for the same sample.

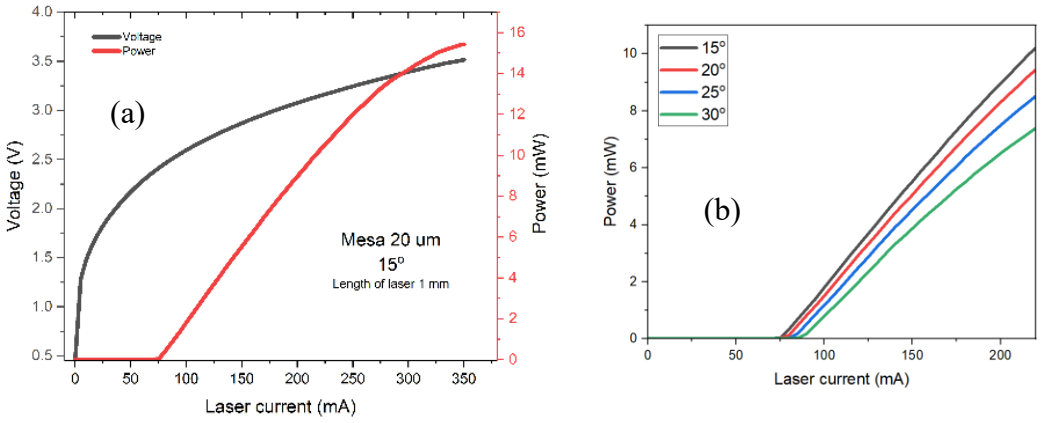


Figure 4.2. (a) - LIV curve (measured at 15°) of 1 mm length laser with ridge width of 20 µm (Generation 1), upper cladding thickness 0.5 µm; (b) - I-V curved under different temperatures of 1 mm length laser with ridge width of 20 µm (Generation 1), having thickness of upper cladding 0.5 µm

To compare data achieved by all the samples, J_{th} was estimated and plotted on the same graph for all devices of generation 1 (Fig 4.3). One can observe J_{th} for devices with different thicknesses of upper cladding and different widths of laser ridge. The lowest J_{th} were achieved for devices with

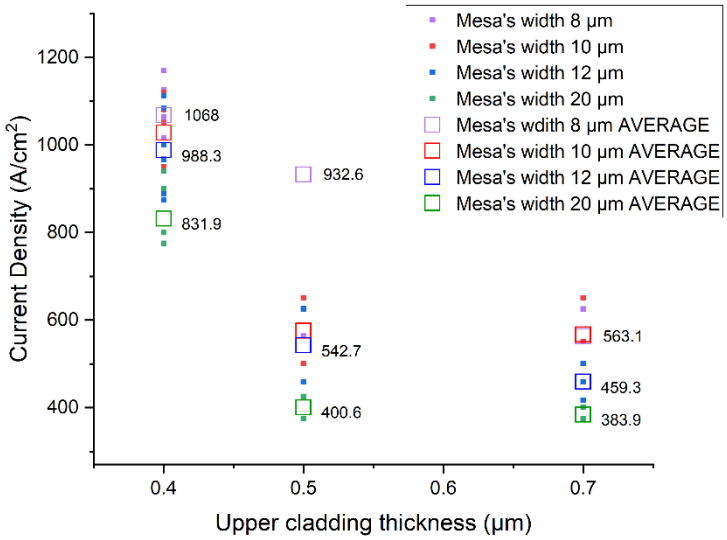


Figure 4.3. J_{th} versus upper cladding thickness for all fabricated samples of Generation 1 (empty squares = mean values)

Mesa width of 20 µm and thicknesses of upper cladding of 0.7µm (383,9 A/cm^2) and of 0.5 µm (400.6 /cm^2), which falls in normal range for the Jth of such devices (200-800 A/cm^2) , but not the lowest achieved so far [8.9].

Even with an upper cladding as thin as 0.4 µm, the lasers continued to operate effectively, exhibiting a threshold current density (Jth) of 631.9 A/cm² and output power of 7 mW. One can clearly see that J_{th} is increasing with the decrease in thickness of upper cladding, due to reduced optical confinement, leading to increase in optical losses. As a result of thin upper cladding layers, a big portion of the optical mode leak into the cladding layers, increasing the interaction with other layers of the device, following with scattering, absorption, or leakage into the surrounded materials [10,11].

To compare the power output among samples with varying upper cladding thicknesses, a graph illustrating the maximum achieved power values for these samples is displayed in Figure 4.4.

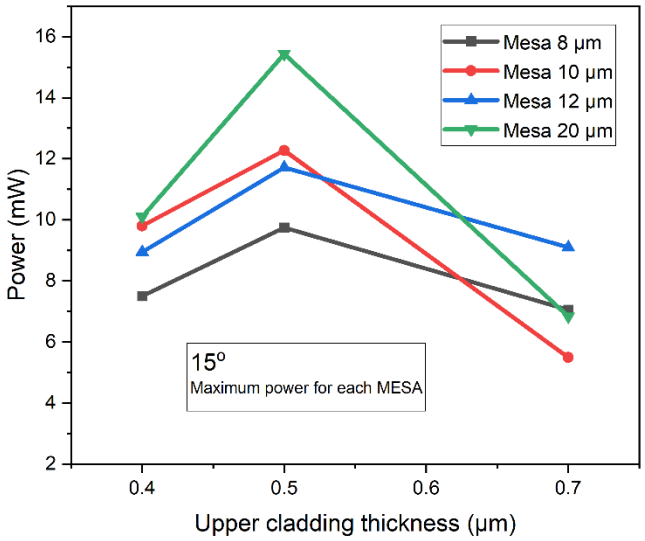


Figure 4.4. Power versus upper cladding thickness for all fabricated samples of Generation 1

Such parameters as characteristic temperature T_0 and serial resistance were evaluated and these parameters for all devices were in an expected range keeping T_o between 65 K and 180 K [12] and R_s between 4-6 Ω [13]. All of them were working at relatively high voltages (3V), what is explained by issues during the growth leading to a low N-dopping level for the upper cladding layer.

After seeing the potential in samples with thinner upper cladding, next objective was to improve the performance. Generation 2 of Fabry-Perot laser diodes differs by thickness of GaSb top contact layer (down to 0.2 µm) and the thickness of upper cladding varies from 0.3 to 0.5 µm. First, all devices were tested as well in CW mode under different temperatures, obtaining LIV curves, presented example is on Fig. 4.5 (a) for a sample with upper cladding of 0.5 µm and mesa width of 20 µm. I-V curves were also obtained at different temperatures (Fig. 4.5 (b)).

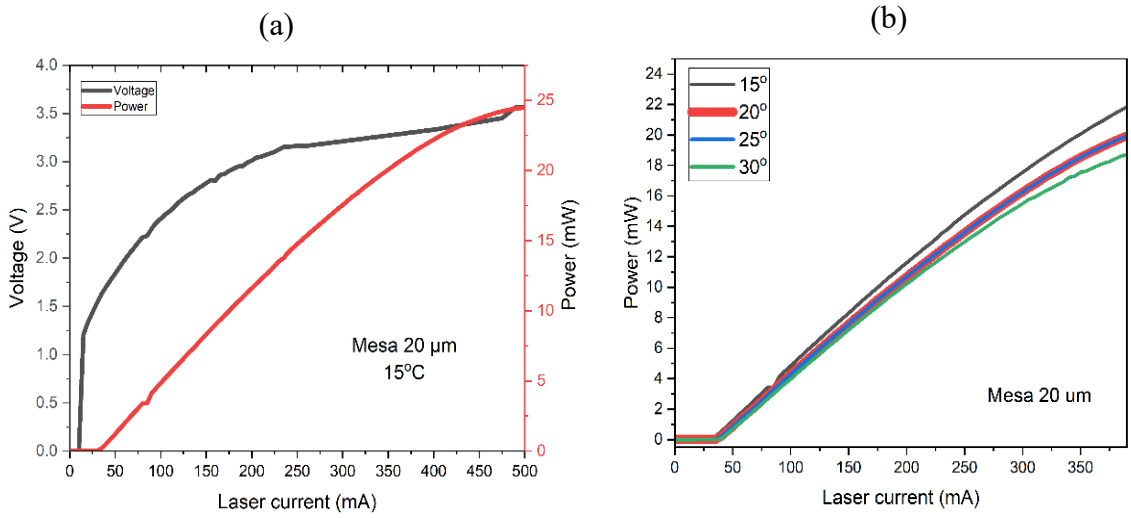


Figure 4.5. (a) - LIV curve (measured at 15°) of 1 mm length laser with ridge width of 20 µm (Generation 2), having thickness of upper cladding 0.5 µm; (b) - I-V curved under different temperatures of 1 mm length laser with ridge width of 20 µm (Generation 2), having thickness of upper cladding 0.5 µm

One can clearly observe that the performance improved compared to the same sample from 1st generation, I_{th} dropped down to 25 mA and the power went up to 25 mW. On Fig. 4.6 are presented J_{th} for all samples obtained from generation 2, where J_{th} dropped down to 138 A/cm^2.

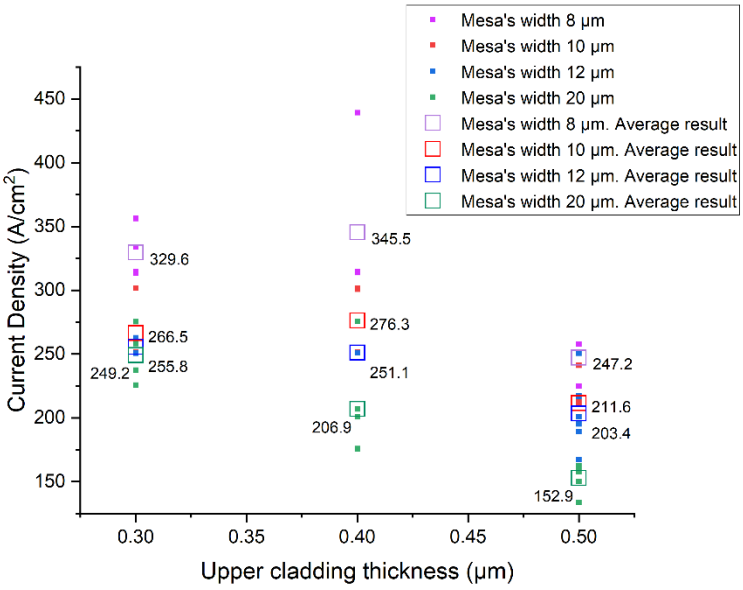


Figure 4.6. Jth versus upper cladding thickness for all fabricated samples of Generation 2 (empty squares = mean values)

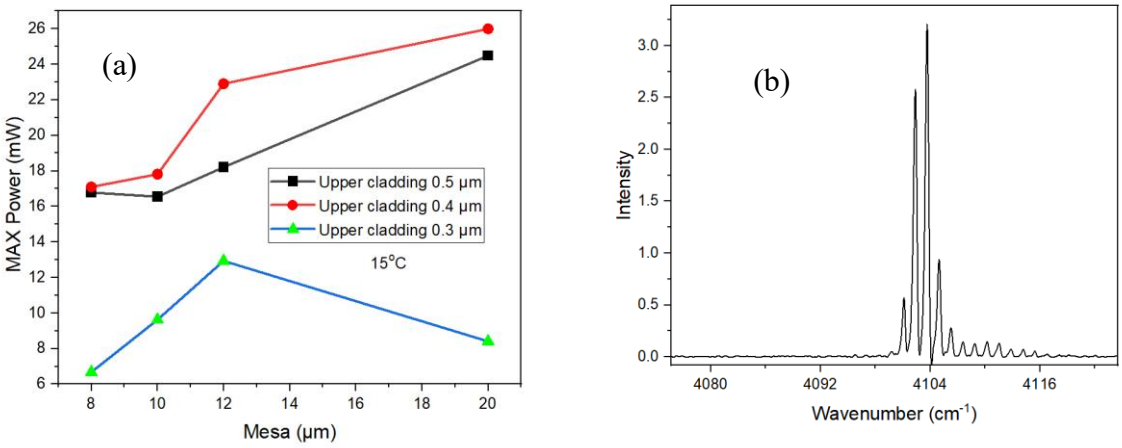


Figure 4.7. (a) - Power versus width of mesa for all thicknesses of upper claddings in samples fabricated for Generation 2; (b) – Spectrum of Fabry-Perot laser diode with thickness of upper cladding 0.5 µm

Upper cladding in this generation was thinned down to 300 nm, and even at such thickness devices were able to perform promising results reaching J_{th} down to 249.2 A/cm^2. On Figure 4.7 (a) can be visible progression of maximum value of output power for all samples from

Generation2. As an example, the spectrum of sample from Generation 2 with thickness of upper cladding 500 nm (wafer V3346) is presented (Fig. 4.7 (b)).

Lower threshold currents take place because thinner layer reduces the electrical resistance and can provide better electrical contact to the underlying layers, what improves the current spreading and enhances the injection of carriers into the active region. Thinner top contact layer also improves heat dissipation, as less material is present to trap the heat within device. Experimental results proved that thinning of top contact layer led us to higher power and lower J_{th} at the same width of the ridge and same lasing conditions. T_0, R_s have been calculated and results in average respectfully are: 70 K, 3.5 Ω. Serial resistance is lower than for samples of Generation 1, confirming the hypothesis stated above.

Conclusion.

Presenting results on custom Fabry-Perot laser diodes, it has been proved that standard thickness of upper cladding layer and top contact layer can be thinned down to 0.5 μm and down to 0.2 μm respectively without any degradation of laser performance, leading to convenient values for threshold current and emitted power in continuous wave regime. This work paths the way to DFB laser diodes developments improving the coupling of the guided mode with a grating on top of the laser ridge. Results of the investigation of such devices are presented in the next chapter.

4.3 Results on custom DFB laser diodes with thin upper cladding and thin top contact layers with grating on the top of the laser ridge (fabrication in Montpellier)

DFB laser diodes based on GaSb have shown valuable performances in recent years: low threshold currents, about 27 mA for 830 μm long device [14] , high output power of 60 mW [15] and single mode operation with SMRS reaching 50 dB [16]. Most of the recent DFB laser diodes have lateral

grating along the ridge [17,18] or corrugation of the sidewalls [6]. Another technique for DFB fabrication is the use of buried grating, where GaSb based components have exhibited threshold current of 57 mA for 1500 µm -long devices and output power of 25 mW [7]. To compete with mentioned above performances, we demonstrate another type of DFB laser diodes with a grating on the top of the ridge, having a good potential [5]. In this part of the manuscript, we present GaSb based DFB laser diodes with an etched grating on the top of the ridge, emitting at 2.4 µm and having thinner layer's structure to optimise the coupling between the DFB grating and lasing mode. The grating period of presented lasers was 346 nm and duty cycle 50%, all devices has cavity length of 1 mm. This DFB laser diodes were based on the promising results of novel Fabry-Perot laser diodes (presented in previous section) and were processed on the same wafers as second generation of them with 0.5 µm thick upper cladding.

On Fig. 4.8 (a) is reported the power and tension versus injected current of the devices measured in continuous wave regime. The power per facet reaches 9 mW with a threshold current of 25 mA at 20°C for cavity length of 1 mm (J_{th} = 500 A/cm^2). It can be noticed that voltage is not as

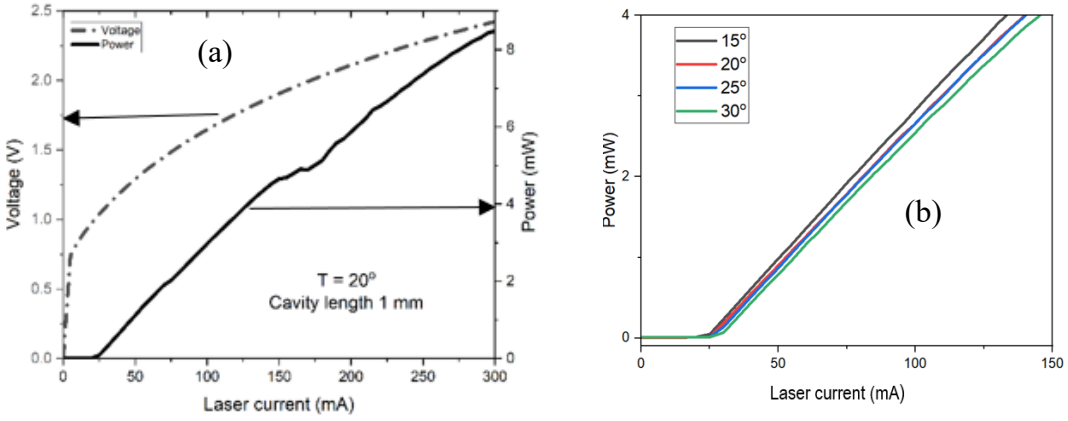


Figure 4.8. (a) - Emitted power and potential versus injected current of a DFB device, L = 1 mm, T = 20°C; (b) – emitted power versus injected current at different temperatures, L = 1 mm.

high as for the Fabry-Perot samples processed on the same wafer. The reason for that is that

voltage characteristics of a laser diode can be subject to variations arising from the intricacies of the fabrication process. Specifically, the passivation steps during fabrication have the potential to impact the electrical properties of the laser diode, including its leakage current. Additionally, the metallization process involved in creating electrical contacts can also exert an influence on the voltage (V) behaviour of the laser diode. The I-V curves of sample under different temperatures can be seen on Fig 4.8 (b). The spectrum was obtained using a Fourier-transform infrared spectrometer (FTIR) and is presented on Fig. 4.9, where a single mode operation is clearly observed. Device has emission at 2.42 μm (T = 20ºC) and at least (due to FTIR resolution) 25 dB side mode suppression ratio. The characteristic temperature, obtained from the Fig. 4.8(b) appears to be 66 K, which is slightly less than standard value for such structures [12]. It can be due to epi side up mounting, which does not allow an efficient temperature extraction. The external differential quantum efficiency is 5.3 %, lower than typical value [14] and it can be due to lack of facet coating and much thinner upper cladding layers [19] compared to standard devices. The electrical characterizations give an internal resistance of 4.3 Ω and the built-in potential of 1.2 V.

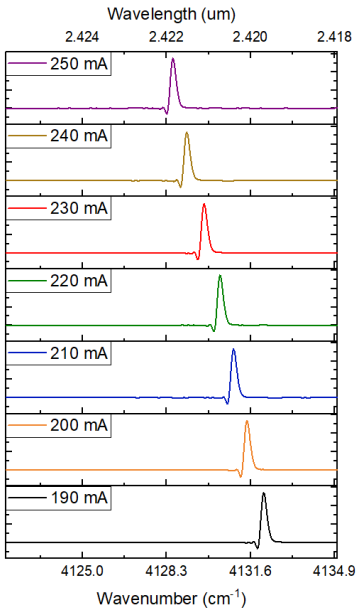


Figure 4.9. Emission spectra of a 1 mm-long device at different currents, T=20°C

Total of 15 DFB lasers been produced, showing similar performance. 9 lasers out of 15 work in continuous tuning regime, showing a single frequency operation starting from I_{th} up to 300 mA, with no mode hops. Another 2 devices show single mode operation only at low currents (below 170 mA) and remaining 3 devices are single mode on high currents (240 mA up to 320 mA)

On Fig. 4.10 (a) is reported the current tuning of the presented DFB laser diode. The laser current was changed from 60 mA up to 300 mA and the longitudinal mode shifted from 4138.134 cm^{-1} to

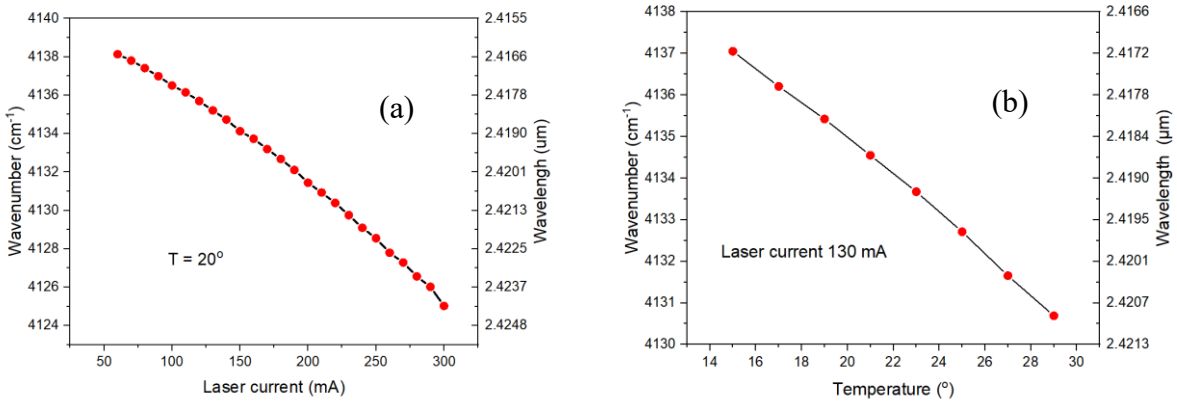


Figure 4.10. (a) - Current tuning of the device at the fixed temperature, T= 20°C; (b) – Temperature tuning of the device at the fixed current 130 mA

4125.025 cm^{-1}, giving an average tuning rate of 0.032 nm/mA. The device was not tested above 300 mA in order to avoid possible thermal degradation. Temperature tuning was performed as well, can be seen on the Fig. 4.10 (b). Within 14° we had a change of 6358 cm^{-1}, giving an average tuning rate of 0.27 nm/°C.

Laser bar with presented DFB laser diode and other 3 functioning devices were mounted in custom housing (Fig. 4.11).

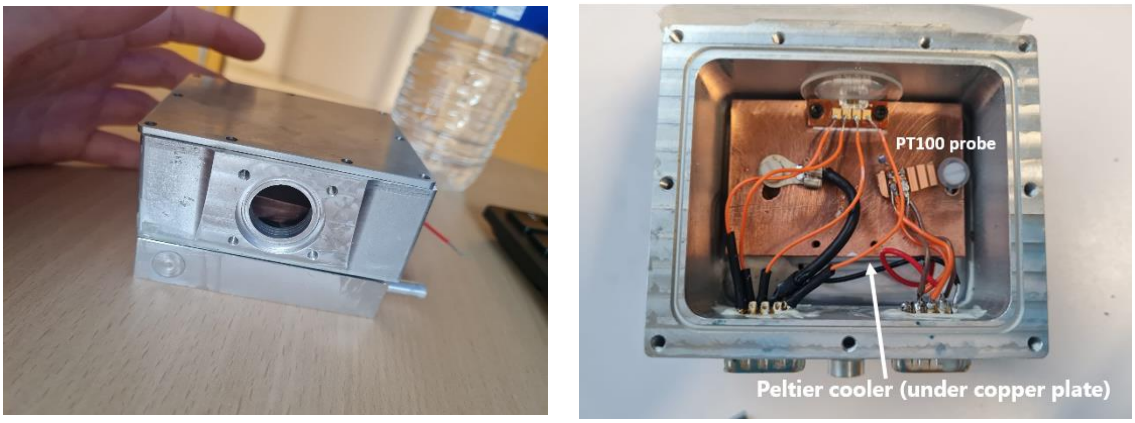


Figure 4.11. Photograph of the packaging (inside and outside view) for the laser bar with 4 DFB laser diodes 1 mm cavity length

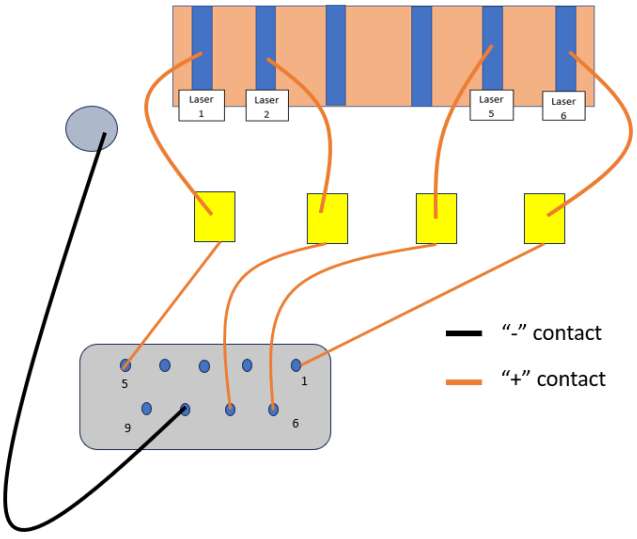


Figure 4.12. Map of connections for all DFB laser diodes and the pin map for output of housing

The laser bar was mounted on copper heat-sink and was carefully adjusted in front of the window in order to assure proper beam direction. Heat dissipation and regulation on the device was provided by the thermoelectric cooler (TEC) and a PT100 probe. The TEC was in direct contact with the laser heat sink through the copper substrate and is common for all 4 devices and thermal interface material was used between the copper base and the heat-sink of the laser bar. Each of the four lasers shares a common ground and negative contact, but in order to independently operate each device within the laser bar, it was necessary to establish individual positive contacts for all of them. This was accomplished by bonding golden wires to the top surface of each device, with the other ends of these wires being attached to four separate ceramic plates. These ceramic plates were used to redirect the positive contact to the pins located on the laser housing. Figure 11 provides an internal view of the packaging, showing all the visible contacts, while Figure 12 illustrates the connectivity plan and pin arrangement of the packaging's output. The collimation lens was not set into the packaging and later on was installed externally. Packaging was tested and all lasers performed correctly. The temperature of the device was successfully controlled by TEC and during testing it was cooled down to 10ºC and heated up to 75ºC. The beam was collimated using the C036TME lens (NA= 0.56) from Thorlabs which has

focal length of 4 mm and working distance of 2.67 mm. Such small working distance allowed us to capture the most from the originally diverging beam.

All DFB laser diodes on the packed laser bar have similar performances and all their characteristics can be found in table 4.1. All packed devices are suitable for HF gas sensing, reaching absorption lines at 4095.439 cm^{-1} and 4123.993 cm^{-1}. Figure 4.13 displays the Hitran simulation of HF absorption lines in comparison to standard air. It is evident from the figure that these mentioned absorption lines are not only notably intense and distinctly separated but also remain free from interference with standard air constituents. Taking into consideration this fact,

Laser	Ith (at 20°C), mA	Max power (at 300 mA), mW	SMSR, dB	Vo, V	Rs, Ohm	To, K
1	25	8	21	1.3	3.7	61
2	25	8.1	23	1.2	3.5	66
5	20	8.4	22	1.3	3.7	67
6	30	7	25	1.3	4.7	64

Table 4.1. Characteristics of packed DFB laser diodes

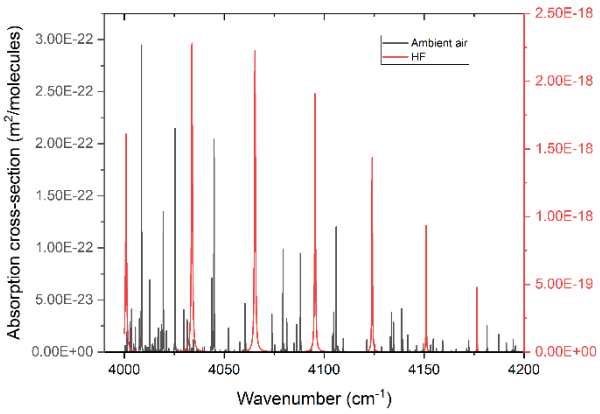


Figure 4.13. HITRAN simulation of HF absorption lines against standard air

along with the sufficient power and SMSR of the devices – these DFB laser diodes can allow low detection limits for the gas sensing and precise detection of HF in industries.

4.4 Results of Custom DFB Laser Diodes with thin upper cladding and thin top contact layers fabricated at Nanoplus

All devices stated in this section were fabricated and tested using facilities of industrial company Nanoplus. It is important to state that all samples mentioned below were tested in CW mode under temperature of 20ºC and all were 1 mm long. Laser diodes with grating on the top of the

Name of the sample *specifics of design	Thickness of upper cladding	Position of grating	Period of grating
V3344TOP	400 nm	On the top of the laser ridge	346-358 nm (step of 4 nm)
V3346TOP	500 nm	On the top of the laser ridge	346-358 nm (step of 4 nm)
V3344 Lateral 1 *smaller laser ridge	400 nm	Grating along the ridge	350 -362 nm (step of 4 nm)
V3344 Lateral 2	400 nm	Grating along the ridge	350 -362 nm (step of 4 nm)
V3346TOP	500 nm	On the top of the laser ridge	346-358 nm (step of 4 nm)
V3346 Lateral 1	500 nm	Grating along the ridge	350 -362 nm (step of 4 nm)
V3346 Lateral 2 *no electroplated contact	500 nm	Grating along the ridge	350 -362 nm (step of 4 nm)

Table 4.2. All designs fabricated at Nanoplus

laser ridge had periods of the grating starting from 346 nm going up to 358 nm with the step of 4 nm. Samples with the lateral grating along the ridge had variation of grating period from 350 nm to 362 nm with the same step. For each laser design, samples were fabricated based on 2 wafers

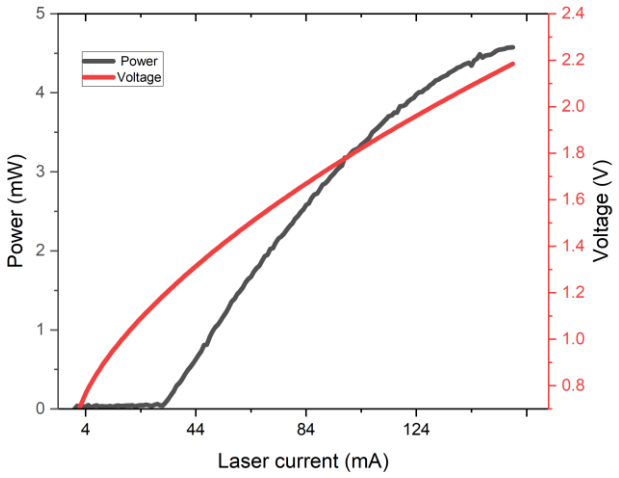


Figure 4.15. Emitted power and potential versus injected current of a DFB device V3346TOP, L = 1 mm, T = 20°C

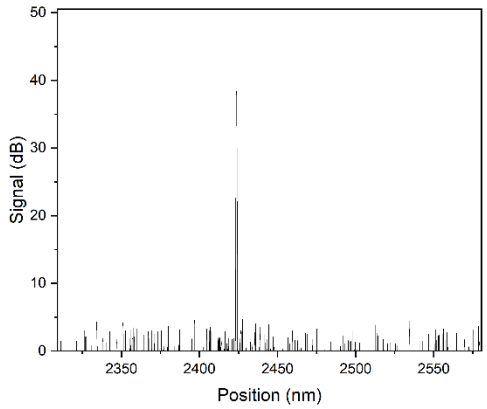


Figure 4.16. Spectrum of DFB device V3346TOP, T = 20°C, I =140 mA

from second generation with thinner layer organisation used before, V3346 (thickness of upper cladding 0.5 µm) and V3344 (thickness of upper cladding 0.4 µm). All devices underwent testing, with an average of nine devices evaluated for each grating period and design. However, for the initial assessment presented below, we focus only on the devices with the smallest grating period in each respective design—346 nm for top samples and 350 nm for lateral grating samples

(as they have best SMSR value). Table 2 provides a comprehensive list of the fabricated and tested designs to facilitate their identification.

4.4.1. Top grating samples fabricated at Nanoplus

To validate the successful operation of the top grating DFB laser diodes with thin upper cladding and top contact layers, two samples were manufactured. The first sample featured an upper cladding thickness of 400 nm, while the second one had an upper cladding thickness of 500 nm. Both samples included a 200 nm-thick top contact layer. An illustrative example of the LIV curve is provided in Figure 4.15, depicting a laser diode with a grating period of 346 nm and an upper cladding thickness of 500 nm. The threshold current (I_{th}) is 32 mA, and the laser's power output reaches 4.4 mW per facet at 150 mA. The laser emission wavelength was measured at 2423 nm under 20°C at a current of 140 mA (Figure 4.16). The device exhibited single-mode emission with a Side Mode Suppression Ratio (SMSR) of 35 dB.

Additionally, parameters as Vo and Rs were were estimated and are as followed: 1.0 V, 7 Ω.

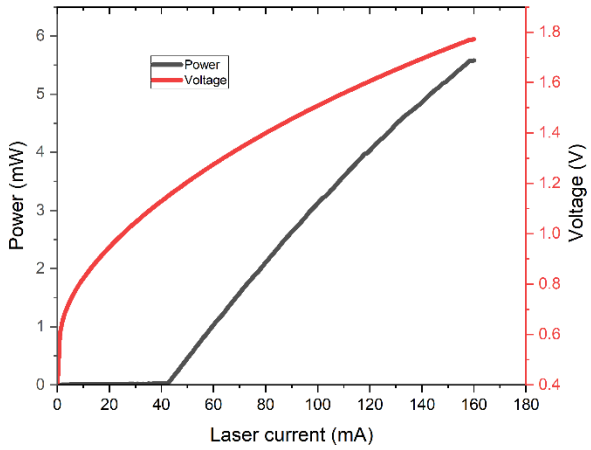


Figure 4.17. Emitted power and potential versus injected current of a DFB device V3344TOP, L = 1 mm, T = 20°C

Unfortunately, T_0 couldn't be calculated as compounds were tested only under one temperature. Devices featuring identical cavity dimensions and grating periods were produced on a wafer with

an upper cladding thickness of 400 nm. This was done to investigate the potential impact of further reducing the upper cladding thickness on device performance and to confirm whether the outcomes would correspond to the earlier presented results on studies of thinning of upper cladding and top contact layers in previous sections. On Fig. 4.17 LIV curve is presented. Presented device with upper cladding thinned down to 400 nm has I_{th} of 43 mA and power is

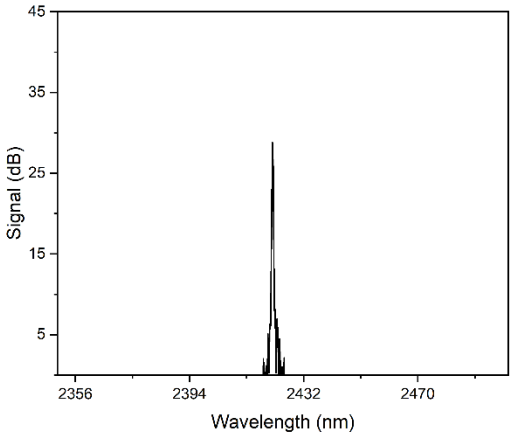


Figure 4.18. Spectrum of DFB device V3344TOP, T = 20°C, I =140 mA

going up to 5.2 mW. From voltage curve, R_s was estimated to be 5.2 Ohm and V_0 to be 0.97 V.

Spectrum is shown on Fig 4.18 with emission at 2.42 μm having SMSR of 29 dB. Comparing with the previous sample it can be clearly seen that thinning of the upper cladding led to increase of I_{th} and decrease of Power, what confirms the results obtained on the Fabry-Perot laser diodes in section 4.2 for the same reasons. Results on presented DFB laser diode with top grating and thinner layer organisation can't be fairly compared with DFB laser diode based on same wafer but processed in Montpellier, as different techniques and materials were used for fabrication (different insulation layers, different metal contacts and etc.). It can be confidently asserted that these results confirm the significant promise of such a configuration for DFB laser diodes, and that these devices are well-suited for real-world applications in gas sensing setups. Furthermore,

it is noteworthy that this device can be consistently manufactured with nearly identical performance.

4.4.2. Samples with lateral grating along the ridge fabricated at Nanoplus

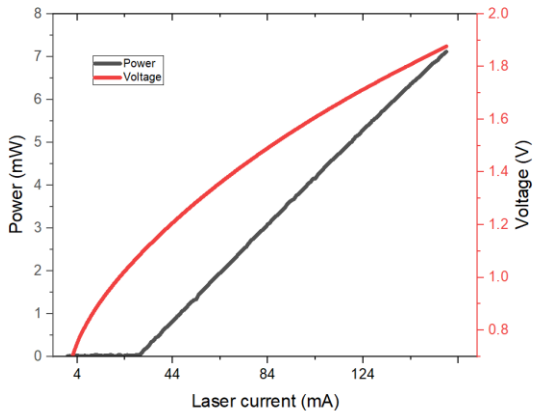


Figure 4.19. Emitted power and potential versus injected current of a DFB device V3346 Lateral 1, L = 1 mm, T = 20°C

Currently, one of the most spread designs for DFB lateral diodes involves a lateral grating positioned alongside the laser ridge. This design is extensively employed by Nanoplus in many of their commercially accessible laser chips. Four samples with lateral gratings along the ridge were produced using the same wafers as the top grating samples (V3344 and V3346). LIV curves and emission spectrums were measured from each device. Characterisation of one of the devices with upper cladding thickness of 500 nm can be seen on Fig. 4.19 and Fig. 4.20 (sample with period of grating of 346 nm).

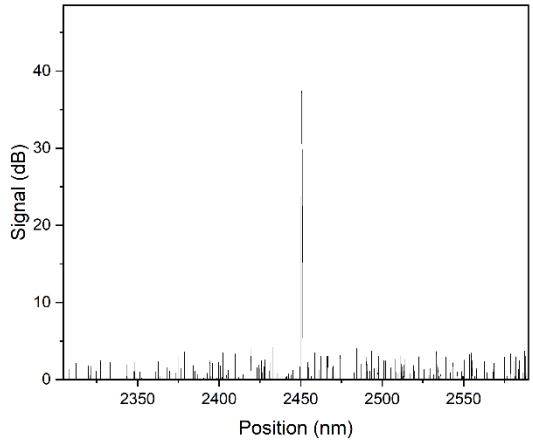


Figure 4.20. Spectrum of DFB device V3346 Lateral 1, T = 20°C, I =140 mA

Straight away can be noticed that even if the behaviour of the samples appeared to be better in terms of emitted power and threshold current, it doesn't significantly differ from the top sample's performance, having I_{th} of 30 mA and reaching 6,6 mW at 150 mA. SMSR for this device was 34 dB. Device from sample V3344 Lateral 2 expectably showed higher I_{th} (35 mA) with same cavity length of devices and lower output power (3.9 mW at 150 mA) (Fig.21 (a)), decrease of

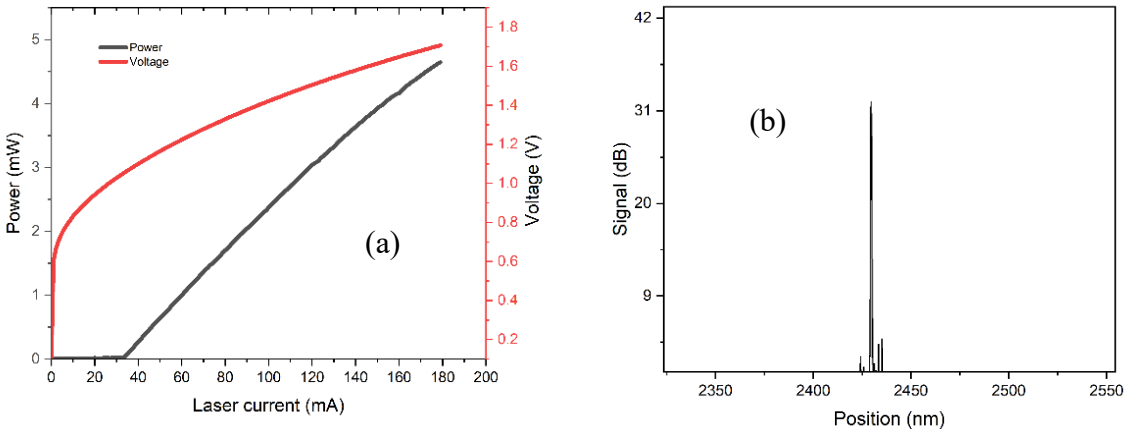


Figure 4.21. (a) Emitted power and potential versus injected current of a DFB device V3344 Lateral 2, L = 1 mm, T = 20°C; (b) - Spectrum of DFB device V3346 Lateral 1, T = 20°C, I =140 mA

performance caused the same effect as for the top grating samples. Spectrum (Fig. 4.21 (b)) showed SMSR of 29 dB. Rest of parameters can be found in table 4.3.

4.4.3. Discussion and summary

Sample	I_{th}, mA	Max power at 150 mA, mW	SMSR, dB	V_o, V	R_s, Ohm
V3346TOP	32	4.4	35	1.01	7
V3344TOP	43	5.2	29	0.97	5.2
V3346 Lateral 1	30	6.6	33	0.99	4.5
V3344 Lateral 1	33	3.5	29	0.91	4.7
V3346 Lateral 2	30	6.2	37	1.09	5.07
V3344 Lateral 2	35	3.9	34	0.9	5.7

Table 4.3. Characteristic of all samples fabricated at Nanoplus

For each design detailed in this section, the average values for both the threshold current (I_{th}) and output power were calculated and are depicted in Figure 4.22 (a) for I_{th} and Figure 4.22 (b) for power. Additionally, average values for I_{th} and output power per facet were included in the same plot for DFB laser diodes with gratings positioned on the top of the ridge, which were fabricated

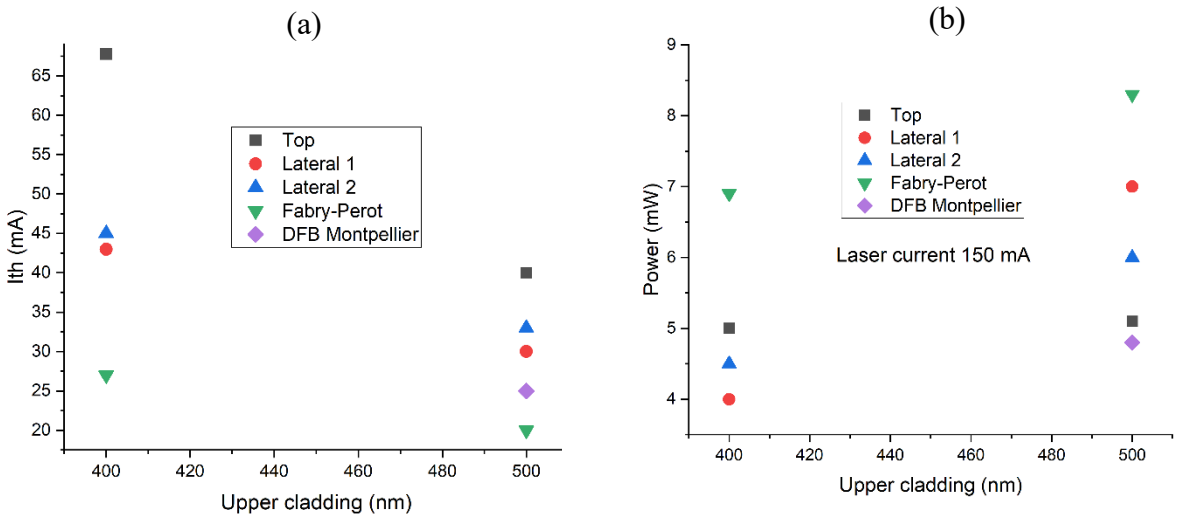


Figure 22. (a) - Average I_{th} plotted against thickness of upper cladding for all samples presented in this chapter; (b) – Average output power plotted against thickness of upper cladding for all samples presented in this chapter

in Montpellier, as well as for Fabry-Perot samples processed on the same wafers. From average data from Fig 4.22 (a) and Fig. 4.22 (b) can be seen that the trend with decrease performance for thinner upper cladding is confirmed both for top grating and grating along the ridge samples. From above graphs it can be observed that even if lateral grating is very stable and mature technique – the results of samples with grating on the top of the laser ridge show very comparable performance, and with future development potentially can be fully integrated to the market. When examining top grating DFB laser diodes, a comparison was made between results from several DFBs produced in Montpellier and other samples fabricated at Nanoplus. It seems that the power output is similar for both samples, but there is a significant increase in the

threshold current for the device fabricated at Nanoplus. To investigate this notable increase in I_{th}, the distribution of I_{th} for all samples featuring top gratings and produced at Nanoplus was plotted (Figure 4.23(a)). It appeared to be a huge spread between the values resulting in such a high average number for threshold current. It can be noticeable that there were samples with relatively the same Ith as for DFBs fabricated in Montpellier. To study further, we plotted average I_{th} value for each period of grating for V3346TOP and V3344TOP samples (Fig 4.23 (b)). Lowest I_{th} (and comparable values with DFBs processed in Montpellier, mentioned in section 4.3) showed up for the grating period of 346 nm. The increase in the threshold value was noticeable for both wafers as the grating periods became larger. There could be several reasons for this phenomenon. DFB laser diodes operate by controlling the resonant wavelength of light within the laser cavity using

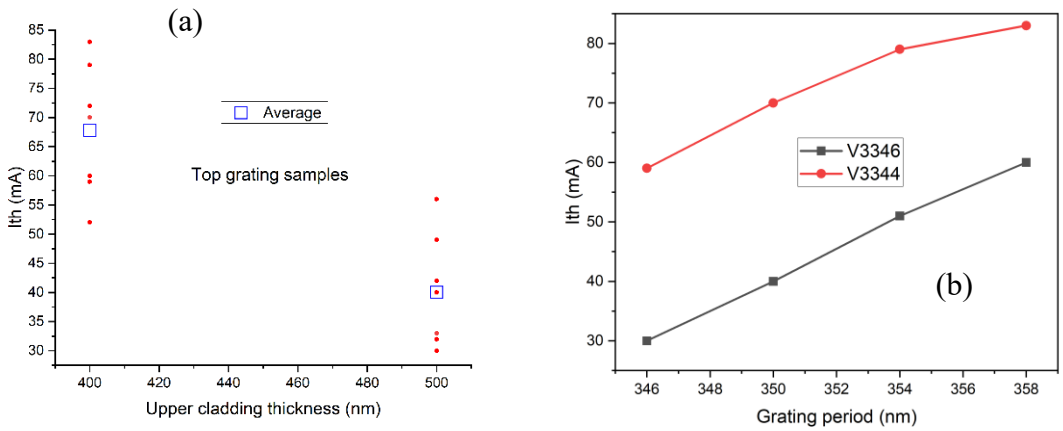


Figure 4.23. (a) - Average values of I_{th} for samples with top grating fabricated at Nanoplus; (b) - I_{th} against the grating period for top grating samples fabricated at Nanoplus

the grating. Increasing the grating period can cause a shifted resonant wavelength, potentially shifting the laser mode away from the ga in peak of the active medium. This can result in weaker gain for the desired lasing mode and stronger competition from other modes, leading to a higher threshold current. Additionally, the coupling coefficient between the grating and the optical mode may change with the grating period. Ultimately, the performance of the top grating device produced in Nanoplus with a grating period of 246 nm, the same as that used for the packaged

devices in Montpellier, exhibited similar results to those obtained in Montpellier. This underscores the stability of such a grating configuration and its potential as a strong contender in the market of GaSb-based DFB laser diodes. Sustainability of such design was further reinforced by comparing it with a fabricated device that had a lateral grating along the ridge (mature technology).

In this chapter we first presented a study on Fabry-Perot laser diodes with different thicknesses of upper cladding and contact layers. It has been proved that standard thickness of upper cladding layer (1.3-1.4 μm) and top contact layer (0.35-0.45 μm) can be thinned down to 0.5 μm and down to 0.2 μm respectively without any degradation of laser performance, leading to convenient values for threshold current and emitted power in continuous wave regime. This work pathed the way to DFB developments.

Based on achieved results on Fabry-Perot laser diodes, later were presented DFB laser diodes that exhibit stable single frequency operation across the entire current tuning range and demonstrate sufficient performances in terms of threshold current and optical output power. Laser devices are based on modified waveguides with thinner contact and cladding layers to be able to etch the DFB grating on top of the laser ridge. Decreasing the upper cladding thickness down to 500 nm and top contact layer down to 200 nm allows for an increased coupling factor by bringing the grating closer to the active zone. Output power of 9 mW per facet has been achieved. Characterization showed I_{th} of 25 mA for 1 mm-long device. Single mode emission at 2.42 μm with SMRS of 25 dB was obtained and is comparable with the already demonstrarted value for top grating samples. Current DFB laser diodes demonstrate a tuning rate of 0.032 nm/mA, enabling them to target two distinct and well separated HF absorption lines positioned at 4123,993 cm^{-1} and 4151.035 cm^{-1}. The

fabricated devices were packed in custom housing and offer the potential for use in tunable laser gas sensing setups, thanks to their sufficient SMSR, output power and tuning properties.

Stability of the proposed design was confirmed by fabrication and characterization of similar devices with same grating configuration at industrial company Nanoplus, achieving comparable values for I_{th} (32 mA), output power per facet (4.4 mW at 150 mA) and SMSR (35 dB). At Nanoplus facility, DFB laser diodes with lateral grating along the laser ridge (mature technology at the company) were fabricated on same wafers as top grating samples, which performance confirmed that devices with grating on the top of the laser ridge can compete on the market with existent designs. Two devices from Nanoplus samples were packed into the TO66 packaging, which can be used to target CH_4 pick at 4176.647 cm^{-1} and NH_3 pick at 4173.126 cm^{-1}.

Reference

[1] Schubert EF. Light-Emitting Diodes. Cambridge: Cambridge University Press; 2006. doi:10.1017/CBO9780511790546

[2] Zhang, Maki Kushimoto, Akira Yoshikawa, Koji Aoto, Chiaki Sasaoka, Leo J. Schowalter, Hiroshi Amano; Key temperature-dependent characteristics of AlGaN-based UV-C laser diode and demonstration of room-temperature continuous-wave lasing. *Appl. Phys. Lett.* 28 November 2022; 121 (22): 222103. https://doi.org/10.1063/5.0124480

[3] G. M. Smith et al., "Very narrow linewidth asymmetric cladding InGaAs-GaAs ridge waveguide distributed Bragg reflector lasers," in IEEE Photonics Technology Letters,1996,8(4), pp. 476-478, , doi: 10.1109/68.491088

[4] Jiao Z, Gu Y, Zhang Y, Hu A, Gong Q, Wang S, Li T and Li X, Effect of Ridge Width on the Lasing Characteristics of Triangular and Rectangular InAs/In0.53Ga0.47As Quantum Well Lasers, Front. Mater, 2022, doi: 10.3389/fmats.2022.833777

[5] H. Zhang, D. A. Cohen, P. Chan, M. S. Wong, S. Mehari, D. L. Becerra, S. Nakamura, S. P. DenBaars, "Continuous-wave operation of a semipolar InGaN distributed-feedback blue laser diode with a first-order indium tin oxide surface grating", Opt. Lett. **44**, 3106-3109 (2019)

[6] Q. Gaimard. A. Larrue, M. Triki, “2.2 um to 7.7 um side wall corrugated index coupled DFB GaSB based laser diodes”, Semicond. Sci. technol. 30, 065015 (2015)

[7] Q. Gaimard, L. Cerutti, R. Teissier and A. Vicet, Distributed feedback GaSb based laser diodes with buried grating, Applied Physics Letters, 2014, **104(**16), doi: 10.1063/1.4873356

[8] D. Barat et al., "Fabry-Perot laser diodes and DFB laser diodes emitting at 2.6μM for absorption spectroscopy," 2008 20th International Conference on Indium Phosphide and Related Materials, Versailles, France, 2008, pp. 1-3, doi: 10.1109/ICIPRM.2008.4702992.

[9] Adamiec, P., Bohdan, R., Bercha, A., Dybala, F., Trzeciakowski, W., Rouillard, Y. and Joullié, A. (2007), Threshold currents under pressure in InGaAsSb/AlGaAsSb laser diodes. phys. stat. sol. (b), 244: 187-191. https://doi.org/10.1002/pssb.200672533

[10] W. Streifer, R. D. Burnham, and D. R. Scifres, Quantum Electron,1976, **QE-12**(3), pp. 177

[11] D. C. Liu, C. P. Lee, C. M. Tsai, T. F. Lei, J. S. Tsang, W. H. Chiang, Y. K. Tu, Role of cladding layer thicknesses on strained-layer InGaAs/GaAs single and multiple quantum well lasers, *Journal of Applied Physics ,* 1993, doi: 10.1063/1.353917

[12] L.Cerutti, A. Vicet, E. Tournie, “Interband mid-infrared lasers” In : Mid-Infrared Optoelectronics, Woodhead Publishing (2020), p. 91-130.

[13] B. Stegmuller, B. Borchert and R. Gessner, "1.57 mu m strained-layer quantum-well GaInAlAs ridge-waveguide laser diodes with high temperature (130 degrees C) and ultrahigh-speed (17 GHz) performance," in *IEEE Photonics Technology Letters*, vol. 5, no. 6, pp. 597-599, June 1993, doi: 10.1109/68.219680.

[14] Q. Gaimard. A. Larrue, M. Triki, "2.2 um to 7.7 um side wall corrugated index coupled DFB GaSB based laser diodes", Semicond. Sci. technol. 30, 065015 (2015)

[15] S. Forouhar, R. M. Briggs, C. Frez, K. J. Franz, A. Ksendzov, "High-power laterally coupled distributed-feedback GaSb-based diode lasers at 2 μm wavelength", Appl. Phys. Lett. **100**, 031107, 1.3678187 (2012)

[16] J. Viheriälä, K. Haring, S. Suomalainen, R. Koskinen, T. Niemi, M. Guina, "High Spectral Purity High-Power GaSb-Based DFB Laser Fabricated by Nanoimprint Lithography," *IEEE Photonics Technology Letters* **28**, 1233-1236 (2016)

[17] C. Yang, S. Xie, Y. Zhang, J. Shang, S. Huang, Y. Yuan, F. Shao, Y. Zhang, Y. Xu, Z. Niu, "High-power, high-spectral-purity GaSb-based laterally coupled distributed feedback lasers with metal gratings emitting at 2 $\boldsymbol{\mu}$m", *Appl. Phys.* **114** (2): 021102, 1.5080266 (2019)

[18] H. Shixian, Y. Jinyi, C. Chun-fang, Y. Jing, Z. Xuyi, Y. Wenfu, A. Du, L. Ruotao, H. Wenxin, C. Yuanyu, *Phys. Scr.* **97**(12), 125014 (2022)

[19] D. C. Liu, C. P. Lee, C. M. Tsai, T. F. Lei, J. S. Tsang, W. H. Chiang, Y. K. Tu, "Role of cladding layer thicknesses on strained-layer InGaAs/GaAs single and multiple quantum well lasers", *Journal of Applied Physics* **73** (12), 8027–8034 (1993)

Chapter 5. Quartz enhanced photoacoustic spectroscopy.

5.1 PAS. Stare of art and theory

Photoacoustic spectroscopy (PAS) is a powerful analytical technique used to study the absorption properties of materials, particularly in the realm of photon-matter interactions. It provides valuable information about the absorption spectra of a wide range of substances, including gases, liquids, and solids.

PAS is a non-destructive analytical method that involves the generation of acoustic signals in a sample through the absorption of modulated electromagnetic radiation, such as laser light. These acoustic signals, which are proportional to the sample's absorption of light, can be detected and analyzed to determine the sample's absorption spectra, allowing for the identification and quantification of its constituent substances. Photoacoustic spectroscopy was discovered by Alexander Bell in 1880. Bell conducted early experiments in which he observed that materials could emit sound when exposed to sunlight. The real development of PAS started again in 1938 (Viegerov) for the study of a gas composition [1]. Later on PAS measurements were realized with minimum detection limit of ppm, using a broadband light source and a microphone. In 1960s the advancement of the laser sources allowed to PAS to make a real step forward [2]. Following the progress, detection limits in the ppb range were shown, with laser sources targeting CO2 absorption lines [3]. In 1976 Allan Rosencwaig and Allan Gersho developed the mathematical and experimental foundations of photoacoustic spectroscopy, making it a quantitative and highly sensitive technique for studying material properties [4]. Following the progress, with time, new designs, for example differential Helmholtz resonator, led to better signal enhancement and the work towards miniaturization of the photoacoustic cell has been started [5–7]. Nowadays, PAS is

well spread technique for toxic gas detection and able to provide sensitive and compact optical sensors for industrial applications.

Main principles of PAS are represented on Figure 5.1.

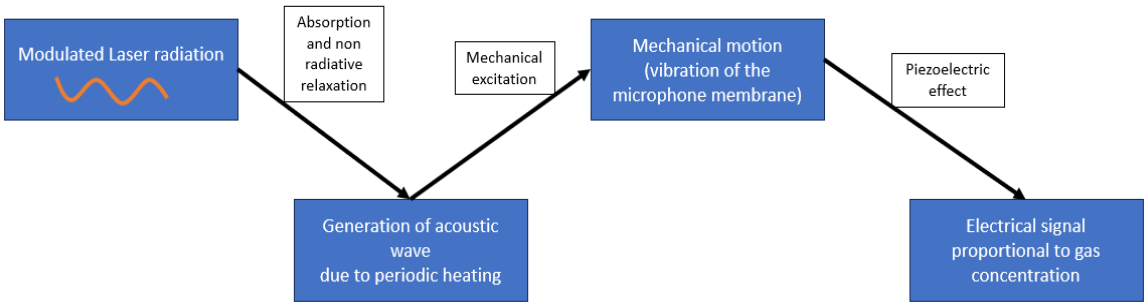


Figure 5.1. Schematic representation of main principals of PAS

When a material is exposed to modulated light (coming, for example, from a laser source), some of the photons are absorbed by the material if their energy matches the energy levels of electronic or vibrational transitions within the material. This absorbed energy excites the electrons or vibrational modes to higher energy levels. After absorbing energy, the excited electrons or vibrational modes can lose their excess energy through various processes, one of which is non-radiative relaxation. In this process, the excess energy is converted into heat rather than being re-emitted as light (radiation). As the material undergoes non-radiative relaxation, it experiences rapid, localized heating. This causes a rapid expansion of the material, followed by a contraction as it cools down. This periodic expansion and contraction result in the generation of acoustic waves. Acoustic waves generated within the material propagate as pressure waves, which can be detected using specialized microphones or transducers. The amplitude and phase of these acoustic signals are directly related to the intensity and phase of the absorbed modulated light. The detected acoustic signals are typically analyzed using signal processing techniques. By measuring the amplitude of the acoustic signal as a function of the modulation frequency (frequency of the

modulated light), a photoacoustic spectrum is obtained. This spectrum provides information about the absorption characteristics of the material at specific wavelengths. The photoacoustic spectrum can be also used for quantitative analysis, including the determination of the concentration of absorbing species in the material. By comparing experimental results with reference spectra, it is possible to identify the substances present in the sample.

Photoacoustic spectroscopy has numerous advantage:

1) Sensitivity: PAS is highly sensitive, capable of detecting even trace amounts of absorbing substances in a sample. This sensitivity makes it useful for the detection of low concentrations of gases, liquids, and solids.
2) Selectivity: PAS can provide selective information about specific absorbing species in a complex mixture. By tuning the light source to specific wavelengths, researchers can target different absorption lines, allowing for the selective analysis of individual components.
3) Non-Destructive: PAS is non-destructive to the sample being analyzed. Unlike some other analytical techniques that may alter or damage the sample during analysis, PAS does not cause chemical or physical changes to the material being studied.
4) Versatility: PAS can be applied to a wide range of materials, including gases, liquids, solids, and even biological tissues. It can be used in various environments and under different conditions.
5) Real-Time Monitoring: PAS can be used for real-time monitoring of dynamic processes. It can provide continuous data on changes in concentration or absorption properties over time, making it valuable in process control and monitoring applications.

6) Wide Spectral Range: PAS can be employed of a broad spectral range, from ultraviolet (UV) to infrared (IR), depending on the choice of the light source. This flexibility allows researchers to study a wide range of molecular and chemical species.
7) Minimal Sample Preparation: PAS often requires minimal sample preparation, reducing the time and effort needed to analyze samples. This makes it suitable for rapid screening and analysis.
8) Environmental Applications: PAS has been used in environmental monitoring to detect pollutants, greenhouse gases, and other contaminants in air and water. Its sensitivity and selectivity are particularly valuable in this context.
9) Biomedical Imaging: PAS has found applications in biomedical imaging, including the imaging of blood vessels, oxygen saturation, and tissue composition. Its non-ionizing nature and high sensitivity make it a safe and informative imaging modality.

Overall, the combination of all the features listed above, makes photoacoustic spectroscopy a powerful tool in various scientific disciplines, including chemistry, physics, environmental science, and biomedical research. Its applications continue to expand as researchers develop new techniques and instruments for specific uses.

Theoretical models of photoacoustic effect have been studied for years. The process of acoustic wave generation can be split into three main parts:

- absorption of incident photons following with excitation of the gas molecules
- generation of thermal and acoustic waves
- identification of the effect caused by photoinduction using an acoustic-electric transducer

Assuming a gas molecule is behaving as a two-level system, we can distinguish between two distinct energy states: the primary energy state (E_0) and the excited energy state (E_1), which are each associated with molecular densities $N_0(r,t)$ and $N_1(r,t)$, respectively. After optical absorption, the system can make a transition back to a lower energy state through two mechanisms: a radiative process involving either spontaneous or stimulated emission and a non-radiative process where energy is transferred via collisions with other molecules in the sample. If we name the Einstein coefficients for spontaneous and stimulated emission as A_{10} and B_{10}, respectively, and represent the non-radiative energy transfer rate as c_{10}, we can express the rate equation for the population of the excited state $N_1(r,t)$ as follows:

$$\frac{dN_1}{dt} = \rho_\vartheta B_{10}(N_o - N_1) - (A_{10} + c_{10})N_1 \qquad (5.1)$$

Where ρ_ϑ is the energy density of radiation. We can write down the lifetime of the excited state as follows:

$$\tau = \frac{1}{A_{10} + c_{10}} \qquad (5.2)$$

Supposing that a weak optical absorption ($N_1 \ll N_0$) take place and N_0 is time-independent, the equation 5.1 can be rewritten as follows:

$$\frac{dN_1}{dt} = \rho_\vartheta B_{10} N_o - \frac{N_1}{\tau} \qquad (5.3)$$

The term $\rho_v B_{10}$ denotes the rate at which optical absorption occurs, and it can be defined as the result of multiplying the photon flux by the absorption cross-section σ. When the incoming photon flux experiences periodic modulation at a frequency ω, it can be represented as follows:

$$F(r,t) = F_o(r)(1 + \delta e^{i\omega t}) \quad (5.4)$$

Putting together equation 3 and 4 we can solve the differential equation and retrieve the population density of the excited energy level as a function of the optical absorption of modulated light:

$$N_1(r,t) = \frac{N_0 \sigma F_o(r) \delta}{\sqrt{1+\omega^2\tau^2}} \tau e^{i(\omega\tau-\theta)} \quad (5.5)$$

where θ = arctan(ωt) is the phase difference between the modulation of photon flux and population density. The heat, which generate optical absorption can thus be connected to the population density in a way:

$$H(r,t) = \frac{N_1(r,t)h\nu}{\tau} = \frac{N_0 \sigma F_o(r) \delta h\nu}{\sqrt{1+\omega^2\tau^2}} e^{i(\omega\tau-\theta)} \quad (5.6)$$

In this model, where hν represents the energy of the absorbed photon ($h\nu = E_1 - E_0$), two key assumptions are made:

- The coefficient $F_0(r)\sigma$ is assumed to have low values to prevent absorption saturation and to disregard stimulated emission.
- The modulation frequency, denoted as ω, is required to be significantly smaller than $1/\tau$.

These conditions are typically met in Photoacoustic Spectroscopy (PAS) experiments, especially when dealing with low concentrations of absorbing gas and modulation frequencies in the kilohertz (kHz) range. The modulated heat transfer process is then transformed into acoustic waves. This transformation can be explained by considering the Navier–Stokes equations with slight

perturbations in thermodynamic parameters such as temperature (T), density (ρ), pressure (p), and linear velocity. These variations in thermodynamic parameters are assumed to be both local and small enough to disregard nonlinear effects. Under these assumptions, the Navier-Stokes equations can be derived in the form of a D'Alembert wave equation, which describes the propagation of the acoustic mode [8].

$$\nabla^2 \delta p(r,t) - \frac{1}{u^2}\frac{\partial^2 \delta p(r,t)}{\partial t^2} = -\frac{\gamma - 1}{u^2}\frac{\partial H}{\partial t} \qquad (5.7)$$

In this context, where 'u' represents the speed of sound in the gas sample, and 'γ' stands for the heat capacity ratio (where $\gamma = C_V/C_p$), the above equation can be solved using the Fourier transform technique, while also applying specific boundary conditions that restrict the propagation of acoustic waves to within the confines of the photoacoustic cell. Employing the Fourier transform operation leads to the following outcome:

$$\left(\nabla^2 + \frac{\omega^2}{u^2}\right)\partial p(r,\omega) = \frac{\gamma - 1}{u^2} i\omega H(r,\omega) \qquad (5.8)$$

The overall solution to this equation can be described as a combination of an infinite number of acoustic modes superimposed together:

$$\partial p(r,\omega) = \sum_j A_j(\omega)\partial p_j(r) \quad (5.9)$$

The general solution for this equation can be written as a combination of various acoustic modes, each represented by their respective amplitudes, $A_j(\omega)$, and governed by solutions $\delta p_j(r)$ associated with the homogeneous wave equation from Equation 5.9. These solutions, δp_j, need to satisfy a boundary condition that requires them to equal zero at the cell walls, as pressure waves exhibit nodal points at these locations.

In the context of Photoacoustic Spectroscopy (PAS), the gas is enclosed within an acoustic cell where optical absorption occurs. Consequently, the determination of the normal acoustic modes relies on the specific geometry of the acoustic cell, which, in turn, defines the applicable boundary conditions. Commonly used acoustic cell designs often feature a cylindrical shape. The excitation source typically consists of a narrow-diameter light beam aligned with the cylindrical axis. Local pressure waves propagate radially outward, perpendicular to the direction of the incident light beam. When a standing-wave vibrational pattern is established, the acoustic cell functions as an acoustic resonator, amplifying the acoustic power at the resonance frequency.

The extent of this amplification in an acoustic cell is quantified by a parameter called the Q-factor (Q). The Q-factor is essentially the reciprocal of losses, serving as a measure of how much energy is retained within the resonator relative to the energy dissipated in one cycle. Another common representation of the Q-factor is as the ratio between the resonance frequency (ω_j) and the full-width half-maximum (FWHM) ($\Delta\omega_j$) of the resonance profile.

$$Q_i = \frac{\omega_j}{\Delta\omega_j} \qquad (5.10)$$

The amplitude of the jth mode corresponding to the resonance frequency ω_j is proportional to

$$A_j(\omega_j) \propto \frac{\gamma - 1}{\omega_j V_o} \alpha P_o L Q_j \qquad (5.11)$$

So, we have the absorption coefficient represented as α, the optical power of the excitation source denoted as P_0, the interaction length as L, and the cell volume as V_0. Typical Photoacoustic Spectroscopy (PAS) cells are characterized by resonance frequencies typically in the range of a few kilohertz, and their Q-factors are typically on the order of approximately 100.

To capture the acoustic signals within these cells, a microphone is usually positioned at the antinode point of one of the eigenmodes of the acoustic cell. This microphone serves as an acoustic transducer, converting the sound waves into an electrical signal. This electrical signal, labelled as S, can be expressed as follows:

$$S = R_m \delta p(r_m, \omega) \qquad (5.12)$$

where R_m is the microphone responsivity and $\delta p(r_m, \omega)$ is the amplitude of the pressure wave in the microphone position. Putting Eq. 5.11 in Eq. 5.12, the electric signal can be then articulated as:

$$S = R_m \frac{\gamma - 1}{\omega_j V_o} \alpha P_o L Q_j \delta p_j(r_m, \omega) = C_m \alpha P_o \qquad (5.13)$$

The term "C_m" is referred to as the cell constant, and it varies based on the characteristics of the mechanical resonator (such as its volume, Q-factor, interaction length), the operating frequency, as well as the microphone's responsivity and placement. Given that the absorption coefficient α can be calculated in following way:

$$\alpha(\lambda) = NC\sigma(\lambda) \qquad (5.14)$$

the final expression of the Photoacoustic Spectroscopy (PAS) signal can be summarized as follows:

$$S = C_m \sigma N P_o c \qquad (5.15)$$

Hence, the electrical signal produced by the microphone exhibits a direct linear correlation with the gas concentration, enabling a precise quantitative analysis of chemical substances.

5.2 QEPAS. Theory and state of the art

Quartz enhanced photoacoustic spectroscopy is a highly sensitive and selective analytical technique used to detect and quantify trace amounts of specific gas species in various samples. It combines the principles of photoacoustic spectroscopy with the use of QTF (Quartz tuning fork) instead of microphone. QTF is a small, highly sensitive mechanical resonator made of a thin, single-crystal quartz crystal. It is shaped like a two-pronged fork, and when it is mechanically stimulated or perturbed, it vibrates at a specific, well-defined mechanical resonance frequency. First, only commercially available QTF (which were used in the clocks) were used, which is characterized by a resonance frequency of 32768 Hz and a Q-factor ~100000 (under vacuum). Schematic representation of the main principle of QEPAS and QTF shape can be found on Fig. 5.2.

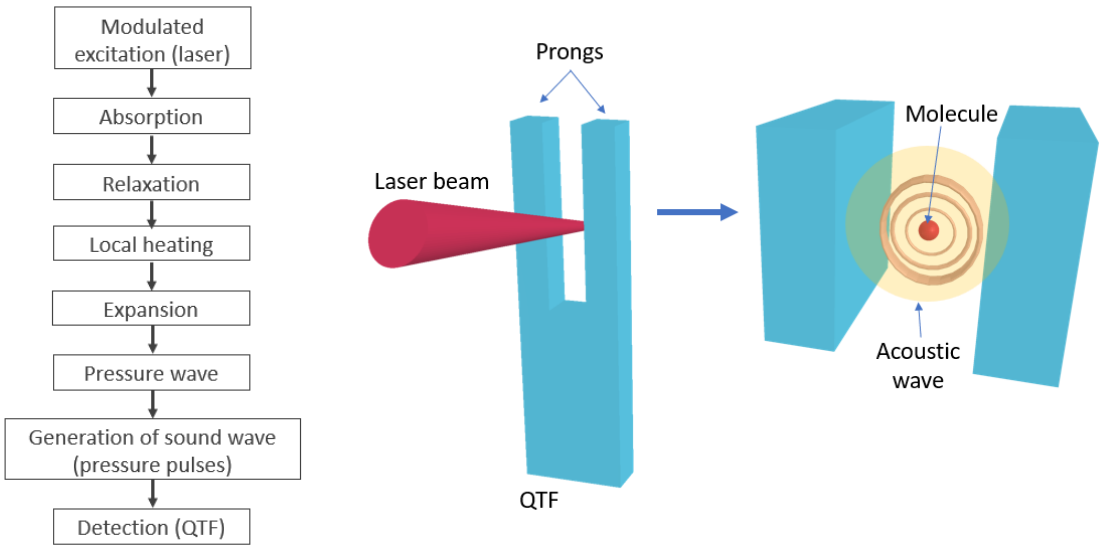


Figure 5.2. Schematic representation QEPAS principal and QTF shape

In essence, the light source, often a laser emitting at a specific wavelength, gets focused between the two prongs of QTF and is absorbed by the gas sample. Subsequently, the excited molecules

return to their ground state through non-radiative processes. These non-radiative processes lead to localized heating in the gas, causing an increase in local pressure. When the intensity of the light source is modulated (normally at the associated resonance frequency of QTF or at one of its subharmonics), it creates periodic thermal energy fluctuations in the sample, resulting in the formation of pressure waves, or in simpler terms, sound waves, with the same frequency as the light modulation. Quartz possesses piezoelectric properties, which means that when the sound wave generated between its two prongs causes an antisymmetric vibration of the prong within the Quartz Tuning Fork (QTF) plane, electrical charges are generated. These charges are directly proportional to the intensity of the sound wave. The signal in Quartz-Enhanced Photoacoustic Spectroscopy (QEPAS) exhibits a linear relationship with the absorption coefficient. This absorption coefficient is derived from the optical cross-section, multiplied by the gas concentration and the total number of molecules in the volume. Consequently, the QEPAS signal linearly correlates with the gas concentration. Typically, the Quartz Tuning Fork (QTF) is coupled with a micro-resonator, which can take the form of a single tube with a hole in the middle (off-beam) or two tubes (on-beam). This micro-resonator acts as an organ pipe resonator, facilitating the probing of the sound wave.

QEPAS provides the same advantages as PAS but is able to reach better sensitivity, with limit of detection of several toxic gases in part per billion or in part per trillion ranges [9]. It also should be mentioned that unlike PAS, QEPAS is insensitive to the background noises. A Quartz Tuning Fork (QTF) operates as an acoustic quadrupole resonator with a relatively narrow bandwidth of a few Hertz or less when operated at atmospheric pressure. Consequently, only a limited number of frequency components within this narrow spectral range can efficiently excite vibrations in the QTF. There are a couple of key reasons why the surrounding ambient noise spectrum has a limited

impact on the Quartz-Enhanced Photoacoustic Spectroscopy (QEPAS) signal. First of them is that typical ambient noise frequencies are generally below 10 kHz, and since the QTF has a bandwidth well above this range, only a small portion of the environmental noise falls within the QTF's bandwidth. Therefore, it has a reduced effect on the QEPAS signal. Second reason is that sound waves in air at a frequency of 32 kHz have a corresponding acoustic wavelength of approximately 1 cm. In the case of external acoustic sources, these waves would exert force in the same direction on the two prongs of the QTF, i.e., the two prongs face the same wavefront, given that the prongs are spaced less than 1 mm apart. This results in an in-plane symmetric vibration mode (as shown in Fig. 5.3) that lacks piezoelectric activity. Conversely, when the acoustic wave source is positioned between the two prongs, it induces an in-plane antisymmetric vibration mode (as illustrated in Fig.5.3) that is piezoelectrically active.

The production of photoacoustic waves entails the conversion of energy from internal molecular states to translational molecular motion. In simpler terms, when a rotational-vibrational state is

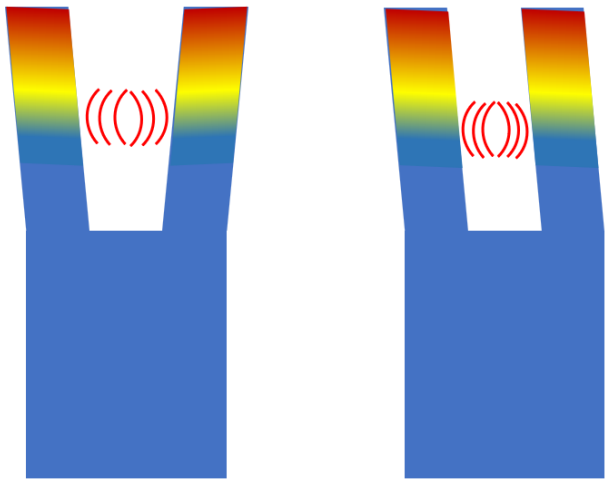


Figure 5.3. Representation of QTF symmetric and antisymmetric vibrations

excited, it is followed by a collision-induced process known as vibrational-to-translation (V-T)

relaxation. This process is characterized by a time constant, referred to as the relaxation time, which depends on the properties of the surrounding molecules and their interactions with each other.

For gas sensing applications, Quartz Tuning Forks (QTFs) operating < 35 KHz frequency range are typically used. This choice is based on the fact that energy transfer processes in gases occur on a microsecond (μs) timescale, and the Photoacoustic Spectroscopy (PAS) signal diminishes at higher frequencies [10]. In Quartz-Enhanced Photoacoustic Spectroscopy (QEPAS), laser modulation frequencies are employed that match one of the flexural modes of the QTF or its subharmonics. These vibration modes generally have higher frequencies than the conventional acoustic modes of PAS gas cells (where $f_0 < 4$ kHz).

When the V-T relaxation process is significantly slower than the modulation frequency, the thermal waves in the gas cannot effectively track the rapid changes induced by the laser-driven molecular vibration excitation. As a result, the generated photoacoustic waves are weaker compared to scenarios where V-T energy equilibration occurs more rapidly [11].

Using Equation 5.13 as a starting point, the photoacoustic signal S can be expressed as follows [12]:

$$S = \frac{P_o Q \alpha}{\sqrt{1+(\frac{2\pi f_o \tau V-T}{P})^2}} = Q\alpha\varepsilon P_o \quad (5.16)$$

5.3 QEPAS twin - sensors for Methane and Nitrious oxide detection

Nitrous oxide (N_2O) and methane (CH_4) are two potent greenhouse gases that, while naturally occurring, have been significantly augmented in the atmosphere due to human activities. N_2O,

often known as "laughing gas," is a byproduct of various agricultural and industrial processes, primarily arising from the use of synthetic fertilizers and combustion-related activities. N_2O, when released into the atmosphere, becomes a potent contributor to global warming, making it a critical target for emissions reduction efforts. On other hand CH_4, commonly referred to as methane, is a fundamental component of natural gas and is released during fossil fuel extraction, distribution, and utilization. Furthermore, CH_4 emissions result from agricultural practices, including enteric fermentation in livestock and the decomposition of organic matter in landfills. Methane is not only a potent greenhouse gas but also highly flammable and explosive in certain concentrations, posing serious safety risks in confined spaces. The imperative to detect N_2O and CH_4 lies in their adverse environmental and health effects. Elevated levels of these gases contribute to climate change, intensifying global warming and its associated consequences, such as extreme weather events, sea-level rise, and disruptions in ecosystems. Additionally, exposure to high concentrations of N_2O or CH_4 can lead to adverse health effects in humans, including asphyxiation and respiratory distress.

The aim of the current work was developing sensitive reliable sensor for detection of both gases. The objection was to manufacture 2 twin-sensors for CH_4 and NO_2 detection, proving repeatability of QEPAS sensor behavior and showing the possibility of simultaneous detection of both gases by the same sensor head. Both sensor's had equal set ups, light sources and type of measurements as QTF and laser characterizations, pressure tests, QEPAS acquisitions of different concentrations of gases and 24h gas sensing in laboratory conditions. Each sensor-head contains the laser source and acoustic detection module (ADM) composed by a custom t-shape quartz tuning fork coupled with a pair of acoustic resonator tubes (length of 12.4 mm and an inner diameter of 1.59 mm). Custom QTF dimensions (spacing between prongs 0.8 mm) allow easier focusing of the laser beam leading to better alignment. Both sensor-heads target two adjacent but not superimposed spectral lines of

CH_4 and N_2O centered at 1275.04 cm^{-1} and 1275.49 cm^{-1} respectively. The ADM represents itself vacuum-tight gas cell equipped with two windows and in/out gas connectors.

In realised sensors laser sources from Thorlabs (QD7840HHLH-A Mid-IR Quantum Cascade lasers) were used emitting at 7,840 µm. Lasers were packed into butterfly packaging and their LIV characterisation was realised and shown on Fig 5.4. Laser for Sensor Head 1 had Ith=125 mA and reached a power up to 90 mW. This laser was reaching the absorption line of CH_4 at 239 mA (output power of 82 mW) and absorption line of N_2O at 262 mA (output power of 81 mW). Laser source for Sensor head number 2 had higher Ith of 150 mA and lower output power reaching 80 mW at maximum current. CH_4 peak can be reached at 319 mA (power of 74 mW) and N_2O could be detected with locked current at 340 mA (power of 76 mW). Characterisation curved for both

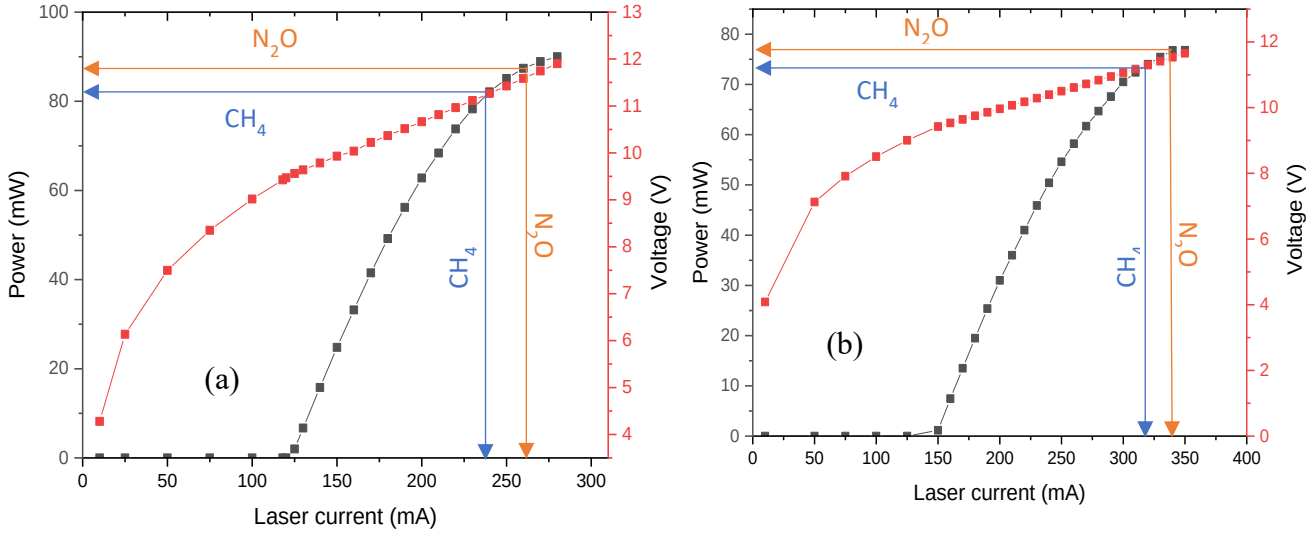


Figure 5.4. (a) - LIV curve for the laser installed in Sensor Head 1; (b) - LIV curve for laser source of Sensor Head 2

lasers can be seen on the Figure 5.4. Presented QCLs were fixed at operation temperature of 20°C.

Characterisation of custom QTF with and without acoustic micro resonator tubes assembled in on-beam configuration were done under 780 Torr, under 500 Torr it was characterised only with micro

resonators. Schematic representation of the characterisation set up and of contacts map of ADM are shown on Figure 5.5 (a) and Fig. 5.5 (b) respectively.

A Tektronix model AFG3102 function generator, capable of providing a sinusoidal voltage with a modulation frequency resolution as fine as 2 millihertz (mHz), is employed to supply the QTF with a sinusoidal voltage. The electrical current generated by the QTF undergoes conversion into

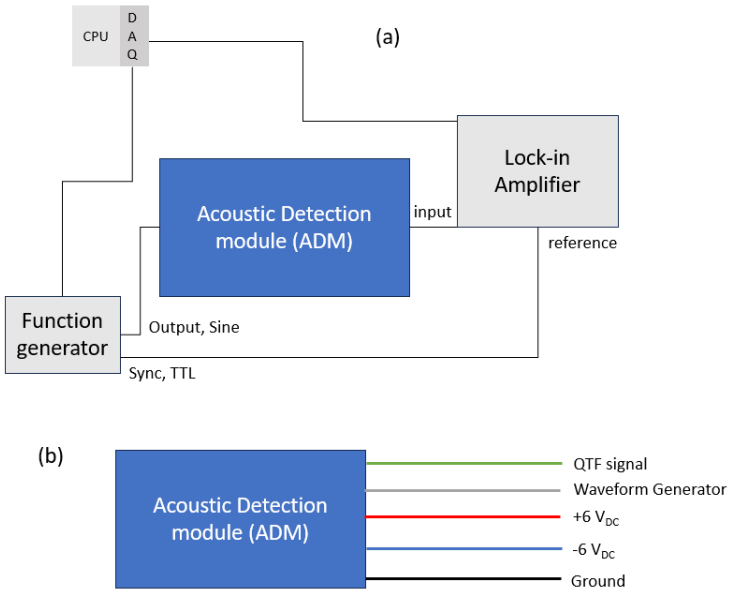


Figure 5.5. (a) - Diagram illustrating the setup for QTF characterization; (b) - depiction of the pinout configuration of the transimpedance amplifier, showing its placement on the underside of the ADM

a voltage signal via a transimpedance amplifier. This voltage output is then measured using a lock-in amplifier, specifically the EG&G Instruments 7265 Dual Phase DSP Signal Recovery Lock-in Amplifier. To investigate the resonance properties of the QTFs, a sinusoidal voltage signal is fed to the QTF via the function generator. The modulation frequency is systematically varied across the expected resonance frequency range.

The data acquired from the QTF is processed by the lock-in amplifier through a data acquisition card (DAQ NI USB-6361) and is subsequently recorded by a laptop computer (CPU). Obtained characterisation curves of QTFs at atmospheric pressure are presented on figure 5.6 for both sensor heads.

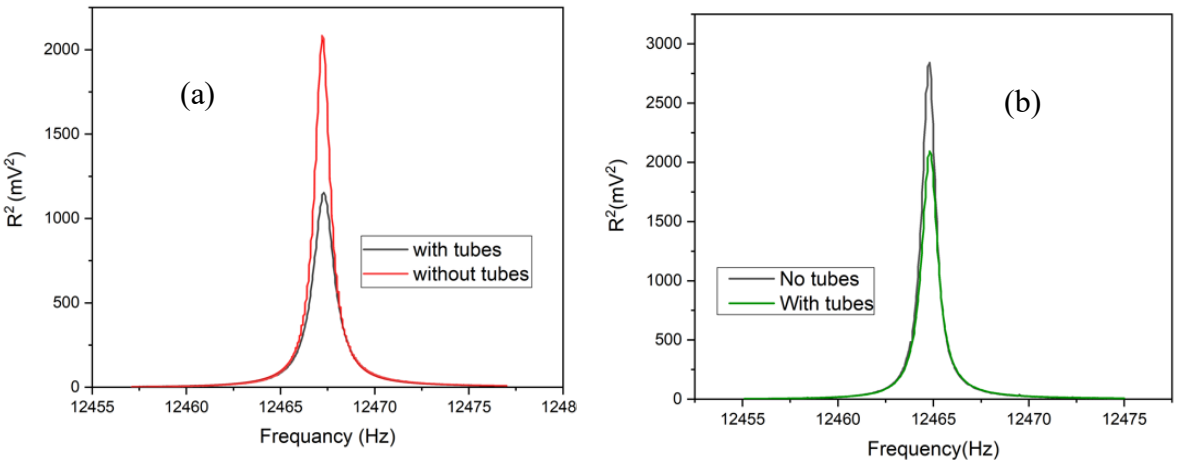


Figure 5.6. Characterisation at atmospheric pressure of T-shape QTF with and without tubes for: (a) - sensor head 1; (b) - sensor head 2

Sensor head	780 Torr				500 Torr	
	With tubes		No tubes		With tubes	
	f_o (Hz)	Q	f_o(Hz)	Q	Fo(Hz)	Q
1	12 467,3	9 183	12 467,2	12 398	12 467,6	12 337
2	12 464,8	12 346	12 464,7	14 444	12 465	15 910

Table 5.1. Characterisation results of custom QTF under different pressure

The spectrophone resonance curves are fitted by using a Lorentzian function to determine the resonance frequency f and the full width at half-maximum value (FWHM). Quality factor is estimated by dividing resonance frequency by FWHM. Table 5.1 shows data for all the

characterisation and can be seen that resonance frequency of the spectrophone is around 12 kHz and quality factor (Q) is going up to almost 16 000 with tubes at lower pressure.

It can be seen that Q is decreased with introduction of resonator tubes into the system and increases if lowering the pressure.

After characterisation of QTFs and laser sources the QEPAS set up was realized, schematic representation of which can be seen on Fig. 5.7. Photo of used senor head is shown on Fig. 5.8. First, acoustic detection module (which consists of QTF and micro resonators) is connected to lock-in amplifier. The sensor head is composed by the laser source, a lens for optical alignment,

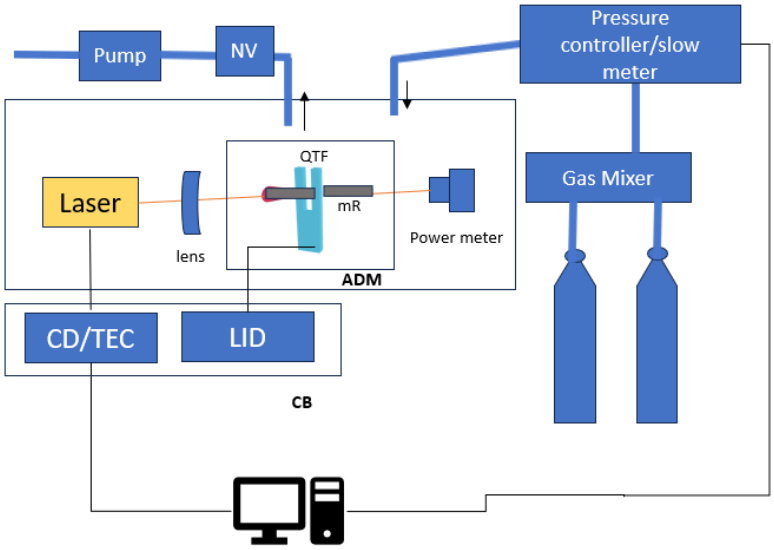


Figure 5.7. Schematic representation of QEPAS setup.

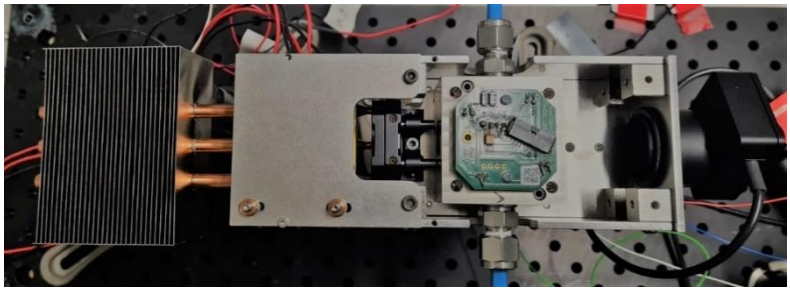


Figure 5.8. Photo of the used Sensor Head in QEPAS setup.

the ADM and a power meter used for alignment purpose and to control the laser power. Nafion humidifier (PDMSXA-100) was used to keep stable the water concentration and had following dimensions: 16 cm of module length, 2.86 cm of module diameter and 1000 cm^2 of membrane area. In below experiments the air flowrate was set to 50 sccm, same as N_2 counter flowrate.

The laser is controlled by current driver and temperature controller. Lock-in amplifier is than connected to function generator from one side and to data acquisition card and computer from another side. Function generator is connected to the current driver and gas was flowing in the ADM throw the tubes using gas dilution system and pressure controller. QEPAS measurements are conducted using both wavelength modulation and 2f-detection (WM-2f) independently. For each sensor head, the laser's sinusoidal modulation frequency is set to half of the resonance frequency of its corresponding spectrophone. Simultaneously, the response of the Quartz Tuning Fork (QTF) is demodulated at its resonance frequency using a lock-in amplifier. To perform QEPAS spectral scans, the emission wavelength is adjusted by gradually ramping the current applied to the laser. This approach ensures that the desired absorption features are fully captured and recovered.

After building up the setup, including gas line, modulation part and sensor head, test for detection of first gas (CH_4) has been started on Sensor Head Number 2. First, we had to determine the optimal working pressure. Differences in QEPAS signal-pressure trends can be mainly ascribed to different no-radiative relaxation rates of different gases, which affecting the efficiency of the acoustic wave generation [13]. We did a pressure test acquiring QEPAS signals of chosen

absorption lines under different pressure (from 100 Torr to 700 Torr) and comparing QEPAS signal pick's values.

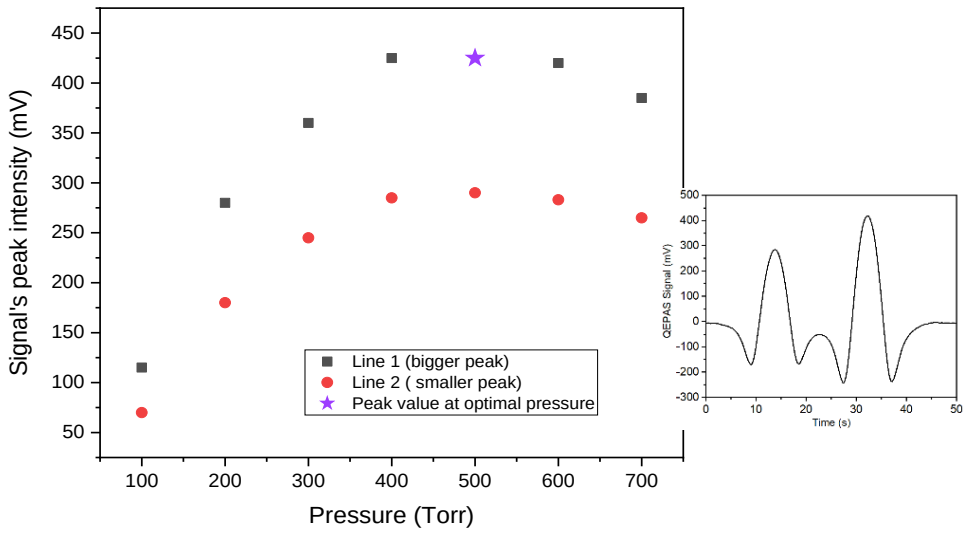


Figure 5.9. QEPAS scan of CH_4 absorption lines at 500 Torr and signal's peak intensity at different operating pressures.

For each gas pressure, the peak-to peak amplitude as well as modulation frequency were adjusted to maximize the peak value of the QEPAS scan. The results of the test are presented on the Figure 5.9. Same pressure test was conducted for N_2O, and results can be observed on Figure 5.10. Even if the optimal pressure for N_2O appears to be 300 Torr, we decide to work at 500 Torr, choosing the optimal pressure for CH_4, although losing a bit in performance for N_2O detection.

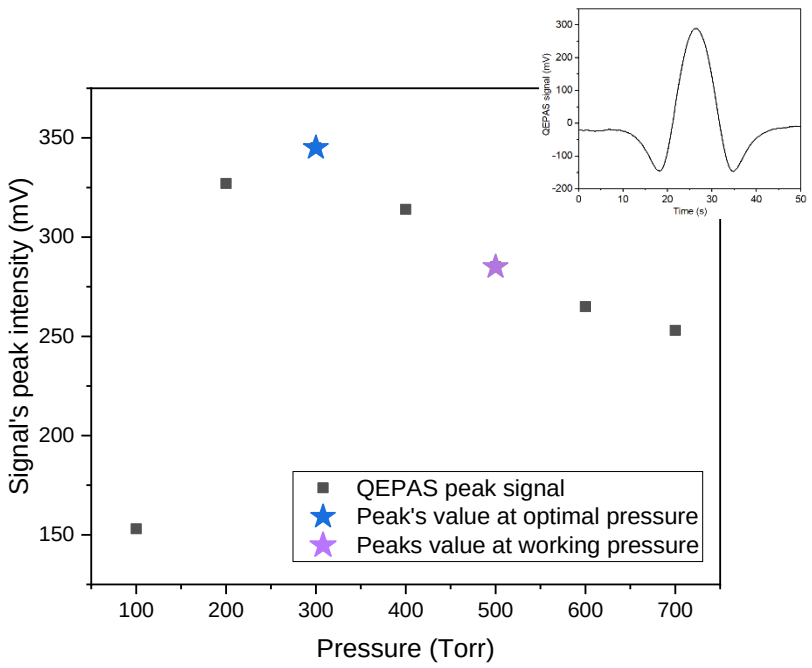


Figure 5.10. QEPAS scan of N_2O absorption lines at 500 Torr and signal's peak intensity at different pressures.

After selecting the operating pressure for both gases (500 Torr) and temperature operation (20ºC), we acquired at first QEPAS signals using gas mixtures with different concentrations of methane and observed a good linearity of the signal. The gas mixtures are produced using an MCQ Instrument (Gas Blender GB1A30120164,) which also controls the total gas flow rate within the gas line, maintaining it at a constant 50 sccm. To calibrate the sensor for methane detection, a cylinder containing a certified concentration of 50 ppm of CH_4 in pure N_2 was employed. This cylinder was used to create various mixtures with reduced CH_4 concentrations by diluting it with pure N_2 from a separate cylinder. Figure 5.12 (a) shows the QEPAS signal of different concentrations of CH_4 and Figure 5.12 (b) present the obtained calibration curve (linearly fitting the peak values as a function of the analyte concentration). As can be seen on Fig. 5.12 (a), in the specific spectral range there are two neighbouring but non-interfering absorption lines of CH_4, the calibration curve was obtained both for more intense peak and for the less intense one. We also

perform step wise measurements keeping the laser locked on the strongest absorption peak. Linearity of the step wise measurements can be noticed as well. For sensing purposes employing the more intense absorption line is preferable, due to its larger calibration curve slope, resulting 9.39 mV/ppm.

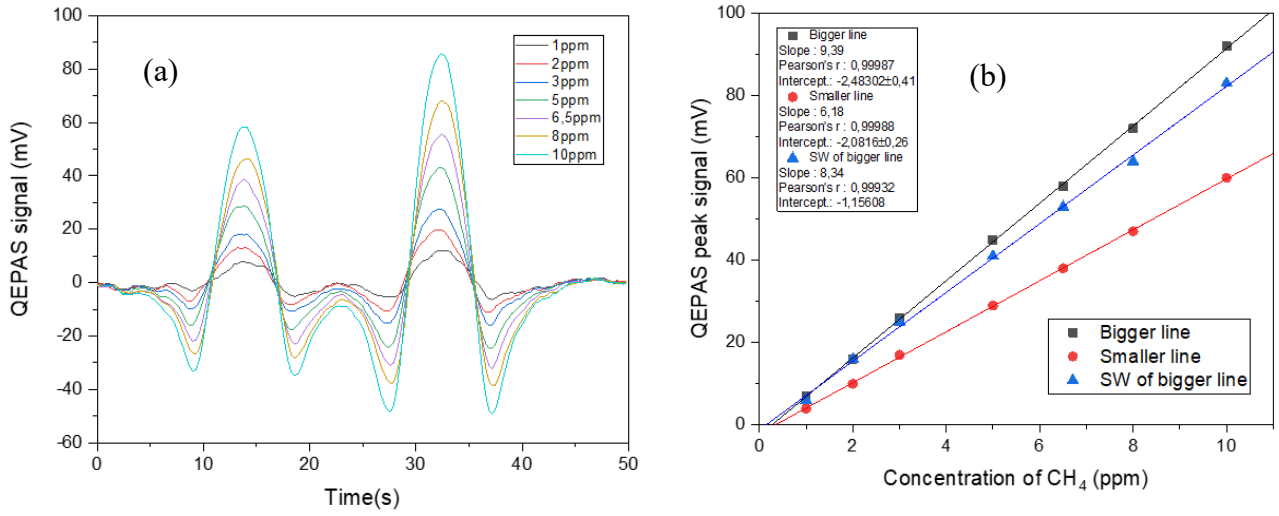


Figure 5.11. (a) - QEPAS signal for different concentration of CH_4; (b) - calibration curve for CH_4

Using the same sensor head with the same laser source and QTF we performed QEPAS measurements for different concentration of N_2O (Figure 5.12 (a)). For nitrogen dioxide

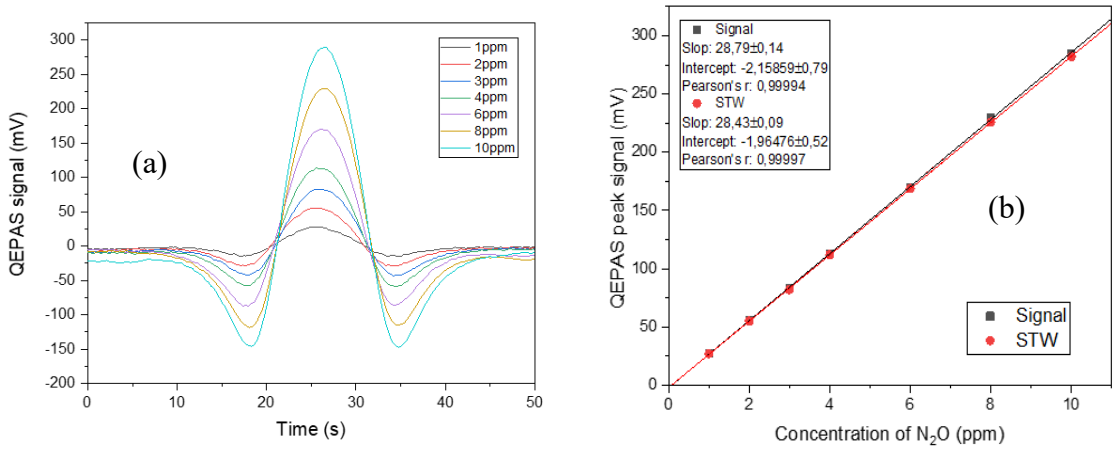


Figure 5.12. (a) - QEPAS signal for different concentration of CH_4; (b) - calibration curve for CH_4

calibration, a cylinder with a certified concentration of 10 ppm of N_2O in pure N_2 was used. Calibration curve is presented on Fig. 5-12(b) and the slope of the calibration cure results 28.79 mV/ppm. Both gases did undergo the stability test, measurements for CH_4 and N_2O were

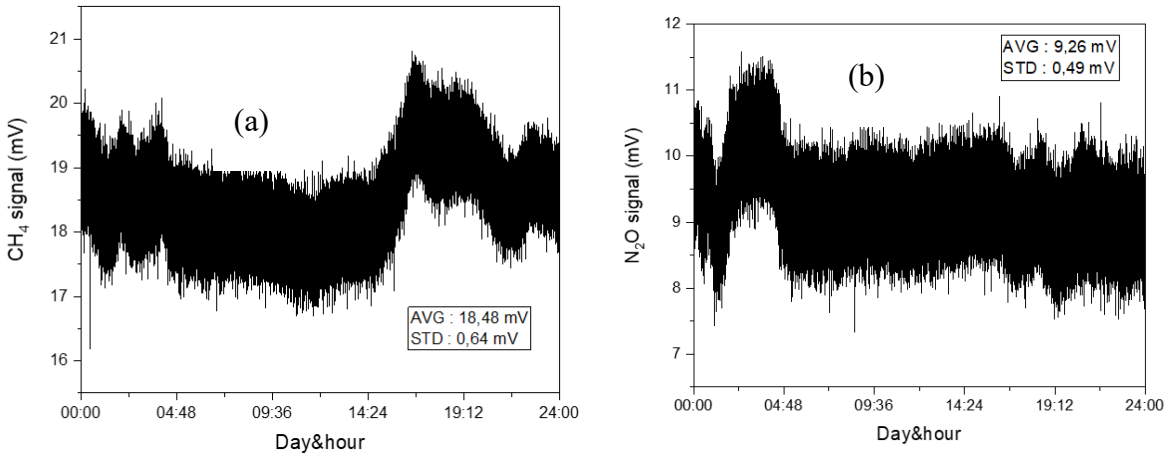


Figure 5.13. (a) - CH_4 signal in the laboratory condition within 24h; (b) – N_2O signal in the laboratory condition within 24h

successfully performed separately in the laboratory conditions during 24 h (Fig. 5.13). Such noisy signal is explained by the custom configuration of the fan for laser cooling.

To analyse the long term stability of the sensor, we conducted an Allan-Werle deviation analysis to estimate the 1σ noise level (and consequently, the attainable Minimum Detectable Limit or MDL) in relation to the integration time. During this analysis, the laser was frequency-locked well away from any absorption features, and standard air was flowing through sensor head. The resulting Allan-Werle deviation plot is displayed in Figure 5.14. Minimum detection limits for both gases considering different integration times can be found in Table 5.2.

After both gases were successfully detected separately using Sensor Head Number 2 giving MDL of 6.4 ppb (CH4) and 2 ppb (N2O), the next step was to oerform all the same measurements and calibration for both gases using Sensor Head Number 1.

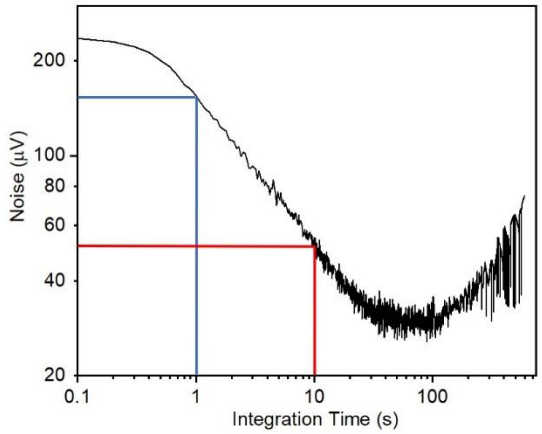


Figure 5.14. Allan-Werle deviation plot of the QEPAS signal as a function of the integration time.

MDL calculations		CH_4		N_2O	
Int time (s)	Noise (mV)	Slope (mV/ ppm)	MDL (ppb)	Slope (mV/ ppm)	MDL (ppb)
0,1	235,79	8,56	27,5	27,37	8,6
1	154,99	8,56	18,1	27,37	5,6
10	54,7	8,56	6,4	27,37	2

Table 5.2. MDL for CH_4 and N_2O at different integration time.

Comparison of results for both Sensor Heads is represented in the Table 5.3. From results it can be clearly seen, that even since Sensor Heads have slight difference performance in laser power and QTF characteristics, the linearity and MDL is very similar, slightly better for sensor head number 1.

	Sensor Head 1	Sensor Head 2
Working T(°)	15°	20°
Working Pressure	500 Torr	500 Torr
Locked current	CH_4 - 239 mA N_2O - 262mA	CH_4 - 319 mA N_2O - 340 mA
Laser power at locked current	CH_4 - 82 mW N_2O - 87,7 mW	CH_4 - 74 mW N_2O - 76,78 mW
Resonance Frequency	12 467,6 Hz	12 465 Hz
Q Factor	12 337	15 910
Slope	CH_4 - 8,56 mV/ppm N_2O - 27,37mV/ppm	CH_4 - 9,39 mV/ppm N_2O - 28,79 mV/ppm
Noise at 10 s int. time	54,7 µV	53,7 µV
MDL at 10 s int. time	CH_4 – 6,4 ppb N_2O - 2 ppb	CH_4 - 5,7 ppb N_2O - 1,8 ppb

Table 5.3. Summarized results on gas sensing of CH_4 and N_2O for both tested Sensor Heads

As both gases could be detected tuning the same laser source separately, the next logical step was trying to detect them sequentially using one of the sensor heads. The tested was conducted creating different gas mixtures: at first we fixed concentration of CH_4 at 2 ppm and varied the concentration of N_2O from 300 ppb to 1000 ppb (Fig.5.15 (a)). It could be observed that peak of CH_4 remained stable without any alterations while N_2O peaks decreased linearly with concentration. In a similar way, we perform measurements keeping constant the N_2O concentration set at 600 parts per billion (ppb) and change the CH_4 concentration. The spectral scans are illustrated in Figure 5.15 (b), where CH_4 peak was decreasing proportionally with decrease of concentration. But in this context, a minor CH_4 peak exhibited an undesirable overlap with the N_2O signal, indicating susceptibility to variations in N_2O concentration, rendering it unsuitable for accurate detection. Conversely, the highest methane peak demonstrated stability without overlaps with N_2O absorption line and consistency in both the previous and current experiments, displaying sensitivity to concentration

changes. Consequently, our findings substantiate the feasibility of concurrent detection of both gases employing a singular sensor apparatus.

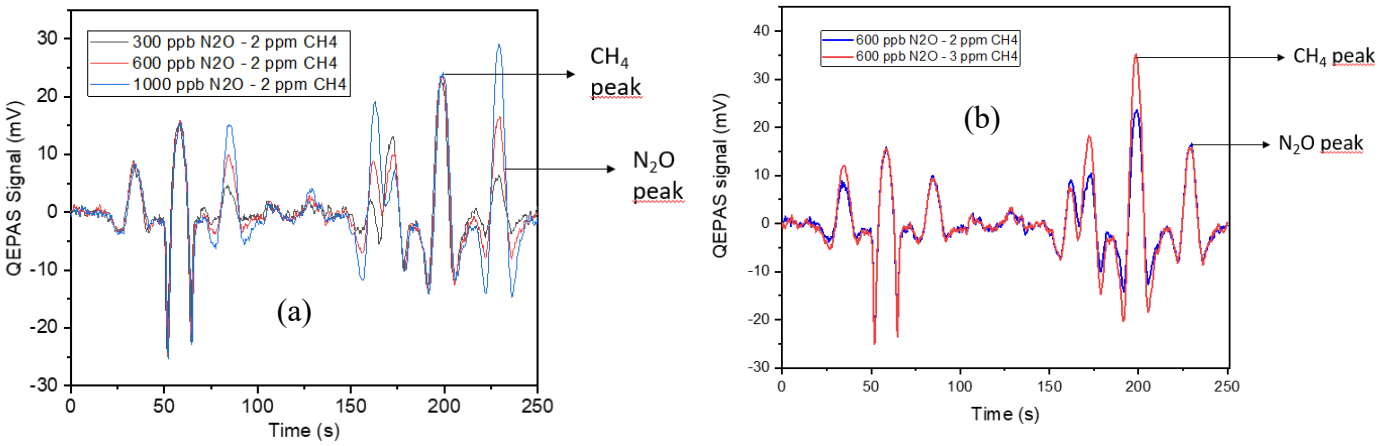


Figure 5.15. QEPAS signal of Gas mixture, where: (a) - concentration of CH_4 was fixed altering the concentration of N_2O; (b) - fixed concentration of N_2O while changing concentration of CH_4.

Hence, our investigation provides compelling evidence of the feasibility of concurrent detection of methane (CH_4) and nitrous oxide (N_2O) within the specified spectral range employing the same laser source. While it is imperative to acknowledge the need for further in-depth exploration in this domain, the present experimental iteration has showcased remarkable promise in terms of its potential for advancement.

Coming to conclusion all the results above proved that detection of CH_4 and N_2O using laser source emitting at 7.8 μm allows not only low detection limits and high sensitivity while detecting them separately, but also open the good potential for sequencially detection of both gases. Furthermore, our successful fabrication of equivalent Quartz-Enhanced Photoacoustic Spectroscopy (QEPAS) sensors equipped with two sensor heads reaffirms the stability and reliability of this approach, suggesting its scalability for larger-scale production.

5.4 QEPAS sensor for ammonia detection

Ammonia (NH3) is a toxic gas commonly encountered in various industrial, agricultural, and domestic settings. Its toxicity poses significant risks to human health and the environment, necessitating the development and implementation of effective detection methods. Ammonia is a colourless gas with a pungent smell, and its toxic properties arise from its alkaline nature, which can lead to severe respiratory and ocular irritation when exposed to even relatively low concentrations. Prolonged or high-level exposure can result in more serious health effects, including respiratory distress, chemical burns, and, in extreme cases, fatality. The importance of detecting ammonia gas lies in its ubiquitous presence in industrial processes such as refrigeration, agriculture (as a fertilizer), and manufacturing. Accidental releases, leaks, or overexposure incidents can occur, posing immediate dangers to workers, nearby residents, and the environment. Additionally, ammonia emissions can contribute to air pollution, water contamination, and ecosystem damage. Detection of extremely low concentrations of ammonia in human breath can lead to faster detection of serious disease, such as kidney and liver failure [14,15].

Development of QEPAS sensor for ammonia detection started with the determination of which absorption line to target, hence which laser source could be suitable for sensitive detection. The HITRAN database simulations for NH_3 at different spectral range were performed and literature study was done. In the end, the industrial available QCL (Thorlabs QD9062HHLH-C), emitting gat 9.062 μm and capable to target the absorption line of NH_3 positioned at 1103.44 cm^{-1}, with a line strength of $1.51 \cdot 10^{-19}$ cm/molecule [16], was chosen. The QCL was mounted in similar sensor head structure showed on Fig 5.8 and the NH_3 line can be targeted with an injection current of 320 mA corresponding to a laser power of 59 mW. QTF characterisation at atmospheric pressure was done implementing a similar set up as in previous experiment (Fig. 5.5(a)) and a similar ADM

(Fig.5.5(b)). The results for the custom t-shape QTF implemented for ammonia sensing is presented on Fig.5.16, showing at atmospheric pressure a resonance frequency after on-beam micro resonators alignment of 12 458,59 Hz and a Quality factor of 12 117.

Pressure study first on QTF performance was conducted between 300 Torr and 760 Torr. With decrease of pressure the resonance frequency and quality factor showed same trend (Table 5.4). Needs to be mentioned that operation method and QEPAS setup used for current ammonia sensor

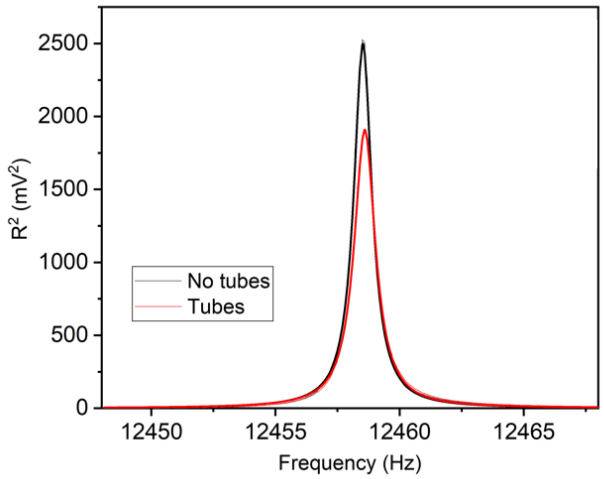


Figure 5.16. QTF characterization with/without tubes at atmospheric pressure.

QTF - pressure	f_o, Hz	Δf	Q
QTF – 100 Torr	12459,36	0,37	33765,2
QTF – 200 Torr	12459,22	0,51	24585,1
QTF – 300 Torr	12459,11	0,61	20440,2
QTF – 400 Torr	12459	0,7	17856,2
QTF – 500 Torr	12458,9	0,78	15974,8
QTF – 600 Torr	12458,81	0,86	14503,7
QTF – 700 Torr	12458,72	0,94	13241,8
QTF – 760 Torr	12458,65	1,01	12395,7

Table 5.4. Results of QTF characterisation operating at different pressures.

development is identical to QEPAS set up used in previous section of N_2O and CH_4 detection (Fig.5.7). First step of this was conducting pressure test for ammonia. A gas mixer (MCQ

Instrument Gas Blender GB1A30120164) whose output was connected to the input valve of the sensor box, a pressure controller/flow meter (MKS Type 649), a needle valve; and a vacuum pump (KNF N 813.4) were used to stabilize the pressure and fix the gas flow at 50 sccm through the gas line.

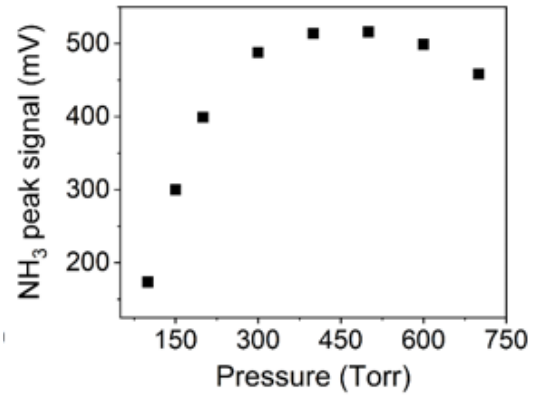


Figure 5.17. Pressure test for Ammonia detection.

The amplitude and the frequency of sinusoidal modulation were optimized for each pressure value and certified concentrations in nitrogen matrix were flowed in the gas line. For a 14 ppm of NH_3 diluted in N_2, the sensor head response showed its maximum value at 500 Torr, and all the parameters for the gas sensor have been set to such pressure value.

Calibration of the sensor for ammonia detection is very complicated process requiring detailed investigation. During the transportation of a gas through a tube or cell, there is a notable occurrence of adsorption effects, particularly when dealing with polar molecules such as ammonia and water. These effects, whether adsorption or desorption, lead to alterations in the concentration of the gas. Polar molecules like NH_3, characterized by substantial and enduring dipole moments, exhibit a strong inclination to adhere to surfaces. The dynamics of adsorption/desorption hinge on both the inherent characteristics of the inner surface (comprising material composition, temperature, and porosity) and the specifics of the experimental conditions (comprising gas flow rates and analyte

concentrations) [17]. The internal surfaces of a sensor and the tubing can be conceived as sites available for NH_3 molecules to bind and as reservoirs of these molecules. Consequently, it is imperative to account for adsorption and desorption processes when seeking to accurately determine the concentration of ammonia.

While a gas mixture pass through the sensor, it attains an equilibrium state in which the surface coverage and the concentration of molecules in the gas phase reach a balance. Consequently, when a gas with a known concentration is passed through a cell, the adsorption phenomenon can be quantified in terms of the time required to achieve a stable concentration level. Conversely, during the removal of a gas species from the gas conduit, molecules released from the reservoir augment the number of molecules in the gas mixture, signifying a desorption process. In both scenarios, the dynamics of adsorption and desorption can compromise the precision of gas detection techniques.

The dynamic equilibrium characterizing adsorption and desorption processes can be theoretically described through a qualitative model that considers time and spatial derivatives of NH_3 concentration and surface coverage, where surface coverage signifies the quantity of particles per unit area [18, 19].

$$\frac{\partial c_g(x,t)}{\partial t} = -u\frac{\partial c_g(x,t)}{\partial x} - \frac{dS}{dV}\frac{\partial c_w(x,t)}{\partial t} \quad (5.16)$$

In this context, we denote 'c_g' as the concentration of ammonia within the gas mixture, 'c_w' as the extent of ammonia coverage on the surface, 'dS' as the infinitesimally small surface area, 'dV' as the infinitesimally small volume, 'u' as the velocity at which the gas mixture is moving, which can be represented as the quotient of the flow velocity Φ and the cross-sectional area A, and 'x' represents the direction of the flow, assumed to be linear. As it is planned to measure ammonia concentration at the specific point $x = x_{meas}$, Equation 16 can be integrated starting from the entry

point of the sensor system, x = 0, where the initial ammonia concentration is c^0_g, to the point x = x_{meas}, where the concentration c_{mg} is measured. This integration results in the following expression:

$$\frac{\partial c_g^m(t)}{\partial t} = \frac{\Phi}{V}\left[c_g^0 - c_g^m\right] - \frac{S}{V}\frac{\partial c_w(x,t)}{\partial t} \quad (5.17)$$

The factor Φ/V corresponds to the reciprocal of the characteristic gas-exchange time, denoted as τ_0. The term $\partial c_w / \partial t$ represents the effective rate of adsorption, which essentially encapsulates the disparity between the rate of adsorption and the rate of desorption. To express $\partial c_w / \partial t$, we can delineate it as a dynamic exchange of molecules between the surface and the gas by distinguishing between these two contributing factors. Assuming that the surface wall coverage reaches saturation at c_w0, the quantity of gas molecules lost to the surface per unit time (i.e., adsorption) can be considered directly proportional to the density of unoccupied binding sites on the surface, represented as $c_w0 - c_w$. Conversely, the number of molecules departing from the surface per unit time (i.e., desorption) is proportionate to the density of occupied sites, represented by c_w:

$$\frac{\partial c_w}{\partial t} = k_1(c_{w0} - c_w) - k_2 c_w \quad (5.18)$$

In this formulation, the constants k_1 and k_2 serve as the proportionality factors. By using this mathematical representation, we can effectively separate the processes of adsorption and desorption. This separation allows us to discern between two distinct scenarios. First one is the sensor initially contains no ammonia, and at a specific time, a gas mixture with a constant ammonia concentration c_0 is introduced (referred to as sensor filling). Second one, the sensor contains a mixture with a constant ammonia concentration c_0, and at a certain point, it is purged by passing pure N_2 through it (referred to as sensor cleaning). It is reasonable to assume that during sensor filling, the process of desorption is negligible, while conversely, during the sensor cleaning phase,

the process of adsorption can be disregarded. Consequently, for the case of sensor filling, Equation 5.18 can be expressed as follow.

$$\left(\frac{\partial c_w}{\partial t}\right)_f = k_1(c_{w0} - c_w) \quad (5.19)$$

Which has the solution as

$$c_w(t)|_f = c_{w0}\left(1 - e^{-\frac{t}{\tau_1}}\right) \quad (5.20)$$

where $\tau_1 = 1/k_1$. By combing Eq. 5.17 and 5.20 and imposing the boundary condition $c^m_g(0) = 0$ and $c^0_g = c_0$, $c^m_g(t)|_f$ can be expressed as:

$$c_g^m(t)\big|_f = A_0\left(1 - e^{-\frac{t}{\tau_0}}\right) + A_1\left(1 - e^{-\frac{t}{\tau_1}}\right) \quad (5.21)$$

Where $A_o = c_o - A_1$, and A_1 is:

$$A_1 = \frac{S \cdot c_{w0}}{\Phi(\tau_1 - \tau_0)} \quad (5.22)$$

For sensor cleaning part of the Equation 5.18 can be neglected, hence the solution is:

$$c_w(t)|_c = c_{w0}\, e^{-\frac{t}{\tau_2}} \quad (5.23)$$

where $\tau_2 = 1/k_2$. Again, by combing Eq. 17 and 23 and imposing the boundary condition $c^m_g(0) = c_0$ and $c^0_g = 0$, the $c^m_g(t)|_c$ can be expressed as:

$$c_g^m(t)\big|_c = A_2\left(1 - e^{-\frac{t}{\tau_0}}\right) - A_3\left(1 - e^{-\frac{t}{\tau_2}}\right) \quad (5.24)$$

Where $A_2 = c_0 - A_3$, while A3 is stated in Equation 5.25.

$$A_3 = \frac{S \cdot c_{w0}}{\Phi(\tau_2 - \tau_0)} \quad (5.25)$$

To determine the values of τ_0, τ_1, and τ_2, we utilized two gas cylinders: one containing a certified NH_3 concentration of 14 ppm in N_2, and the other containing pure N_2. These cylinders served as input sources for our gas blending system. The process of sensor filling was initiated with the introduction of pure N_2 into the sensor enclosure. At a specific moment (equivalent to t = 0 in our theoretical model), a rapid switch interrupted the flow of N_2, and the certified NH_3 mixture commenced flowing through the system. Conversely, the sensor cleaning process began with the certified NH_3 mixture and transitioned to pure N_2 at t = 0 using a rapid switch mechanism. In both scenarios, the laser current remained fixed to the NH_3 absorption peak, while sinusoidal modulation was applied with a peak-to-peak current of 15 mA, employing WM-2f detection. The NH_3 QEPAS signal, normalized to the unit, as a function of time during both the filling and cleaning procedures, is presented in Figures 5.18 (a) and 5.18 (b), respectively.

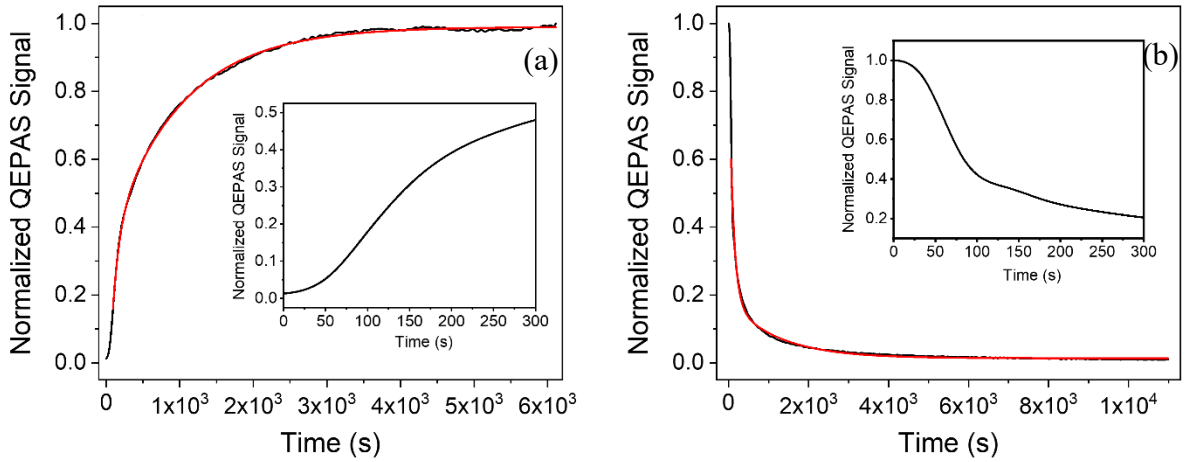


Figure 5.18. (a) - The graph illustrates the QEPAS signal, which has been normalized, plotted against time, and synchronized with the NH_3 absorption peak during the filling process. The actual signal is represented by the black curve, and it has been fitted using an exponential function based on Eq.21, depicted by the red curve. Inset: A closer examination of the signal's initial rise reveals an inflection point; (b) - The graph displays the normalized QEPAS signal over time, synchronized with the NH_3 absorption peak during the cleaning process. The black curve represents the observed signal, while the red curve represents the exponential fit based on Eq. 24. Inset: A closer look at the initial decline in the signal reveals an inflection point.

The initial signal rise shows a positive concavity up to t = 92 s, when there occurs an inflection point, as seen in the inset of Fig. 5.18 (a). As a result, the QEPAS signal rises more slowly for t of 92 s than it was predicted by theoretical analyses, indicating the presence of nonlinear effects that are not taken into account by the simple theoretical model [18]. Due to the high initial density of free binding sites on the inner surfaces of the sensor, it is possible to explain the early QEPAS signal behaviour by the fact that few molecules reach the measurement point, or spectrophone, and the chance of NH_3 molecules being captured is quite high. The NH_3 molecules can more easily reach the spectrophone as these sites begin to fill, and a dynamic equilibrium between the gas flux and the adsorption processes can be established, which is the condition imposed by the theoretical model during the transient. The QEPAS signal decrease appears to be delayed until t = 60 s, at which point it drops down with a positivity concavity, as predicted before. A similar situation is also seen during the sensor cleaning process. These factors led to the fitting of only experimental data above and below the inflection points using equations 21 and 24, respectively, and their reporting as solid red lines in figures 5.18 (a) and 5.18 (b) for the filling and cleaning processes. The filling procedure takes τ_0 = 93 and τ_1 = 966 seconds, and the cleaning procedure takes τ_0 = 107 and τ_2 = 1212 seconds, according to the fitting procedure. In both situations, the time constant associated with adsorption/desorption processes is significantly larger than the typical gas-exchange time constant, which is mostly only because of the dimensions and the flow of gas. All mentioned above results were carefully implemented for a better calibration of ammonia sensor.

Starting with the certified concentration of 14 ppm of NH_3 in N_2, the calibration of Sensor Head for NH_3 was carried out similarly to calibration which were done for previous sensors (section

5.3). A 60-minute waiting period was taken into account for each dilution in order to reach a steady-state signal. The sensor was cleaned following that before going on to the next dilution. Fig. 5.19 reports the QEPAS signal for various NH_3 concentrations in N_2 (from 1.4 ppm to 14 ppm).

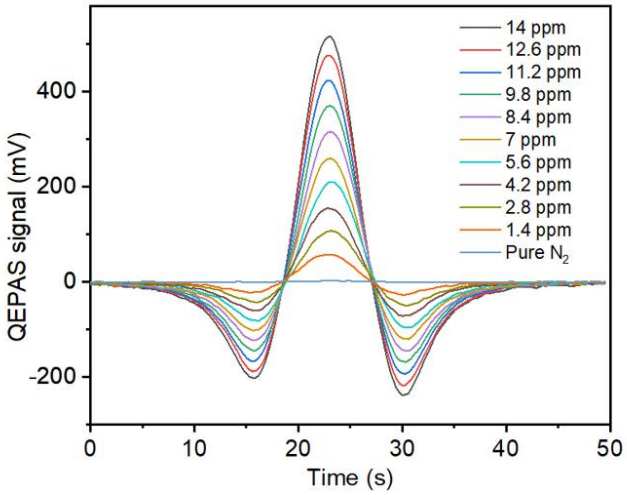


Figure 5.19. QEPAS signal for different concentrations of NH_3

In Fig. 5.20, the peak values are plotted as a function of the NH_3 concentration along with the linear fit, which yields sensitivity of 37.22 mV/ppm (slope of the linear fit).

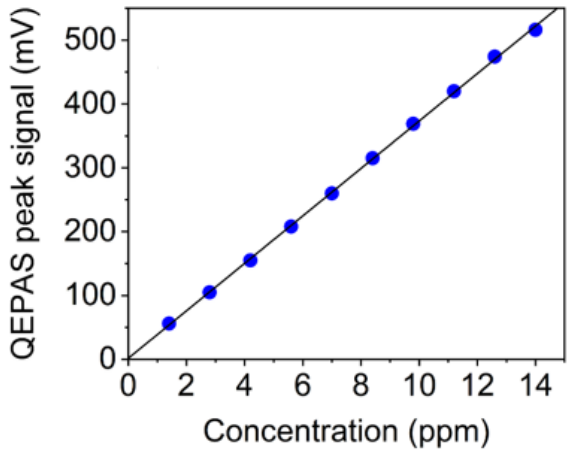


Figure. 5.20. Calibration curve for NH_3 detection

Fig. 8 reports the results of the Allan-Werle analysis, which were made to determine the minimum detection limit (MDL) as a function of the integration time. From such analyses a MDL of 5.8 ppb for 0.1 s integration time was deducted.

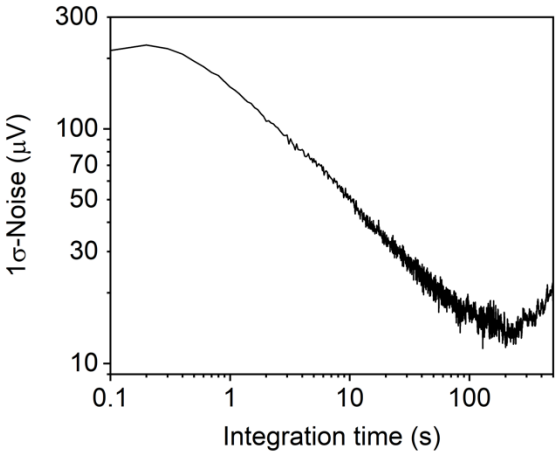


Figure 5.21. Allan-Werle deviation analysis for the NH_3 sensor.

To sum up, should be said that a highly sensitive and selective sensor for ammonia detection was developed and tested. Adsorption and desorption processes were modelled and taken into consideration for an accurate calibration of the sensor because ammonia is a polar molecule with a large and permanent dipole moment. When taking into account a 60-minute waiting period between each concentration in the calibration phase, an NH_3 minimum detection limit of 5.8 ppb at an integration time of 0.1 s was estimated. At an integration time of 10 sec, the MDL results 1.4 ppb, a record value for QEPAS.

The MDLs reached for the three gas species at an integration time of 0.1 s are below the natural abundance of the three analytes, thus making the two sensor heads suitable for the monitoring of their levels in environmental air. Thereby a portable QEPAS 19-inches 6U-rack sensor system capable to detect methane, nitrous oxide, and ammonia, implementing two sensor heads have been realised. The architecture and a picture of the realised system is shown in Figure 5.22.

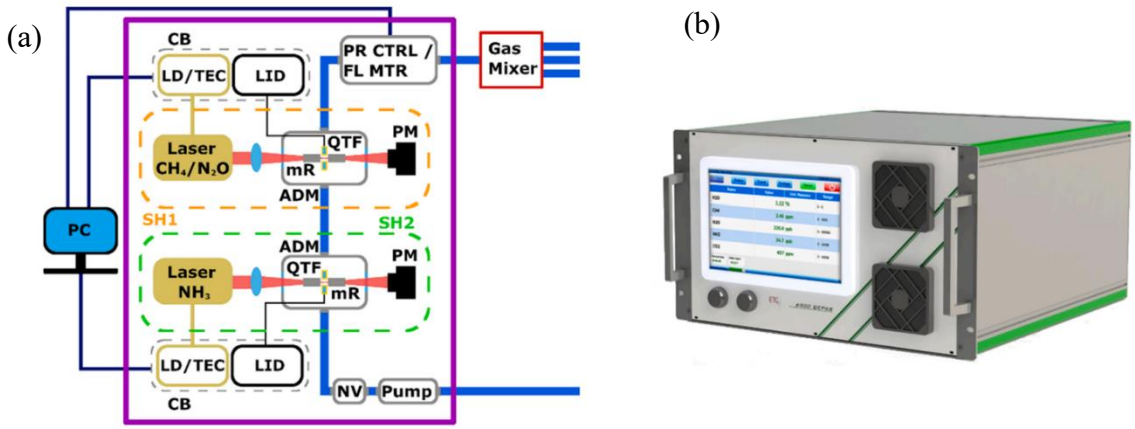


Figure. 5.22. (a)- Schematic of the sensor box composed of two QEPAS sensor heads, one for detection of CH_4 and N_2O, the other for NH_3 detection, connected in series in the same gas line; (b) - Picture of the realized 19-inches 6U-rack sensor. Size: 35cmx55cmx44cm, weight 14 kg. PC – Personal Computer; QTF – Quartz Tuning Fork; mR – Resonator tubes; ADM – Acoustic Detection Module; PM – Power Meter; SH1 – Sensor Head 1; SH2 – Sensor Head 2; CB – Control Board; LD – Laser Driver; TEC – Thermoelectric Cooler; LID – Lock-In Detection; PR CTRL/FL MTR – Pressure controller/ Flow Meter; NV – Needle Valve.

The sensor was employed to measure the concentrations of methane, nitrous oxide, and ammonia in laboratory air for more than 4 h. The use of the Nafion humidifier allowed keeping stable the water concentration to 1.2 %. This approximately corresponds to 50 % relative humidity at 20 ◦C. This setting is reasonable because the relative humidity of the laboratory air is significantly lower than 50 %. For the cases in which the relative humidity is higher than 50 %, one possibility is to insert a membrane gas dryer before the tube humidifier for an upstream reduction of the relative humidity below 50 %. A software was developed to drive both sensor heads and acquire and process the QEPAS signals. The measurements were performed at 500 Torr by acquiring QEPAS spectral scans of the CH_4 and N_2O absorption lines with Sensor Head 1 and the QEPAS spectral of the NH_3 absorption line with the related sensor head, both operating at 0.1 s integration time. For each spectral scan, the QEPAS peak signals of CH_4, N_2O, and NH_3 absorption features were extracted and are plotted as a function of time in Fig. 5.23.

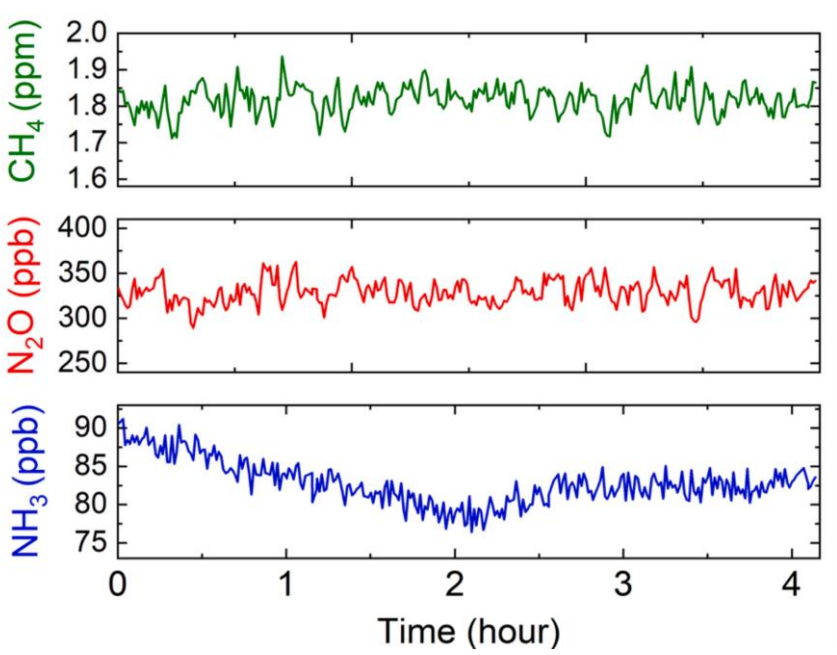


Figure. 5.23. QEPAS peak signals extracted by consecutive QEPAS spectra acquired by sampling the air inside the laboratory at fixed H2O concentration of 1.2 %.

The time interval between two consecutive peaks of the same analyte was 50 s. The reported concentrations were calculated using the calibration curve of each analyte. The extracted peaks returned stable concentrations of methane and nitrous oxide, with an average CH_4 concentration of 1.81 ppm, with a standard deviation of 0.04 ppm, and an average N_2O concentration of 330 ppb, with a standard deviation of 13 ppb. These measured values are consistent with the expected CH_4 and N_2O levels in atmosphere [19]. The ammonia concentration slightly varied during the measurement period, with an average level of 83 ppb and a standard deviation of 3 ppb. This NH_3 level is coherent with the typical levels of ammonia in indoor air [20].

The realised sensing device is very compact and has following dimensions: 35cmx55cmx44cm. The weight of final packaging is equal to 14kg in total. Such numbers would allow to use mentioned sensors for environmental detection on unarmed air vehicles (UAVs),precisely th

sensing module can be lifted by such models as Freefly Alta X (max lifting weight 15 kg, flight time 20 min and range 5 km), JOUAV CW-80E (max lifting weight 25 kg, flight time 840 minutes and range up to 200 km), Draganfly Heavy Lift Drone (max lifting weight 30 kg, flight time 55 min, range 20 km) and finally Ehang 184 (max lifting weight 100 kg, flight time 23 minutes and range 30 km).

Conclusion

During this PhD research, the primary focus was directed towards the exploration of compact and highly sensitive solutions for the detection and analysis of toxic gases, particularly within the realm of optical absorption spectroscopy. The Quartz-Enhanced Photoacoustic Spectroscopy (QEPAS) technique served as a detection platform, with a customized T-shaped Quartz Tuning Fork (QTF) employed as the core sensing element.

The initial objective of the research was the development of dual-sensor systems capable of detecting both CH_4 and N_2O at environmental level. The main goal was to harness the same laser source operating at a wavelength of 7.8 micron and the same sensor head for each gas individually, with the subsequent exploration of the possibility of simultaneous detection. Remarkably, the sensors achieved a Minimum Detectable Limit (MDL) of 28 ppb for CH_4 and 8.6 ppb for N_2O for 0.1 s integration time for both gases, showcasing optimal sensitivity for environmental monitoring. Furthermore, the stability of the sensor was validated under laboratory conditions, with continuous operation over a 24-hour period. To ensure the reproducibility of these sensors for potential commercialization, two sensor heads were developed, each featuring slight variations in laser and QTF characteristics, yet both yielded consistent and reliable performance results.

Another significant contribution of this research involved the creation of a compact sensor designed specifically for NH_3 detection. The calibration of this sensor was meticulously conducted, taking into account the adsorption and desorption processes crucial for accurate measurements. Ammonia's distinct characteristics as a polar molecule with a substantial permanent dipole moment were factored into the sensor's operation. When considering a 60-minute waiting period between each concentration level during the calibration phase, the sensor achieved an record Minimum Detection Limit of 1.4 ppb for NH_3, with an integration time of 10 seconds.

A portable QEPAS 19-inches 6U-rack sensor system capable to detect methane, nitrous oxide, and ammonia, three important analytes for the study of the environmental footprint of agriculture and food production industry, was realised. The sensor was employed to monitor the concentration of methane, nitrous oxide and ammonia in laboratory air, since the achieved detection limits were all below the natural abundance of the three gas species in atmosphere. This measurement returned an average CH_4 concentration of 1.81 ppm, an average N_2O concentration of 330 ppb and an average NH_3 concentration of 83 ppb. These results are compatible with the expected levels of these analytes in indoor air. Considering the obtained performances and the lab test, the realized sensor results suitable for the on-field monitoring of gas traces of methane, nitrous oxide and ammonia for agriculture and food production industry applications.

In the sensors mentioned earlier, industrial laser sources from Thorlabs were employed. The subsequent phase of the research involved the development of a custom and efficient laser source specifically tailored for integration into these sensor heads. This laser source needed to fulfil stringent criteria, including single-mode operation, adequate output power, low power consumption, a narrow laser linewidth, and excellent tunability. Consequently, the research embarked on the creation of novel Distributed Feedback (DFB) laser diodes featuring gratings

positioned atop the laser ridge. We decided to work on InGaAsSb/GaSb quantum wells laser diodes. Comprehensive simulations were conducted to optimize various parameters, exploring how variations in upper cladding thickness and grating etching depth affected coupling, losses, and confinement factor.

Once the design parameters were established, additional experiments were conducted with Fabry-Perot laser diodes featuring different layers configurations to validate the trends observed in simulations. Subsequently, we have fabricated DFB laser diodes with gratings positioned on the top of the ridge, achieving low threshold current (I_{th}) of 25 mA, output powers reaching up to 9 mW, a Side-Mode Suppression Ratio (SMSR) of 25 dB, and stable continuous tuning capabilities. This innovative design was also replicated in an industrial setting and compared with more mature processes of devices with grating along the laser ridge. The outcome yielded a collection of single-mode devices characterized by sufficient power output, low I_{th}, excellent tuning capability, and the capacity to target gases such as HF, NH_3, and CH_4.

Looking ahead, it is of the high interest to use fabricated and packed GaSb-based DFB laser diodes emitting at 2.4 microns for the detection of NH_3, CH_4 and HF and to integrate them in the developed compact QEPAS module. Developed QEPAS module can be also implemented on the existed on market UAVs for environmental detection of toxic gases,

Reference

[1] Viegerov, M.L. Eine methode der gasanalyse, beruhend auf der optisch-akustischen tyndallrontgenerscheinung. ¨. Dokl. Akad. Nauk SSSR 1938, 19, 687–688.

[2] Kreuzer, L.B. Ultralow gas concentration infrared absorption spectroscopy. J. Appl. Phys. 1971, 42, 2934–2943.

[3] Allan Rosencwaig, Allen Gersho; Theory of the photoacoustic effect with solids. *Journal of Applied Physics* 1 January 1976; 47 (1): 64–69. https://doi.org/10.1063/1.322296

[4] Kerr, E.L.; Atwood, J.G. The Laser Illuminated Absorptivity Spectrophone: A Method for Measurement of Weak Absorptivity in Gases at Laser Wavelengths. Appl. Opt. 1968, 7, 915.

[5] Zeninari, V.; Kapitanov, V.A.; Courtois, D.; Ponomarev, Y.N. Design and characteristics of a differential Helmholtz resonant photoacoustic cell for infrared gas detection. Infrared Phys. Technol. 1999, 40, 1–23.

[6] Rouxel, J.; Coutard, J.G.; Gidon, S.; Lartigue, O.; Nicoletti, S.; Parvitte, B.; Vallon, R.; Zéninari, V.; Glière, A. Miniaturized differential Helmholtz resonators for photoacoustic trace gas detection. Sensors Actuators, B Chem. 2016, 236, 1104–1110.

[7] Bauer, R.; Stewart, G.; Johnstone, W.; Boyd, E.; Lengden, M. 3D-printed miniature gas cell for photoacoustic spectroscopy of trace gases. Opt. Lett. 2014, 39, 4796–4799.

[8] B. Berne, R. Pecora, Dynamic Light Scattering: With Applications to Chemistry, Biology, and Physics, Springer, Boston, MA, 2000.

[9] A. Sampaolo, P. Patimisco, M. Giglio, A. Zifarelli, H. Wu, L. Dong, V. Spagnolo, "Quartz-enhanced photoacoustic spectroscopy for multi-gas detection: A review", Anal. Chim. Acta 1202, 338894 (2021).

[10] W.H. Flygare, Molecular relaxation, Acc. Chem. Res. 1 (1968) 121–127. [109]

[11] G. Wysocki, A.A. Kosterev, F.K. Tittel, Influence of molecular relaxation dynamics on quartz-enhanced photoacoustic detection of CO2 at λ =2 μm, Appl. Phys. B Lasers Opt. 85 (2006) 301–306.

[12] A.A. Kosterev, Y.A. Bakhirkin, F.K. Tittel, S. McWhorter, B. Ashcraft, QEPAS methane sensor performance for humidified gases, Appl. Phys. B Lasers Opt. 92 (2008) 103–109.

[13] S. Dello Russo, A. Sampaolo, P. Patimisco, G. Menduni, M. Giglio, C. Hoelzl, V.M.N. Passaro, H. Wu, L. Dong, V. Spagnolo, Quartz-enhanced photoacoustic spectroscopy exploiting low-frequency tuning forks as a tool to measure the vibrational relaxation rate in gas species, Photoacoustics 21 (2021) 100227. https://doi.org/10.1016/j.pacs.2020.100227.

[14] J. Manne, O. Sukhorukov, W. J¨ ager, J. Tulip, Pulsed quantum cascade laser-based cavity ring-down spectroscopy for ammonia detection in breath, Appl. Opt. 45 (36) (2006) 9230–9237.

[15] C. Wang, P. Sahay, Breath analysis using laser spectroscopic techniques: breath biomarkers, spectral fingerprints, and detection limits, Sensors 9 (10) (2009) 8230–8262.

[16] I. E. Gordon, L. S. Rothman, R. J. Hargreaves, R. Hashemi, E. V. Karlovets, F. M. Skinner, E. K. Conway, C. Hill, R. V. Kochanov, Y. Tan, P. Wcisło, A. A. Finenko, K. Nelson, P. F. Bernath, M. Birk, V. Boudon, A. Campargue, K. V. Chance, A. Coustenis, B. J. Drouin, J. M. Flaud, R. R. Gamache, J. T. Hodges, D. Jacquemart, E. J. Mlawer, A. V. Nikitin, V. I. Perevalov, M. Rotger, J. Tennyson, G. C. Toon, H. Tran, V. G. Tyuterev, E. M. Adkins, A. Baker, A. Barbe, E. Canè, A. G.

Császár, A. Dudaryonok, O. Egorov, A. J. Fleisher, H. Fleurbaey, A. Foltynowicz, T. Furtenbacher, J. J. Harrison, J. M. Hartmann, V. M. Horneman, X. Huang, T. Karman, J. Karns, S. Kassi, I. Kleiner, V. Kofman, F. Kwabia-Tchana, N. N. Lavrentieva, T. J. Lee, D. A. Long, A. A. Lukashevskaya, O. M. Lyulin, V. Y. Makhnev, W. Matt, S. T. Massie, M. Melosso, S. N. Mikhailenko, D. Mondelain, H. S. P. Müller, O. V. Naumenko, A. Perrin, O. L. Polyansky, E. Raddaoui, P. L. Raston, Z. D. Reed, M. Rey, C. Richard, R. Tóbiás, I. Sadiek, D. W. Schwenke, E. Starikova, K. Sung, F. Tamassia, S. A. Tashkun, J. Vander Auwera, I. A. Vasilenko, A. A. Vigasin, G. L. Villanueva, B. Vispoel, G. Wagner, A. Yachmenev, S. N. Yurchenko, The HITRAN2020 molecular spectroscopic database, J. Quant. Spectrosc. Radiat. Transf. 277 (2022) 107949. https://doi.org/10.1016/j.jqsrt.2021.107949.

[17] O. Vaittinen, M. Metsälä, S. Persijn, M. Vainio, L. Halonen, Adsorption of ammonia on treated stainless steel and polymer surfaces, Appl. Phys. B. 115 (2014) 185-196. https://doi.org/10.1007/s00340-013-5590-3.

[18] J. Henningsen, N. Melander, Sensitive measurement of adsorption dynamics with nonresonant gas phase photoacoustics, Appl. Opt. 36 (1997) 7037-7045. https://doi.org/10.1364/AO.36.007037.

[19] A. Schmohl, A. Miklos, P. Hess, Effects of adsorption–desorption processes on the response time and accuracy of photoacoustic detection of ammonia, Appl. Opt. 40 (2001) 2571-2578. https://doi.org/10.1364/ao.40.002571.

[20] M. Li, C.J. Weschler, G. Beko¨, P. Wargocki, G. Lucic, J. Williams, Human ammonia emission rates under various indoor environmental conditions, Environ. Sci. Technol 54 (2020) 5419–5428